THE UNIVERSITY OF CHICAGO

DRIVING PROCESSES BEHIND THE GLOBAL OCEAN CIRCULATION: WATER MASS TRANSFORMATIONS AND THE EFFECT OF SOUTHERN OCEAN TOPOGRAPHY

A DISSERTATION SUBMITTED TO
THE FACULTY OF THE DIVISION OF THE PHYSICAL SCIENCES
IN CANDIDACY FOR THE DEGREE OF
DOCTOR OF PHILOSOPHY

DEPARTMENT OF GEOPHYSICAL SCIENCES

BY
TATSU MONKMAN

CHICAGO, ILLINOIS
JUNE 2024

To my parents

The sea, thundering on all the shores of the world, and the universal ocean of air, though invisible, speaks aloud in a thousand voices

TABLE OF CONTENTS

LIST OF FIGURES

ACKNOWLEDGMENTS

First of all I would like to thank my brilliant advisor Malte Jansen, for all of your tireless help, guidance, and mentoring during these past years. I have gained so much as your student and it was an incredible privilege to learn from your creative and detailed approach to problem solving. I am truly humbled to have been given the opportunity to work with you over these past years, and I cannot thank you enough for all you have taught me.

I would like to thank my committee members Douglas MacAyeal, Noboru Nakamura, and Tiffany Shaw for all of their constructive feedback, interesting perspectives, and encouragement during my time in Chicago. I would like to thank you in particular for the invaluable foundation in Geophysical Fluid Dynamics each of you contributed to during my first year, and for the thought-provoking discussions about my work from the perspectives of those in the atmospheric and glaciological fields.

I would also like to thank the rest of the University of Chicago faculty for the learning opportunities and community they provided during my time in the Geophysical Sciences Department. In particular I would like to thank Liz Moyer for an invaluable introduction to climate science and for her mentorship during Rossbypalooza, as well as Fred Ciesla and Dorian Abbot for their guidance during my time as a Teaching Assistant.

I would like to thank the administrative staff in the Geophysical Sciences Department, in particular Jolene Hanchar, Adelaide Grosse, and Victor Gavin, for all of the logistical support over the years. Your kind help has been invaluable to the smooth continuation of my graduate studies and I can't imagine how I would have navigated the complexity of the academic bureaucracy without you.

I would like to thank my many good friends in the Department of Geophysical Sciences graduate student and postdoc body for making my time here so enjoyable: Ziwei Wang, for your camaraderie, fun conversation, and sensible advice for navigating graduate school and beyond; Haynes Stephens, for our periodic check-ins and for keeping each other sane during challenging times; Maria Hernandez Limon, for you tireless efforts to organize outreach events

and communicate our work to the next the next generation of scientists; David Cerny, Anna Wisniewski, Zhe Zhang, and the other members of my cohort for our shared experience early on in graduate school and in grappling with the challenges posed by COVID-19. I would like to thank the past students and postdocs who welcomed me into the department when I first arrived: Hailu Kong for your reassuring advice, encouragement, and example as one of the few other physical oceanography students in our department; previous graduate students Pragallva, Osamu, and Jim, and postdocs Todd, Zhihong, Jenny, and Hung-I for your inspiring work and thoughtful discussions in climate journal club. I would also like to thank the climate students and postdocs who entered the department after me: Bowen, Xuan, Carly, Joonsuk, Siming, Camilla, Giorgo, Huanzhou, Lin, Freya, Hsing-Hung, Jiacheng, Nuanling, Allison, Sam, Branson and Yaoxuan, for making the climate group a vibrant, friendly, and stimulating experience. I learned so much from you and discussing new and interesting literature with you during journal club was the highlight of my graduate school experience. I am going to miss you all.

I would like to thank my friend and fellow graduate student, Jordan Todes, for letting me tag along during a short fieldwork excursion to Owens Valley, California, in what unexpectedly became the adventure of a lifetime. I would also like to thank the chief scientists on the GO-SHIP I08S cruise, Sebastien Bigorre and Katelyn Schockman, for allowing me, a clumsy ocean modeler, the immense privilege of performing fieldwork on the Southern Ocean.

I would like to thank my two longterm roommates and lifelong friends, Andrea and Brenda Benitez, as well as the rest of the Benitez family for their friendship and support during my time in Chicago. I am forever indebted to the generosity you showed me when I first arrived alone in Chicago so many years ago. I will miss you dearly.

I would like to thank my undergraduate thesis advisor, Philip Choi, who instilled a love of science and discovery in me, gave me endless encouragement and support during my time at Pomona, and wrote a letter of recommendation for me when I applied to graduate school. Although I have strayed a bit from pure physics and astronomy, the solid foundation you

gave me in technical skills and the joy of studying the natural world you instilled in me is something I cherish everyday.

I would like to thank my partner for almost the entirety of graduate school, Lois, for your humor, love, and for always believing in me even when it felt like everything was lost. I am so grateful for you and am so proud of how far you have come in your own research. I hope someday soon we will both stand on top of a glacier together again.

I would like to thank my brother Forest, for your wit, friendship, and for remaining close even as academics and life has pulled us to different ends of the country. I am so impressed and proud of how far you have come, and I can't wait to see all of the great things you accomplish as a fellow PhD and mathematician.

I would like to thank my grandparents for everything you have done for me, especially during my post-college years crisscrossing the country (sometimes aimlessly) when I always seemed to land back in your driveway in Kenmore. Thank you grandma for your quiet encouragement and numerous life lessons, and thank you grandpa for the hours of interesting conversations concerning research and academia and for being an example of what it means to be a truly great scientist. I can never begin to repay you for everything.

Finally I would like to thank my mom and dad for being my parents, for a childhood immersed in the natural world, and for showing me that with hard work and determination I was capable of so much more than I believed. It is thanks to you that I have come this far. I love you.

ABSTRACT

The ocean's Meridional Overturning Circulation (MOC) plays a central role Earth's climate, setting the stratification and large scale dynamics of the global ocean and controlling the abyssal storage of carbon and heat. However, fundamental questions remain regarding the overall structure and driving processes of the MOC. In this dissertation we take a step towards establishing a more comprehensive view of the global MOC that takes into account modern observation-based predictions of its driving processes and the role of complex topography in the Southern Ocean in influencing its structure. We begin by characterizing the volume transport and water mass transformation rates of the global overturning circulation using the Estimating the Circulation and Climate of the Ocean (ECCO) reanalysis product. The ECCO solution supports a large rate of exchange between the mid-depth and abyssal overturning cells, consistent with recent estimates. However, much of the upwelling in ECCO's deep ocean is not associated with irreversible water mass transformations as is typically assumed in theoretical models. Instead, a dominant portion of the abyssal circulation in ECCO is associated with isopycnal volume tendencies, reflecting a deep ocean in a state of change and a circulation in which transient tendencies play a leading role in the water mass budget. Although observational constraints are insufficient to unambiguously determine whether the simulated tendencies are real, there are indications that much of the trends in ECCO are spurious. Whether or not ECCO's tendencies are realistic, they are a key part of its abyssal circulation and hence need to be taken into consideration when interpreting the ECCO solution.

We next address the role of Southern Ocean topography and wind stress in the deep ocean overturning and water mass composition using a suite of idealized global ocean circulation models. Specifically, we investigate how the presence of a meridional ridge in the vicinity of Drake Passage and the formation of an associated Southern Ocean gyre influences the water mass composition of the MOC's abyssal limb. Our results show that a Drake Passage ridge can significantly decrease the strength of the mid depth cell, provided the ridge is

high enough to intersect the isopycnals along which NADW flows southward. Passive tracer experiments meanwhile show that a weakening mid-depth cell is linked to decreasing abyssal ventilation by North Atlantic water masses, and further that an increasing ridge height in Drake Passage and a concurrent gyre spin-up leads to a substantial decrease in NADW-sourced AABW (AABW forms from former NADW that surfaces in the Southern Ocean) in the abyssal ocean. We explain this behavior using a simple scaling relationship between the gyre and a mixing-driven exchange of NADW-origin waters with the surface layer north of the ACC, and in the final study of this dissertation we test this mixing pathway against more complex idealized setups. Our results show that the gyre-driven mixing pathway is robust in the presence of zonal extensions to the Drake Passage ridge and in the presence of additional submarine topographic barriers placed throughout the Southern Ocean domain.

CHAPTER 1

INTRODUCTION

The meridional overturning circulation (MOC) is a major part of the planetary-scale circulation of Earth's oceans and is the primary process by which the ocean equilibrates its internal heat and tracer composition with the broader climate (Talley et al., 2003; Sigman et al., 2010). The MOC is driven by air-sea forcing at the ocean surface, where wind stress, heat, and freshwater fluxes drive the large-scale horizontal and vertical advection of seawater, giving rise to a global circulation that is tied to atmospheric forcing and variability (Lumpkin and Speer, 2007). The MOC connects the major ocean basins and drives exchange between the different vertical ocean levels, and plays a critical role in redistributing heat and tracers between ocean basins and between the surface and the ocean interior. The response of the MOC and the ocean to changing climatic conditions further results in feedbacks between the ocean and the climate on a variety of spatial and temporal scales (Marshall et al., 2015), making accurate characterizations of its structure and driving processes a central goal of modern climate science.

Our understanding of the MOC's structure has historically lagged behind that of the atmosphere due to the difficulty of observing the deep ocean (Talley, 2013). The earliest modern observations of large scale vertical oceanic circulation date back to the early-mid 19th century, when measurements taken during Wust and Defant's polar expeditions indicated the creation of North Atlantic Deep Water (NADW) and Antarctic Bottom Water (AABW) in the high latitudes (Wust and Defant, 1936). In response, Stommel and Arons (1959) developed some of the earliest models for the large scale circulation of NADW and AABW (and by extension the MOC), in which diffusive upwelling in the interiors of the ocean basins was hypothesized to balance sinking deep water at the high latitudes and form closed meridional circulation cells. To account for the different water mass properties of NADW and AABW, lighter and denser water masses respectively, Stommel and Arons (1959) proposed the classic "two-cell" schematic of the deep ocean circulation in which AABW and

NADW circulate vertically and meridionally via two distinct lower and upper cells. In this picture, NADW forms in the North Atlantic, circulates through the mid-ocean at depth, and surfaces in the Indo-Pacific via diffusive upwelling forming the "mid depth" cell (Note that the mid depth cell is often referred to as the "Atlantic Meridional Overturning Circulation" or "AMOC" due to its primary localization to the Atlantic basin). Concurrently, AABW sinks off the coast of Antarctica and spreads across the ocean bottom below NADW and upwells diffusively in the abyssal Indo-Pacific and Atlantic basins forming the "abyssal" cell (Broecker, 1987). The different surface forcings that set the composition of each deep water mass (Figure 1.1) was (and remains) a key difference between the mid depth and abyssal cells (Gordon, 1986). Variations of this general, two-cell picture have persisted to the present day and can be seen in most global observational datasets (Figure 1.1).

The historic picture of mixing-driven abyssal upwelling presented a problem for mid-century oceanographers, however: in order to balance the rate of dense water formation in the high latitudes and maintain the observed abyssal stratification, much stronger vertical mixing in the interior ocean was required than was actually observed (Munk, 1966; Kunze et al., 2006; Ledwell et al., 1998). This problem, dubbed the "missing-mixing paradox," persisted through the 20th century and was only solved very recently with the recognition of the central role of wind-driven upwelling in the Southern Ocean (Toggweiler and Samuels, 1998; Nikurashin and Vallis, 2012), a region whose characterization has historically lagged that of the northern basins due to its extreme observation conditions and remote location. The circulation of the Southern Ocean is unique due to its topography - the lack of a meridional continental barrier in the latitudes of Drake Passage and intense westerly winds over the Southern Ocean allow the formation of a clockwise circumpolar circulation around Antarctica known as the Antarctic Circumpolar Current (ACC). The ACC is accompanied by a net northward Ekman transport of surface waters, which is balanced by upwards flow along upward tilting isopycnals that outcrop at the Southern Ocean surface. Crucially, these tilted isopycnals allow a large portion of the dense water in the ocean interior to

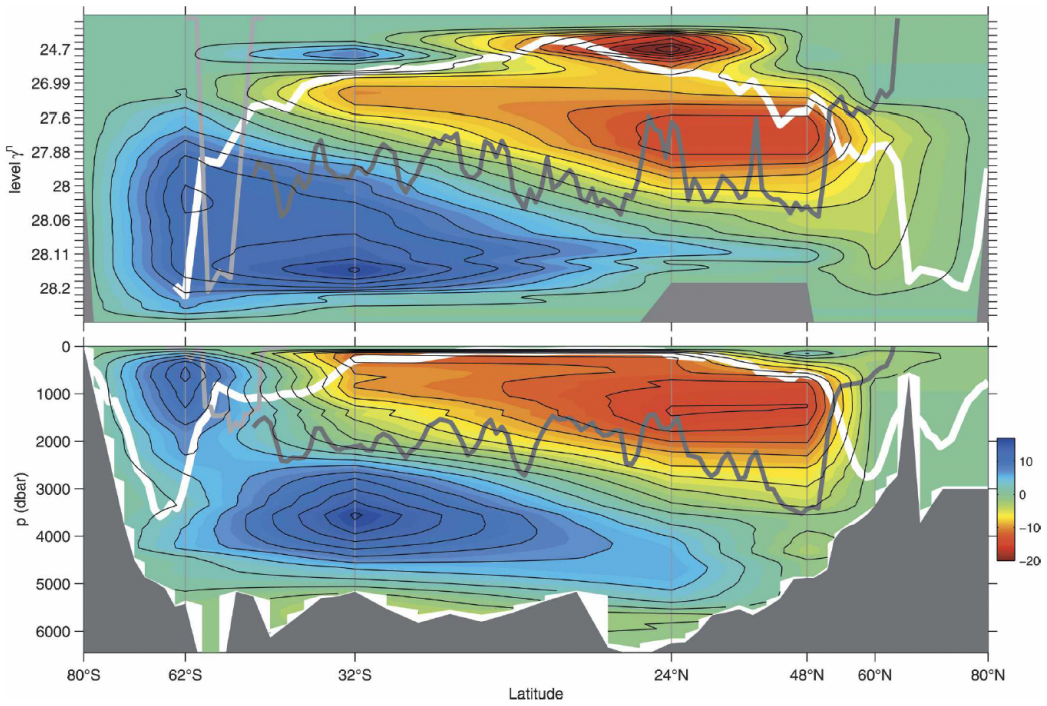

Figure 1.1: Taken from Lumpkin and Speer (2007): The Global MOC, zonally integrated to show the meridional stream function, Ψ, in neutral density (top) and pressure levels (bottom), at 2 Sv contour levels. This picture of the MOC was produced using inverse methods based off of hydrographic sections, the approximate latitudes of which are shown by the vertical gray lines. Solid contour lines give the average winter mixed layer level at each latitude (white), the mean depth of ocean ridge crests (dark grey), and depth of the Scotia Arc east of Drake Passage (light).

return adiabatically to the ocean surface and therefore connect the ocean interior to the surface without the need for large interior diffusivities. While the potential importance of the Southern Ocean circulation was hypothesized early by Eady (1957), it was not until Toggweiler and Samuels (1998) and Webb and Suginohara (2001) that the implications of this phenomenon for the MOC were recognized. Thus, the "missing-mixing paradox" is largely accounted for in the modern view of the MOC where the return limbs of the mid depth and abyssal cells are closely tied to the circulation of the Southern Ocean (Marshall and Speer, 2012).

1.1 The MOC: a modern view

Here we summarize our contemporary view of the MOC's large scale structure using the zonally-integrated, two-dimensional view of the global MOC given by the overturning stream function, Ψ (see Chapter 1, 2.2), which gives a good approximation of the large scale transport of water in the global ocean (Nikurashin and Vallis, 2012). Ψ is illustrated in both neutral density and pressure levels in Figure 1.1, where we can immediately see the two major circulation cells emerge: the clockwise mid depth cell extends from the surface to approximately 2 km depth (approximately 2000dbar pressure) and occupies the middle density levels in the deep ocean, and the counterclockwise abyssal cell cell extends from the surface in the Southern Ocean to the ocean bottom and occupies the ocean's highest density levels. Both cells cross the equator and together span the full latitudinal extent of the global ocean, transporting heat and tracers across the solar insolation maximum (Donohoe et al., 2020).

By separating the global transport by ocean basin as in Figure 1.2 we can see that much of the mid depth and abyssal cells are localized to the Atlantic and Indo-Pacific basins, respectively. Deep water formation driving the downward limb of the mid depth cell occurs in the North Atlantic, where dense water produced by deep convection in the Nordic Seas and off the coast of Greenland combine with Arctic Ocean inflow to produce NADW. NADW flows southwards at depth following formation, crosses the equator, and enters the Southern

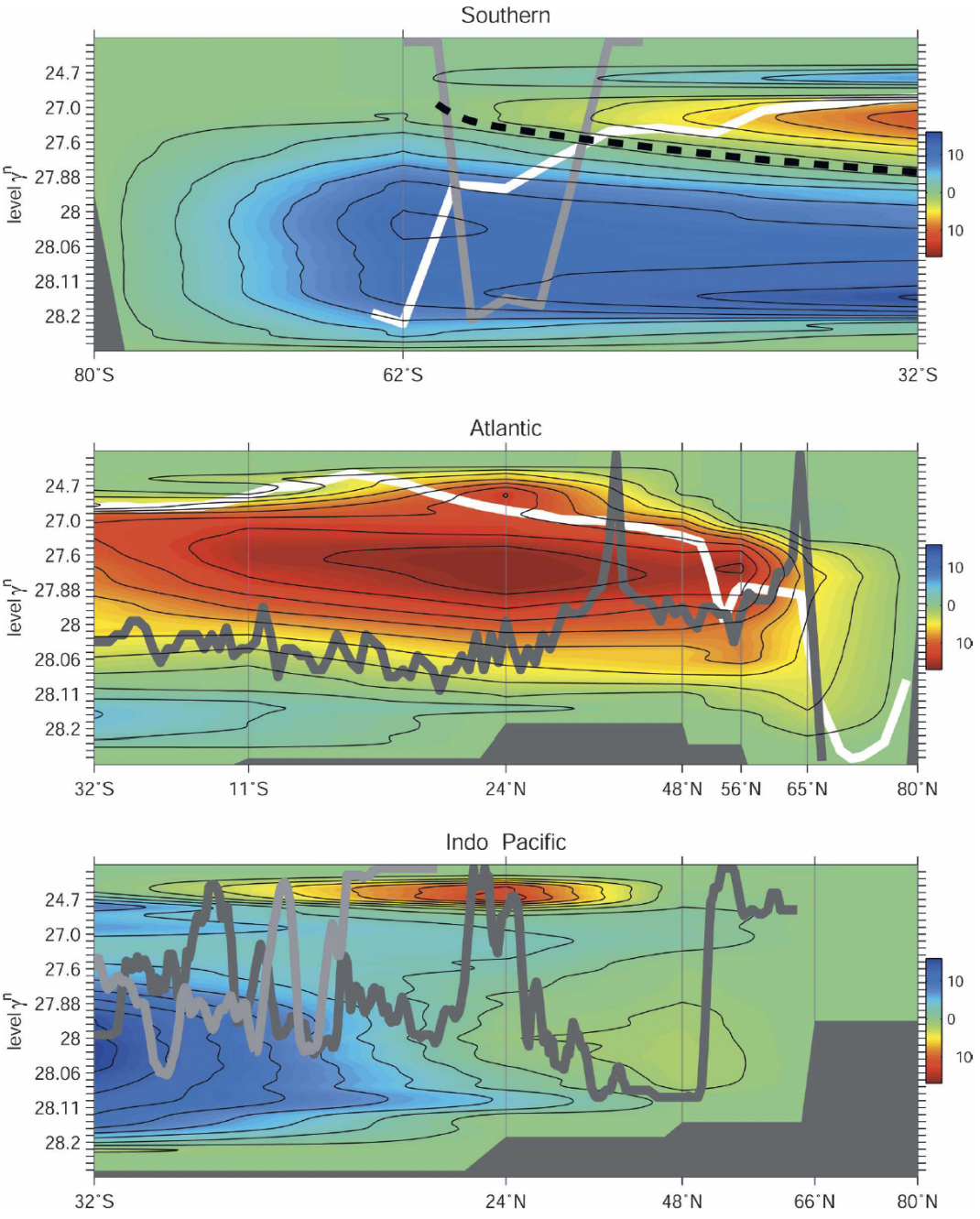

Figure 1.2: Taken from Lumpkin and Speer (2007): Overturning stream functions for different basin-wide subsections of MOC at 2 Sv contour intervals. Subplots give the MOC in neutral density coordinates in the Southern Ocean (top), Atlantic (middle), and Indo-Pacific (bottom) given in neutral density coordinates. The dashed line in the Southern Ocean plot divides the mid depth and abyssal overturning cells, both of which extend into the northern ocean basins. The winter mixed layer level and bathymetric features are represented in the same way as 1.1

Ocean, comprising the lower limb of the mid depth cell. This southward flow of NADW is thought to remain mostly adiabatic, although it also subsumes a small amount of southern ocean-sourced bottom water that mixes upwards diabatically from below (Talley et al., 2011). Once NADW enters the Southern Ocean it upwells along sloped isopycnals to the ocean surface and either moves northward to join intermediate and surface waters north of the ACC, or southward towards AABW formation regions off of the coast of Antarctica.

Deep water in the Indo-Pacific consists mainly of AABW, which forms off of the coast of Antarctica due to high rates of surface buoyancy loss. Following formation, AABW spreads across the bottom of the Southern Ocean and gradually moves northward into the abyssal Indo-Pacific and Atlantic basins (Talley et al., 2011; Stewart and Hogg, 2017). AABW then gradually upwells via diffusive, mixing-driven exchange with higher buoyancy water in the basin interiors and enters the mid depths, before returning southwards, reentering the Southern Ocean in the mid depths at a lower density than AABW and upwelling to the surface along sloped isopycnals. As with NADW, this upwelled former AABW then either recirculates southwards toward the AABW formation regions or northwards into the intermediate and surface waters of the northern ocean basins.

The Southern Ocean overturning thus plays a crucial role in the dynamics of both overturning cells and is closely linked to the overlying wind stress: powerful Ekman transport at the surface of the Southen Ocean pushes surface waters northwards and results in a divergence at the surface of the ACC, which is in turn balanced by upwelling deep waters south of the wind-stress maximum and downwelling in the north (Toggweiler and Samuels, 1995a). The resulting overturning circulation is known as the Deacon cell and acts to overturn southward flowing water entering the Southern Ocean from the northern basins, leading to a "thermally indirect" vertical circulation in the Southern Ocean. Concurrently, the upward tilting iospycnals in the Southern Ocean result in a buildup of baroclinic potential energy that is released via baroclinic instabilities, rd. eddies, that act to flatten the isopycnal surfaces by transporting water masses southward in the upper ocean (Marshall and Radko, 2003). In

aggregate these eddies result in an eddy-driven overturning circulation that balances the mean wind-driven flow. The sum of the two circulations is called the "residual" overturning circulation and gives a good approximation of the flow along which buoyancy and tracers are advected from the deep ocean to the surface in the real Southern Ocean (Marshall and Speer, 2012).

The Southern Ocean's net effect on the MOC is thus to bring deep waters to the surface and redistribute between the northern basins and the AABW formation sites off the coast of Antarctica, pathways that close the upper limbs of the mid depth and abyssal cells and facilitate water mass exchange between them (Schmitz, 1995). The direction that an upwelled parcel of water travels is thought be largely determined by the surface buoyancy flux in the region it upwells in: water that upwells in regions of net buoyancy loss will densify and thus must reenter the deep ocean via sinking in the AABW regions near Antarctica, while water that experiences net buoyancy gain cannot sink and must travel northwards and join the lighter mode and thermocline water in the northern ocean basins (Ferrari et al., 2014). This results in several possible MOC circulation regimes under Earth's continental configuration, as shown in Figure 1.3, including a) an adiabatic mid-depth overturning associated with the transport of NADW from its formation site, upwelling along isopycnals in the Southern Ocean, buoyancy gain at the surface of the Southern Ocean, and return northwards as intermediate and surface water (Wolfe and Cessi, 2011); b) a diabatic abyssal overturning associated with AABW formation off the coast of Antarctica, transport to the northern basins along the ocean bottom, diabatic upwelling in the basin interiors, return to the Southern Ocean surface along sloped isopycnals, and recirculation towards AABW formation sites; and c) an inter-basin exchange overturning pathway whereby NADW is transported through the Southern Ocean to the Indo-Pacific at depth, upwelled to the surface of the Indo-Pacific, and transported back into the Atlantic Ocean (Ferrari et al., 2017).

In reality the global MOC is probably composed of a combination of the various overturning circulations described by Ferrari et al. (2017), with water masses being mixed and

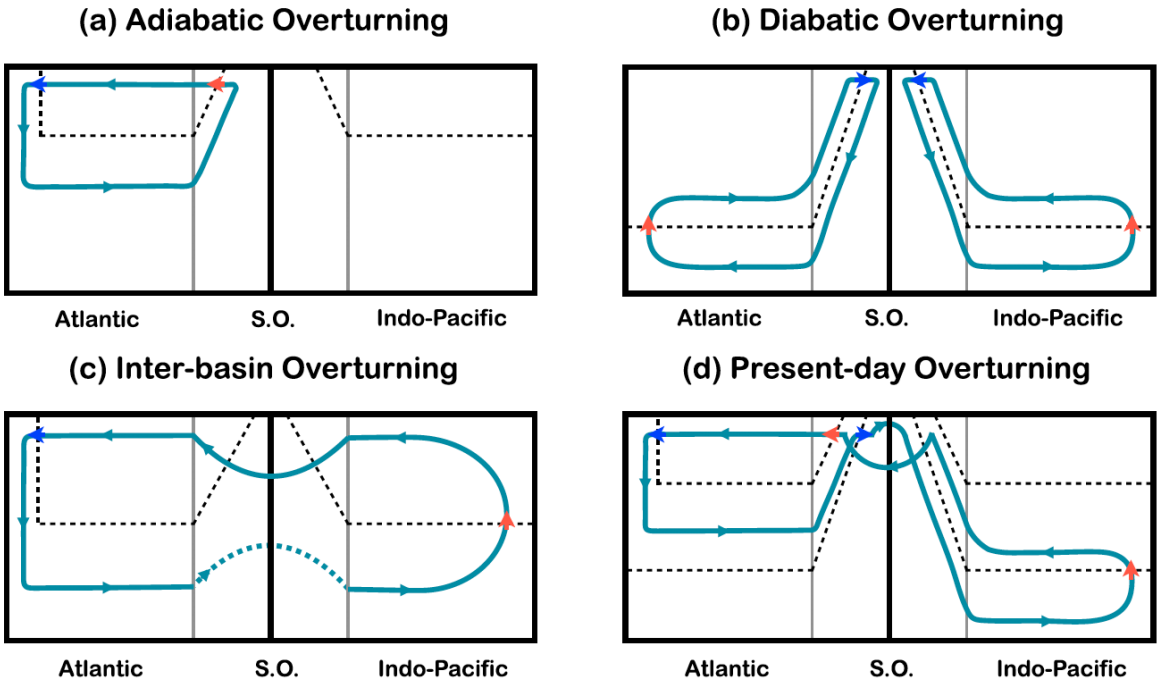

Figure 1.3: Taken from Ferrari et al. (2017): Simplified overturning schematics for the various overturning pathways (blue lines) described in this chapter. The domain of each plot extends northwards away from the Southern Ocean (center portion) to the left (Atlantic), and right (Indo-Pacific) panels, representing the northern basins. The colored arrows give the transformation of water masses at the surface and the interior to lighter (red) and denser (blue) states. The dashed lines are the surfaces of constant density (isopycnals) that separate the intermediate, deep, and abyssal waters.

exchanged between them such as in the "figure-eight" configuration shown in Figure 1.3d. Contemporary observations generally support inter-basin and inter-cell exchanges via the Southern Ocean, such as in the "inter-basin" exchange and "figure-eight" circulations shown above (Lumpkin and Speer, 2007; Talley, 2013; Cessi, 2019; Rousselet et al., 2021), although the specifics of the pathways through which these exchanges are accomplished are difficult to determine from the sparse observations available. Furthermore, the Southern Ocean's extent and zonally continuous geometry allows various water masses to enter and mix at overlapping depths and density classes (Tamsitt et al., 2017), making separating their pathways via hydrographic transects and zonal averaging difficult. Various theoretical configurations to describe the real circulation have been proposed, including the popularized "global ocean conveyor belt" in the 1980s (similar to the regime in 1.3c) and more recently the purely adiabatic (and hence unconnected from the abyssal cell) AMOC proposed by Wolfe and Cessi (2011). However, we still lack an agreed upon picture of the unified global ocean circulation, especially with respect to the circulation pathways of the Southern Ocean.

Recently theorists have begun to extend idealized models of ocean circulation to include intercell/basin exchange (e.g. Thompson et al., 2016; Jones and Cessi, 2016; Nadeau and Jansen, 2020) and it is clear that continuous "figure-eight" loop circulation regimes are possible in simple two-basin setups without topography (1.3 3d) (Ferrari et al., 2017; Nadeau and Jansen, 2020). Thus, the latest theory and numerical experiments generally support the intercell exchange suggested by observations, but only to zeroth order complexity. Importantly, the exact amounts and pathways of NADW that is transformed into AABW versus intermediate water, cycling into the abyssal and mid depth cells respectively via the Southern Ocean, remains uncertain (Ferrari et al., 2017).

Our understanding of the Southern Ocean's role in the MOC is further complicated by recent studies highlighting the important role of zonal topographic asymmetries in the Southern Ocean circulation. The Southern Ocean is home to large outcropping and submarine topographic features, which in turn have been shown to force the large-scale standing meanders

in the ACC (Thompson and Garabato, 2014), polar gyres (Nadeau and Ferrari, 2015; Patmore et al., 2019), and northward AABW export (Stewart and Hogg, 2017). The circulation patterns associated with Southern Ocean topographic features are further thought to carry a significant amount of surface water towards bottom water formation regions (Schröder and Fahrbach, 1999; Reeve et al., 2019) and have recently been shown to play an important role in counteracting the direct response of the ACC and overturning circulation to changes in wind stress (Kong and Jansen, 2021). Studies such as Tamsitt et al. (2017) and Youngs and Flierl (2023) further suggest that deep water upwelling in the Southern Ocean is highly localized near submarine topography, a fact that is obscured in the zonally integrated view and largely ignored in zonally symmetric theory. Furthermore, Southern Ocean circulation features are thought to have climatic importance: studies suggest that meanders adjacent to the Weddell and Ross Gyres likely account for the majority of dissolved inorganic carbon outgassing in the Southern Ocean (Brady et al., 2021) and its southward transport (Ito et al., 2010), and idealized representations of standing meanders have also been associated with significant poleward heat transport (Youngs et al., 2017; Xing et al., 2023) towards AABW formation regions. Thus, proper characterization of the Southern Ocean circulation has significance for both our overall picture of the global ocean circulation and large scale climate, making further investigation into the Southern Ocean's structure and its influence on the MOC of critical importance.

In order to address the gaps outlined above, we here seek to contribute towards a more comprehensive view of the MOC by investigating the MOC's water mass budget in the abyssal ocean and examining the the effect of topographic asymmetries in the Southern Ocean on the overall global ocean circulation in an idealized setting.

1.2 Thesis outline

Here we investigate the drivers of the various limbs of the MOC, the pathways of intercell exchange, and the influence of Southern Ocean submarine topography on the large scale

ocean circulation. We approach this topic in this thesis using a combination of observation and idealized models. A brief outline of this thesis is as follows.

We begin in Chapter 2 by characterizing the major overturning limbs of the MOC in Version 4 Release 4 of the Estimating the Circulation and Climate of the Ocean state estimate reanalysis product (referred to simply as "ECCO" in the text). To do so we employ a water mass budget decomposition (Walin, 1982) of the overturning in each of the major ocean basins. Our results confirm the adiabatic nature of NADW's southward flow through the Atlantic and we further characterize its partitioning into intermediate and abyssal cell deep water at the boundary with the Southern Ocean based on previously established theory (Ferrari et al., 2014; Nadeau and Jansen, 2020). We also find that transient volume change plays a dominant role in ECCO's representation of the deep and abyssal ocean overturning, a result that carries large significance when interpreting ECCO's representation of the real ocean.

In Chapter 3 we use idealized models to investigate the role of Southern Ocean submarine topography in shaping the large scale ocean circulation and the water mass composition of the deep ocean. We employ passive tracers to track the pathways of different deep water masses as they circulate through the MOC, develop novel techniques for estimating the rate of exchange between the overturning cells of the deep ocean and the surface waters of the northern basns, and derive a simple scaling relationship to predict the effect of topography on the composition of the abyssal cell. Our results show that Southern Ocean topography can heavily influence the water mass composition of the abyssal ocean via a) its control over the mid depth cell and b) its influence on the strength of a Southern Ocean gyre. Specifically, the ventilation of the abyssal Indo-Pacific by NADW (and hence the strength of the lower "inter-basin overturning" in Figure 1.3c) is directly proportional to the strength of the mid depth cell, which is in turn controlled by topographic height and Southern Ocean wind stress. Additionally, we identify an "exchange" pathway between the closed overturning circulation and the surface of the northern basins that is tightly controlled by the Southern Ocean gyre,

and characterize it using a simple scaling relationship.

In Chapter 4 we test the robustness of the results identified in Chapter 3 under more complex topographic setups. Our results indicate that, at least in the limited cases explored here, the theory we have developed in Chapter 3 holds up well. The composition of the abyssal ocean under more complex topography remains largely determined by the strength of the mid depth cell and a Southern Ocean gyre, with the abyssal NADW ventilation controlled by mid depth cell strength and the "exchange" pathway remaining closely linked to Southern Ocean gyre spinup.

Chapter 5 concludes this thesis with a discussion of the implications of this research and the scope for future study.

CHAPTER 2

THE GLOBAL OVERTURNING CIRCULATION AND THE ROLE OF NON-EQUILIBRIUM EFFECTS IN ECCO

2.1 Introduction

This chapter focuses primarily on the zonally integrated MOC and its representation in ECCO, a state-of-the-art ocean reanalysis product. As discussed in Chapter 1, we still lack a clear consensus on the exchange rate of volume between the mid depth and abyssal cells, and on the role and rates of diapycnal mixing which governs the interior water mass transformations thought to be critical to maintaining the MOC. Our incomplete understanding of the structure of the deep ocean circulation, and the associated water mass transformations that control its circulation, leads to uncertainty in predicting its role in future and past climate shifts and serves as motivation for this study.

Observational and theoretical evidence supports a large amount of exchange between the mid depth and abyssal cells via the Southern Ocean, although there is some disagreement about the actual magnitude of exchange that occurs. Hydrographic analysis by Talley (2013) suggests that most NADW is converted to abyssal-cell AABW near the coast of Antarctica ($\sim$13Sv), and re-circulates through the abyssal cell before returning into the Atlantic (c.f. Ferrari et al., 2014). Inverse analysis by Lumpkin and Speer (2007) shows a somewhat more even partitioning of NADW between the abyssal cell ($\sim$11Sv) and recirculation within the mid depth cell ($\sim$7Sv) and a similar partitioning was found by Cessi (2019) in the ECCOv4r2 state estimate (spanning 1992-2011). A recent study by Rousselet et al. (2021) utilized ECCOv4r3's climatological mean state to advect Lagrangian drifters along the pathway of NADW in the MOC and found a similar partition of NADW between "upper" (32%) and "lower" (78%) recirculation routes. Rousselet and Cessi (2022) further argued that a portion of NADW densifies and enters the abyssal Indo-Pacific directly at depth, without first upwelling to the surface around Antarctica. The magnitude and structure of the intercell

exchange thus remains a subject of debate.

The previous studies do not explicitly investigate the water mass transformation processes that are necessary to maintain the proposed circulation. A common assumption is that any volume flux convergence below a sub-surface isopycnal is primarily balanced by water mass transformations associated with diapycnal mixing. This is the fundamental assumption underlying idealized models of the deep ocean overturning circulation, such as those developed by Gnanadesikan (1999), Wolfe and Cessi (2011) and Nikurashin and Vallis (2012). In these models, deep water formation in the north is balanced exactly by a combination of wind-driven upwelling along isopycnals in the south, which does not require any interior diapycnal water mass transformations, and diapycnal upwelling in the basin interior, which is balanced by mixing-driven water mass transformations. Bottom water formation around Antarctica, meanwhile, is generally assumed to be driven entirely by mixing-driven upwelling in the basin interiors to the north (Nikurashin and Vallis, 2012). In these models, diapycnal transformations in the deep ocean play a central role in closing the overall MOC. However, such theoretical models hinge on the assumption that the overall circulation is in equilibrium, with diapycnal transport balanced exactly by irreversible water mass transformations either via surface fluxes of heat and freshwater or via diapycnal mixing in the interior.

Whether or not ECCO supports the assumptions of classic equilibrium models of the ocean circulation serves as a major motivation for this study. Studies utilizing earlier ECCO releases such as Wunsch and Heimbach (2014) and Liang et al. (2017) suggest that deep ocean temperature and salinity tendencies are present in the earlier ECCO solutions, although the existing studies do not address the potential role of these tendencies in the MOC and deep ocean water mass budgets. Recent work such as Trossman et al. (2022), meanwhile, has revealed that ECCO's representation of diapycnal mixing in the deep ocean interior is much smaller than mixing rates suggested by microstructure measurements (Waterhouse et al., 2014) and estimates of mixing via internal tide breaking (de Lavergne et al., 2020b). Such

low diapycnal mixing rates may be expected to influence ECCO's representation of the abyssal ocean circulation, yet studies such as Cessi (2019) suggest that the net rates of deep water formation and upwelling in ECCO's ocean basins are generally consistent with observations.

In this study we employ a volume-budget framework to investigate the overturning circulation and water mass transformations in ECCO, paying particular attention to the rate of intercell exchange, the role of diapycnal mixing in the return pathways of deep and bottom water, and whether the common equilibrium assumption holds in ECCO's representation of the present-day ocean. We focus on the basin-wide volume budgets and hence define intercell exchange as the amount of NADW that leaves the Atlantic below the isopycnal that separates the mid depth and abyssal cells in the Southern Ocean, which has to be balanced by a similar amount of upwelling in the Indo-Pacific (Nadeau et al., 2019). This quantity measures the net exchange of volume between the overturning cells and basins, although it does not reveal the pathways taken by individual water parcels (for which readers should refer to Rousselet et al. (2021) and Rousselet and Cessi (2022)). In each basin, we then apply an isopycnal volume budget decomposition based on Walin (1982) (see also Lee et al. (2002), Urakawa and Hasumi (2014), Newsom et al. (2016), and Megann (2017)) which allows us to decompose any net up- or down-welling into specific water mass transformation processes and/or isopycnal volume tendencies.

Our results generally support the interconnected view of the MOC, with a large amount of exchange between the mid depth and abyssal cells, roughly in line with existing theory and observations. However, the water mass budget also shows that ECCO's deep ocean is not in equilibrium and that isopycnal volume changes associated with trends in the deep ocean density play a major role in the deep ocean water mass budgets.

2.2 Methods

2.2.1 The ECCO State Estimate

We analyze monthly-mean results taken from the ECCO ocean state estimate (Forget et al., 2015; ECCO Consortium et al., 2021, 2022). The ECCO setup comprises a non-linear inverse modeling framework utilizing MITgcm (Marshall et al., 1997b) in conjunction with the adjoint method (Forget and Ponte, 2015) to produce an optimized solution of the hydrostatic Boussinesq equations fit to a suite of oceanographic data spanning a 26-year time period from 1992 to 2017 (ECCO Consortium et al., 2021). The model component of ECCO uses the Lat-Lon-Cap 90 (LLC90) grid with a latitudinally-varying horizontal resolution between approximately 20km-40km at 80^oN/S to 110km at 10^oN/S. Further details about the ECCO state estimate are provided in Forget et al. (2015) and ECCO Consortium et al. (2021).

2.2.2 The Meridional Overturning Circulation in Potential Density Coordinates

In order to evaluate the overall volume budgets of the global ocean circulation we employ the isopycnal streamfunction, $\Psi(y, \sigma_2)$, as a function of latitude (y) and potential density referenced to 2000dbar (σ_2). We choose σ_2 because it corresponds to the approximate average local pressure of NADW within the Atlantic interior and has been used previously by Rousselet et al. (2021) and Rousselet and Cessi (2022). $\Psi(y, \sigma_2)$ is defined as the zonally and vertically integrated sum of the resolved meridional transport field, $\mathbf{v}(x, y, z, t)$, and the parameterized meridional eddy transport, $\mathbf{v}^*(x, y, z, t)$, from the ocean bottom to a given σ_2 surface. Since the ECCO fields are given in z-space, we begin our analysis by calculating the local streamfunction, $\psi(x, y, \sigma_2, t)$, by vertically integrating the transport to a vertical σ_2 grid:

$$\psi(x, y, \sigma_2, t) = \int_{-H(x,y)}^{z(x,y,\sigma_2,t)} \mathbf{v}(x, y, z, t) + \mathbf{v}^*(x, y, z, t) dz, \tag{2.1}$$

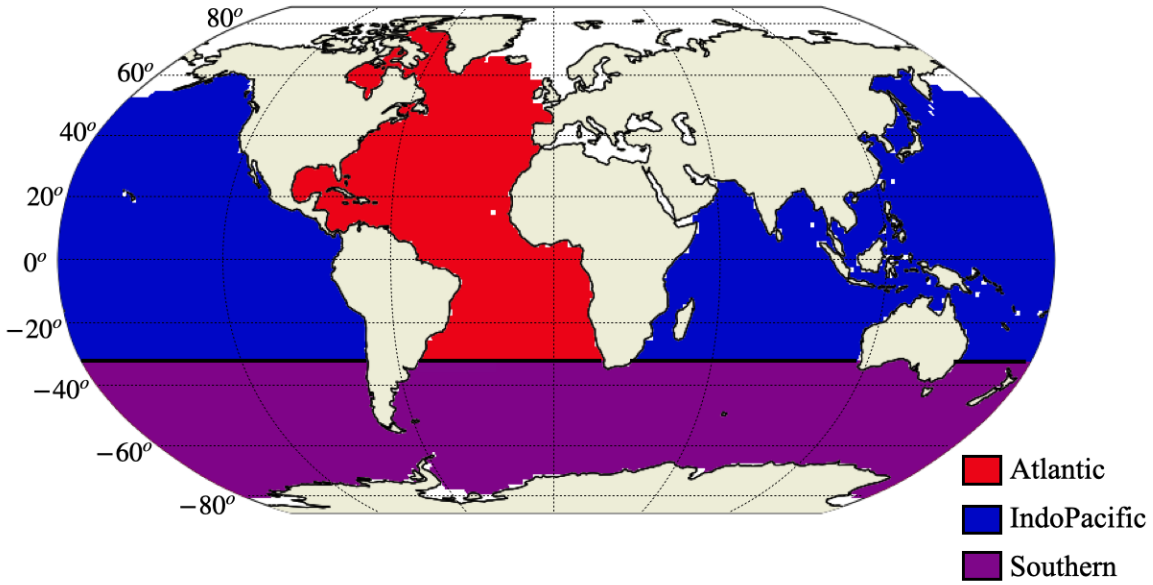

Figure 2.1: Basin masks used for subdividing the global ocean. The Atlantic basin (red) extends from 32^oS north into the Labrador and Baffin seas. The Indo-Pacific basins (blue) are considered together and extend from 32^oS to the Aleutians in the North. The Southern Ocean (purple) is bounded in the north at 32^oS and extends to the coast of Antarctica. Note that the basin masks shown here do not include the poleward limits of the interior volumes considered in section 3 that are imposed by the outcrops of isopycnal surfaces into the surface layer, whose locations vary depending on the density surface under consideration.

where $H(x, y)$ denotes the ocean depth and $z(x, y, \sigma_2, t)$ gives the depth of an isopycnal surface σ_2 at a particular location, found by linearly interpolating σ_2 between vertical grid points. The vertical integral in 2.1 is performed on the native model grid, before linearly interpolating ψ to the height of a given isopycnal $z(x, y, \sigma_2, t)$. Note that technique is similar to Ferrari and Ferreira (2011) and perfectly preserves the meridional mass transport in each column. To test the sensitivity of our results to the interpolation method we repeated our analysis without any interpolation (i.e. the integral in 2.1 simply includes all gridboxes with potential density smaller than the specified σ_2 level, which amounts to assuming a piece-wise constant rather than piece-wise linear density profile) (see Appendix). Differences between the two methods were found to be on the order of 1% and hence do not affect our conclusions Next, we integrate $\psi(x, y, \sigma_2, t)$ in the zonal and take the time average:

$$\Psi(y, \sigma_2) = \overline{\int_{x_0(y)}^{x_1(y)} \psi(x, y, \sigma_2, t) dx}, \tag{2.2}$$

where $\int_{x_0(y)}^{x_1(y)} dx$ gives the zonal integral at a given latitude y across an ocean basin bounded by longitudes x_0 and x_1, and $\overline{(\cdot)}$ denotes the time-average of the enclosed quantity over the full ECCO time period. We calculate $\Psi(y, \sigma_2)$ across three ocean basins: the Atlantic, Southern, and Indo-Pacific Oceans, which in turn are divided by the continents and the 32^oS parallel (Figure 2.1). Note that in order to remove contributions from the North Sea circulation to the AMOC streamfunction we exclude regions East of the Greenland-Iceland-Scotland (GIS) ridge system from our Atlantic mask (Figure 2.1). Notice that all isopycnals either out-crop into the surface layer or in-crop into the seafloor before reaching the open boundary at the GIS ridge system. As a result the overflows do not affect the interior volume budgets presented in Section 2.3

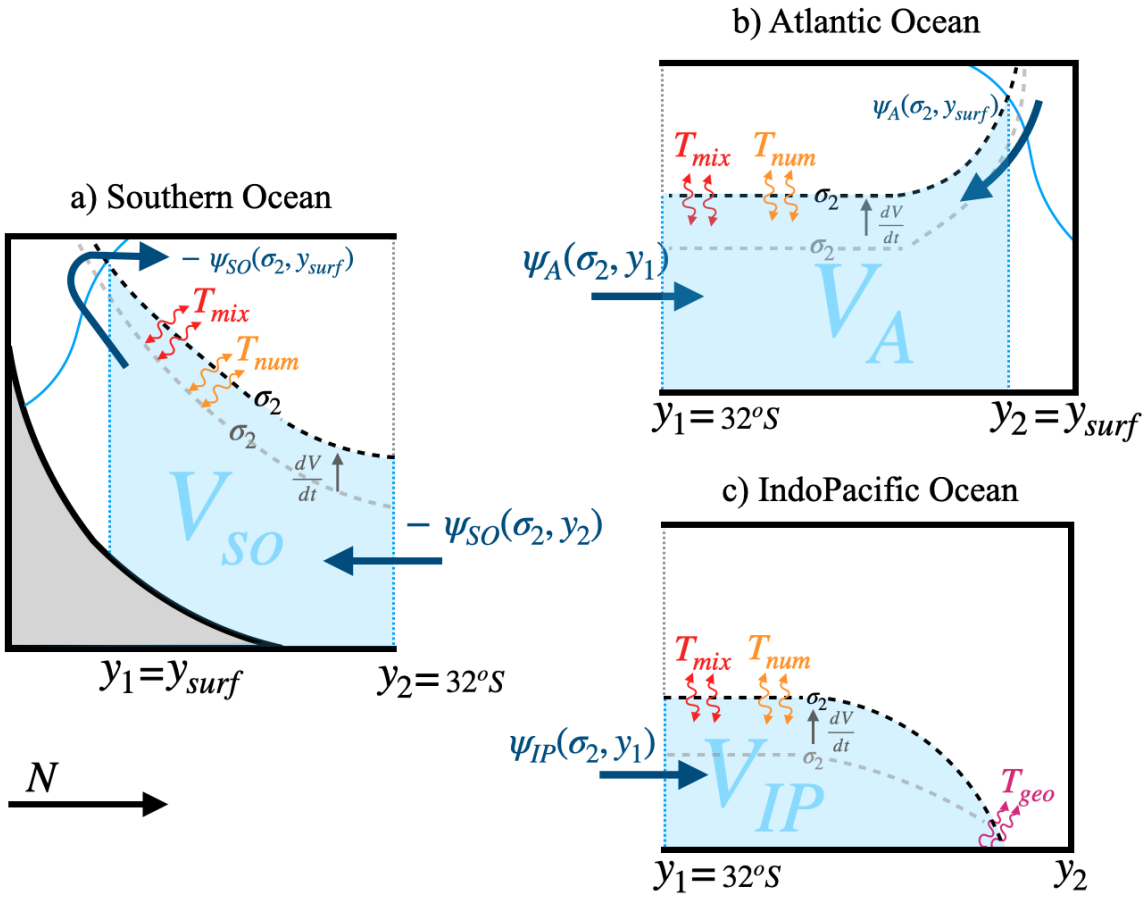

Figure 2.2: Schematic of the water-mass-transformation framework used in this study, applied to the Atlantic (subscript A), Indo-Pacific (subscript IP), and Southern Ocean (subscript SO). Black dashed lines indicate an isopycnal surface of density σ_2. Transports into and out of isopycnal volumes are indicated by arrows, with dark blue indicating net advective flux ($\Psi(y, \sigma_2)$), red the transport balanced by explicit diapycnal diffusion (T_{mix}), orange the transport balanced by numerical diffusion (T_{num}), purple transport balancing geothermal heating (T_{geo}), and grey apparent diapycnal transport balanced by volume change (dV/dt). Latitudes defining the southern and northern meridional bounds of the ocean basins are given by dotted blue lines and labeled y_1 and y_2, respectively, and the latitude where the isopycnal intersects with the surface layer is given by y_{surf}. The bottom of the surface layer is indicated by solid blue lines.

2.2.3 Volume Budget Decomposition in the Interior

We employ an isopycnal volume-budget analysis based on Walin (1982) and Newsom et al. (2016) to diagnose the processes that balance diapycnal advection within the large-scale circulation in ECCO (Figure 2.2). We consider a volume flux balance of a volume of ocean, $V(y_1, y_2, \sigma_2)$, bounded above by an isopycnal of density σ_2, in the zonal direction by continental boundaries, and in the meridional by the latitudes y_1 in the south and y_2 in the north. We define the bottom of the surface layer as the maximum surface potential density at or equatorwards of any given latitude over the zonal width of the basin and the entire ECCO time period (i.e., the bottom of the surface layer does not depend on time or longitude). Following volume conservation, the total meridional transport in and out of the volume below any given isopycnal can be expressed as the sum of the volume tendency and various water mass transformation processes at the bounding isopycnal:

$$\begin{aligned}\Delta\Psi = \overline{\frac{d}{dt}V(y_1, y_2, \sigma_2, t)} \; + \; \overline{T_{geo}(y_1, y_2, \sigma_2, t)} \; + \; \overline{T_{plume}(y_1, y_2, \sigma_2, t)} \\ + \; \overline{T_{mix}(y_1, y_2, \sigma_2, t} \; + \; \overline{T_{num}(y_1, y_2, \sigma_2, t)} \; + \; \overline{R(y_1, y_2, \sigma_2, t)}.\end{aligned} \tag{2.3}$$

Here $\Delta\Psi = \Psi(y_2, \sigma_2) - \Psi(y_1, \sigma_2)$ is the net transport across the northern and southern boundaries which must, by volume conservation, be balanced by the terms on the RHS (see also Figure 2.2).

$\overline{\frac{d}{dt}V(y_1, y_2, \sigma_2, t)}$ is the time-averaged change in the total volume itself resulting from any net volume convergence below a given isopycnal:

$$\frac{d}{dt}V(y_1, y_2, \sigma_2, t) = \frac{d}{dt}\iint_{A_{\sigma_2}(y_1, y_2)} h(x, y, \sigma_2, t)dA, \tag{2.4}$$

where $h(x, y, \sigma_2, t) = z(x, y, \sigma_2, t) + H(x, y)$ is the height of the isopycnal above the ocean bottom and $A_{\sigma_2}(y_1, y_2)$ is the basin area bounded in the south and north by y_1 and y_2, respectively.

$T_{geo}(y_1, y_2, \sigma_2, t)$ is the diapycnal transport balanced by geothermal heating:

$$T_{geo}(y_1, y_2, \sigma_2, t) = -\frac{\partial}{\partial \sigma_2} \iint_{A_I(y_1, y_2, \sigma_2, t)} \frac{\alpha Q_{geo}(x, y)}{c_p} dA, \tag{2.5}$$

where $A_I(y_1, y_2, \sigma_2, t)$ is the area where the bottom density $\sigma_{2bottom} \geq \sigma_2$ within the domain bounded by y_1, y_2 and the sides of the basin, $Q_{geo}(x, y)$ is the geothermal heat flux at the ocean floor, $\alpha = -\frac{1}{\sigma_2}\frac{\partial \sigma_2}{\partial \theta}$ is the thermal expansion coefficient, and c_p is the heat capacity of seawater (see de Lavergne et al. (2016) for a full derivation). The integral in 2.5 is computed on the model grid over small σ_2 bins following Abernathey et al. (2016, SI (S11)).

T_{plume} gives the watermass transformation due to salt plume forcing (a parameterized in-situ forcing in ECCO), and is computed as

$$T_{plume}(y_1, y_2, \sigma_2, t) = \frac{\partial}{\partial \sigma_2} \iiint_{V(y_1, y_2, \sigma_2, t)} \frac{\partial \sigma_2}{\partial S} \dot{S}_{plume}(y_1, y_2, \sigma_2, t) dV, \tag{2.6}$$

where $\dot{S}_{plume}$ is the salinity tendency (psu/s) due to in-situ salt plume flux, which is only significant in the Southern Ocean. The integral above is again taken on the model grid before interpolating to σ_2 levels.

$T_{mix}(y_1, y_2, \sigma_2, t)$ represents the water mass transformation rate due to explicitly parameterized diapycnal mixing. Note that in addition to background vertical diffusion, which is optimized as part of the ECCO inversion, T_{mix} contains mixing contributions from parameterized mixing due to the Gaspar, Gregoris, and Lefevre (GGL) scheme (Gaspar et al., 1990), isoneutral mixing when the local neutral slope is not aligned with the slope of the σ_2 surface, and horizontal mixing in the presence of slope-clipping along steep isopycnals. (The MITgcm configuration used for ECCO employs a slope clipping scheme that limits the effective isopycnal slope used in the Gent and Mcwilliams (1990) and Redi (1982) parameterizations to a maximum value of $2 \cdot 10^{-3}$. When this maximum slope is exceeded, mixing is no longer isoneutral.) All of these terms contribute to diapycnal mixing but their individual contributions are difficult to diagnose explicitly. We derive T_{mix} from the diffusive

tendencies of temperature and salinity as:

$$T_{mix}(y_1, y_2, \sigma_2, t) = \frac{\partial}{\partial \sigma_2} \iiint_{V(y_1,y_2,\sigma_2,t)} \frac{\partial \sigma_2}{\partial \theta} \dot{\theta}_{mix}(x, z, y, t) + \frac{\partial \sigma_2}{\partial S} \dot{S}_{mix}(x, z, y, t) dV, \quad (2.7)$$

where $\dot{\theta}_{mix}(x, z, y, t)$ and $\dot{S}_{mix}(x, z, y, t)$ are the temperature and salinity tendencies due to diffusive flux convergence, respectively. $\dot{\theta}_{mix}(x, z, y, t)$ and $\dot{S}_{mix}(x, z, y, t)$ can be computed exactly based on ECCO diagnostics, as discussed in Piecuch (2017). As in equations 2.1 and 2.6 the vertical integral is taken on the model grid before interpolating to σ_2 levels.

Additionally, we must take into account the effects of numerical diffusion associated with inaccuracies in ECCO's advection scheme, T_{num}. Numerical diffusion is an inherent property of z-space ocean models such as ECCO, and can reach comparable magnitude to explicit mixing (Griffies et al., 2000; Lee et al., 2002). Previous studies have estimated numerical diffusion simply as the residual of the volume budget described above (Lee et al., 2002; Urakawa and Hasumi, 2014), Megann (2017)). Here, we take a slightly more direct path and characterize the contribution from numerical diffusion as the residual between the advective flux derived from the diagnosed density tendency due to the advection scheme and the flux implied by the net volume transport across the volume's horizontal boundaries, $\Delta\Psi$:

$$T_{num}(y_1, y_2, \sigma_2, t) = \Delta\Psi + \frac{\partial}{\partial \sigma} \iiint_{V(y_1,y_2,\sigma_2,t)} \frac{\partial \sigma_2}{\partial \theta} \dot{\theta}_{adv}(x, z, y, t) + \frac{\partial \sigma_2}{\partial S} \dot{S}_{adv}(x, z, y, t) dV, \quad (2.8)$$

where $\dot{\theta}_{adv}(x, z, y, t)$ and $\dot{S}_{adv}(x, z, y, t)$ are the temperature and salinity tendencies due to the advection scheme, which can be calculated from the ECCO diagnostics (Piecuch, 2017), and include any numerical diffusion arising from the discretization (See Appendix A for further details). This approach is particularly suited to ECCO, where the θ and S budgets can be closed exactly.

The final term in 2.3, $R(y_1, y_2, \sigma_2, t)$, is the residual and reflects inaccuracies in our volume

budget computation. By applying 2.3 to specific domains of interest, we can estimate the major drivers of interior water mass transformations that balance any net up- or down-welling across the different basins. It should be noted that an additional contribution from shortwave penetrating flux is included in the ECCO model and can in theory have an effect below the surface layer, as defined here, but was found to be negligible in our budget.

We can further decompose the isopycnal volume tendency itself to determine the individual contributions from changes in the temperature and salinity of the deep ocean:

$$\overline{\frac{d}{dt}V(y_1, y_2, \sigma_2, t)} = -\overline{T_\Theta(y_1, y_2, \sigma_2, t)} - \overline{T_S(y_1, y_2, \sigma_2, t)} - \overline{R(y_1, y_2, \sigma_2, t)}, \tag{2.9}$$

where $-T_\Theta(y_1, y_2, \sigma_2, t)$, $-T_S(y_1, y_2, \sigma_2, t)$ are the individual volume tendencies due to the temperature- and salinity-driven buoyancy tendencies, respectively:

$$\begin{aligned} T_\Theta(x, y, z, t) &= \frac{\partial}{\partial \sigma} \iiint_{V_{\sigma_2}} \frac{\partial \sigma}{\partial \theta} \dot{\theta}(x, y, z, t) dV \\ T_S(x, y, z, t) &= \frac{\partial}{\partial \sigma} \iiint_{V_{\sigma_2}} \frac{\partial \sigma}{\partial S} \dot{S}(x, y, z, t) dV. \end{aligned} \tag{2.10}$$

As previously, the term $R(y_1, y_2, \sigma_2, t)$ in 2.9 is the residual due to any disagreement between the volume tendency we infer directly from 2.4 and indirectly from the density tendencies in 2.9. Because the temperature and salinity budgets in ECCO can be closed exactly, it can be shown that $R(y_1, y_2, \sigma_2, t)$ in 2.9 is the same as $R(y_1, y_2, \sigma_2, t)$ in 2.3. Here we find that $R(y_1, y_2, \sigma_2, t)$ is generally small.

2.3 Results

2.3.1 The isopycanl overturning in ECCO

The isopycnal overturning in ECCO (Figure 2.3) is in broad agreement with that derived in other studies (e.g. Lumpkin and Speer, 2007; Cessi, 2019) and the magnitudes of the overturning cells generally fall within uncertainties established by observation-based estimates (Lumpkin and Speer, 2007; Talley, 2013; Kunze, 2017), as previously found for ECCOv4r2 by Cessi (2019). The mid depth cell occupies the Atlantic with a peak overturning strength of 17.2Sv occurring at 55^oN, in good agreement with other estimates (Lumpkin and Speer, 2007; Talley, 2013). The abyssal cell dominates the Indo-Pacific and the lower part of the Southern Ocean and peaks at approximately 14.4Sv at 36^oS, a substantially weaker value than that derived by Lumpkin and Speer (2007) (20Sv), Talley (2013) (29Sv), and Kunze (2017) (20Sv), but similar to the estimates of de Lavergne et al. (2016) (10-15Sv). The abyssal cell in our analysis is also weaker than the value reported in Cessi (2019) (20Sv, at 30S) using ECCO version 4 release 2.

The net exchange of volume between the Atlantic's mid depth cell and the abyssal cell can be found by considering the overlap between the Atlantic, Indo-Pacific and Southern Ocean overturning stream functions at 32^oS (c.f. Nadeau et al., 2019). In ECCO, 14.2Sv of NADW exit the Atlantic at 32^oS, of which 4.6Sv enter the Southern Ocean at density classes occupied by the mid depth cell ($\sigma_2 < 1036.95 kg/m^3$), while 9.6Sv of NADW enter the Southern Ocean in the density range of the abyssal cell ($\sigma_2 \geq 1036.95 kg/m^3$) and hence must be balanced by a similar amount of upwelling in the Indo-Pacific. Large-scale diapycnal transport is visible beneath the surface layer in all ocean basins (Figure 2.3, Figure 2.4). In the Atlantic, $\sim$1.2Sv of NADW upwells diabatically at σ_2=$1036.6 kg/m^3$ and returns to the surface within the North Atlantic. Denser NADW downwells over the length of the Atlantic yielding around 8.1Sv of downwelling at σ_2=$1036.95 kg/m^3$ (Figure 2.3a). The Indo-Pacific, meanwhile, is dominated by the abyssal cell with an upwelling of 14.4Sv at $\sigma_2 = 1037.053 kg/m^3$. Of

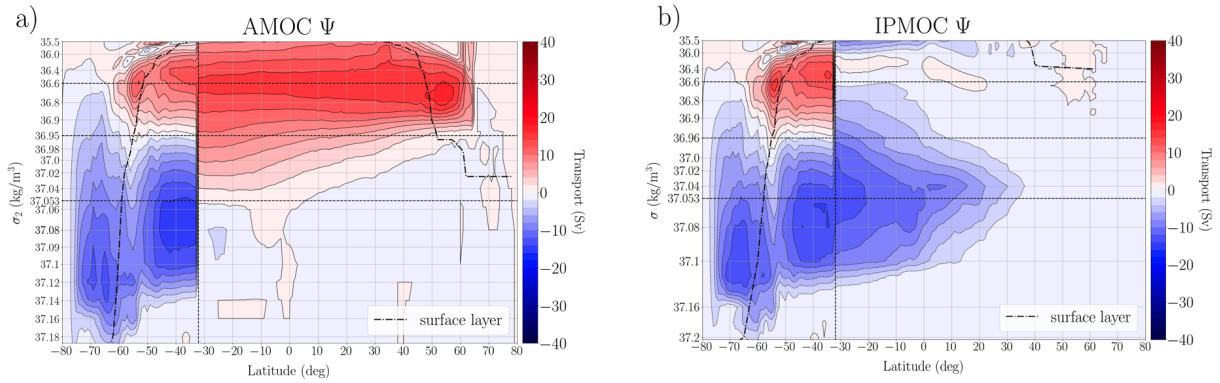

Figure 2.3: Atlantic, Indo-Pacific, and Southern Ocean stream functions in potential density space (referenced to 2000dbar), calculated from ECCO and averaged over the full ECCO time period (1992-2017). a) Atlantic Meridional Overturning Circulation (AMOC) and b) Indo-Pacific Meridional Overturning Circulation (IPMOC). The Southern Ocean Meridional Overturning Circulation is plotted in both a) and b) south of 32^oS. Positive (red) denotes clockwise flow and negative (blue) denotes counterclockwise flow (CL=2Sv). The dash-dotted line indicates the bottom of the surface layer (see text). The vertical dashed line indicates the northern end of the Southern Ocean at 32^oS. Horizontal dashed lines denote specific density surfaces of interest: the upper bound of southward-flowing NADW entering the Southern Ocean: σ_2=1036.6kg/m^3, the division between the mid depth and lower cells in the Southern Ocean: σ_2=1036.95kg/m^3, and the maximum density of NADW entering the Southern Ocean: σ_2=1037.053kg/m^3. The density-axis is stretched to reflect the average isopycnal depth within the Atlantic for σ_2<1037.1kg/m^3 (the maximum density in the Atlantic) and is extended linearly to the highest densities in the Southern Ocean. The same density axis is used in subsequent plots. Note that the AMOC stream function is not well defined north of 60N and above $\sigma_2\sim$1036.9kg/m^3 due to open zonal boundaries along the Greenland-Iceland-Scotland ridge system.

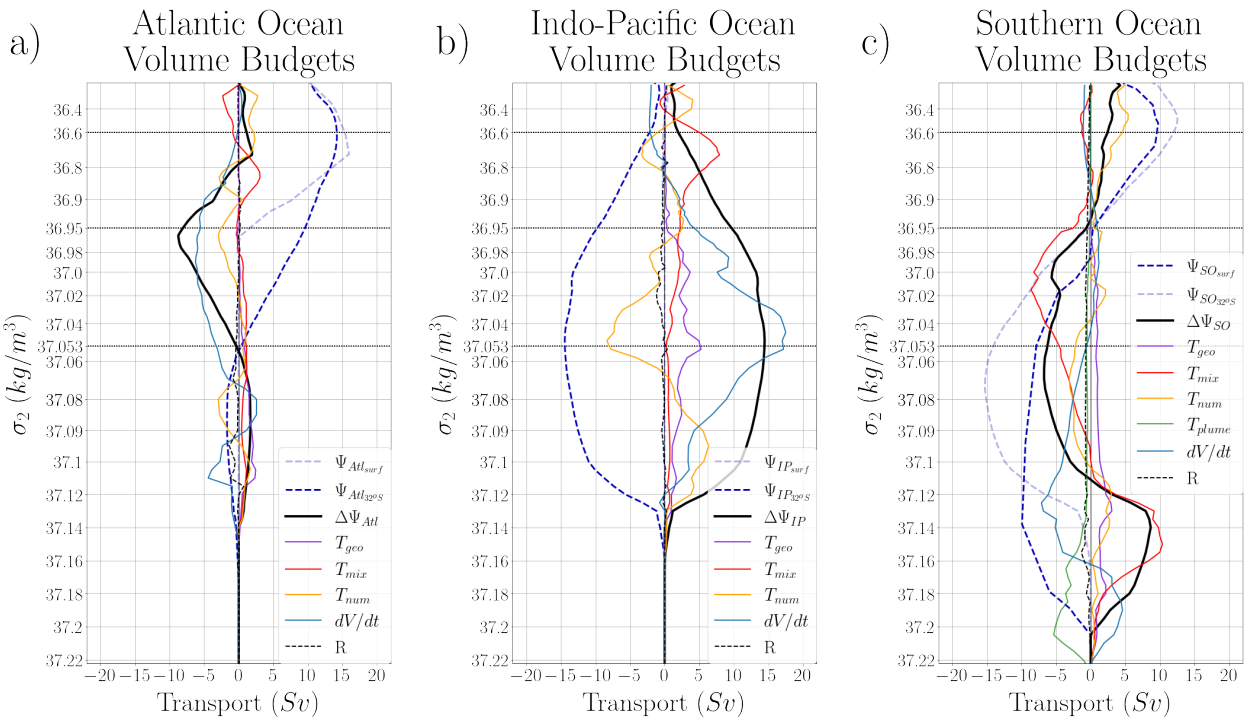

Figure 2.4: Volume budget decompositions over the Atlantic Ocean a), Indo-Pacific Ocean b), and Southern Ocean c). Solid black lines denote net diapycnal transport at each density surface, inferred from the difference between Ψ across each region's northern (dashed light blue) and southern (dashed dark blue) boundaries. The subscript $Surf$ refers to the stream function at the bottom of the surface layer, defined by the minimum surface density at a given latitude (Figure 2.2). The net diapycnal transport (solid black) is decomposed into contributions from: geothermal transformations (T_{geo}, solid purple), explicit mixing (T_{mix}, solid red), numerical diffusion (T_{num}, solid orange), isopycnal volume change (dV/dt, solid cyan), and transport due to buoyancy tendencies from salt plume flux forcing (T_{plume}, solid green) which is only significant in the Southern Ocean. R (dashed black) gives the residual.

the abyssal circulation that returns to the Southern Ocean, 4.8Sv enter at densities below $\sigma_2 = 1036.95\text{kg/m}^3$ and recirculate through the abyssal cell while the remaining 9.6Sv return in the buoyancy range of the mid depth cell, balancing the transfer of NADW into the abyssal cell.

2.3.2 Volume Budget and water mass Transformations

We now examine the isopycnal volume budgets in the Atlantic, Indo-Pacific, and Southern Ocean interiors in order to identify the water mass transformation processes associated with

the deep ocean circulation. As above, we primarily focus on the net transformations across the isopycnals $\sigma_2 = 1036.6 kg/m^3$ (marking the maximum of the mid depth cell in the South Atlantic), $\sigma_2 = 1036.95 kg/m^3$ (marking the division between the mid depth and abyssal cell at $32^o S$), and $\sigma_2 = 1037.053 kg/m^3$ (marking the bottom of NADW in the South Atlantic as well as the maximum of the abyssal cell in the Indo-Pacific). We find that volume tendency plays a leading role in driving diabatic water mass transformations across these isopycnals in all basins, while, surprisingly, explicit mixing-driven upwelling is relatively small in both the deep Atlantic and Indo-Pacific.

In the Atlantic, we see a small net upwelling signal at $\sigma_2 = 1036.6 \text{kg/m}^3$ (1.2Sv) which is primarily due to numerical diffusion (2.2Sv), partially compensated by explicit mixing (-0.9Sv) and volume tendency (-0.2Sv). Deeper in the Atlantic, the diapycnal downwelling of NADW at $\sigma_2 = 1036.95 \text{kg/m}^3$ (-8.1Sv) is associated primarily with the volume tendency term, dV/dt (-5.5Sv), with a smaller contribution associated with numerical diffusion (-2.6Sv). Net diabatic transformations in the Atlantic at $\sigma_2 = 1037.053 \text{kg/m}^3$, meanwhile, are quite small (-0.73Sv) with a compensation between a negative volume tendency signal (-3.6Sv) and small positive contributions from numerical diffusion (0.9Sv), explicit mixing (1.0Sv), and geothermal heating (0.7Sv).

In the Indo-Pacific, the volume tendency contribution again dominates, particularly over the depth range of the abyssal cell. The upper Indo-Pacific contains only a small amount of net transport (2.0Sv) at the $\sigma_2 = 1036.6 \text{kg/m}^3$ isopycnal, where the effect of explicit mixing (5.0Sv) is largely balanced by volume tendency (-2.1Sv) and numerical diffusion (-1.1Sv). Indo-Pacific upwelling at $\sigma_2 = 1036.95 \text{kg/m}^3$ is much larger (9.7Sv), and is primarily associated with a volume tendency (4.3Sv), with additional contributions from numerical diffusion (2.5Sv) and explicit mixing (2.2Sv) and a small contribution from geothermal heating (0.8Sv). Diapycnal upwelling in the Pacific peaks near $\sigma_2 = 1037.053 \text{kg/m}^3$ where it reaches 14.5 Sv. This upwelling is primarily balanced by the volume tendency term, contributing to 17.0Sv, with a smaller contribution from geothermal heating (3.3Sv), and substantial compensation

associated with numerical diffusion (-8.4Sv). Numerical diffusion also plays a large role in the densest regions of the Indo-Pacific, peaking at 6.4Sv at around $\sigma_2 = 1037.053\text{kg/m}^3$.

In the Southern Ocean, volume tendency, numerical diffusion, and explicit mixing all play major roles. Upwelling at $\sigma_2 = 1036.6\text{kg/m}^3$ in the interior Southern Ocean (2.4Sv) is associated with numerical diffusion (4.6Sv), with compensating contributions from explicit mixing (-1.3Sv) and volume tendency (-1.0Sv). Interior transformations across $\sigma_2 = 1036.95\text{kg/m}^3$ are small. Transformations at the $\sigma_2 = 1037.053\text{kg/m}^3$ isopycnal in the Southern Ocean yield a net interior downwelling of -6.2Sv which is primarily driven by explicit mixing (-4.9Sv). It should be noted as well that a large amount of mixing-driven up- and down-welling is present in the abyssal Southern Ocean and is likely related to slope-clipping along steep isopycnals in the isopycnal mixing scheme[1]. Transformations due to salt plume forcing are also prevalent in the densest regions of the Southern Ocean, contributing -5.4Sv at the $\sigma_2 = 1037.205\text{kg/m}^3$ isopycnal, and are primarily balanced by a volume tendency.

2.3.3 Volume Tendency Decomposition

The importance of the dV/dt terms that we observe in ECCO's overturning circulation merits further discussion. These volume tendencies are associated with density trends, which in turn can be decomposed into temperature and salinity trends. The decomposition of the isopycnal volume tendencies into contributions from temperature and salinity trends, together with the associated temperature and salinity trends themselves are shown in Figure 2.5.

In the Atlantic, the most notable feature of the volume tendency is a strong isopycnal deepening in the depth range of the lower limb of the AMOC between $\sigma_2 = 1036.6\text{kg/m}^3$ and $\sigma_2 = 1037.07\text{kg/m}^3$, which is associated with a basin-averaged warming of $0.08C^o$ over the 24-year ECCO time period. The Atlantic also exhibits a small amount of cooling in the lower density ranges of the abyssal ocean, amounting to $-0.002C^\circ$ over the ECCO period,

1. In ECCO's representation of the Southern Ocean isopycnal slopes frequently exceed the model's slope clipping threshold of $4 \cdot 10^{-3}(kg/m^3)/m$.

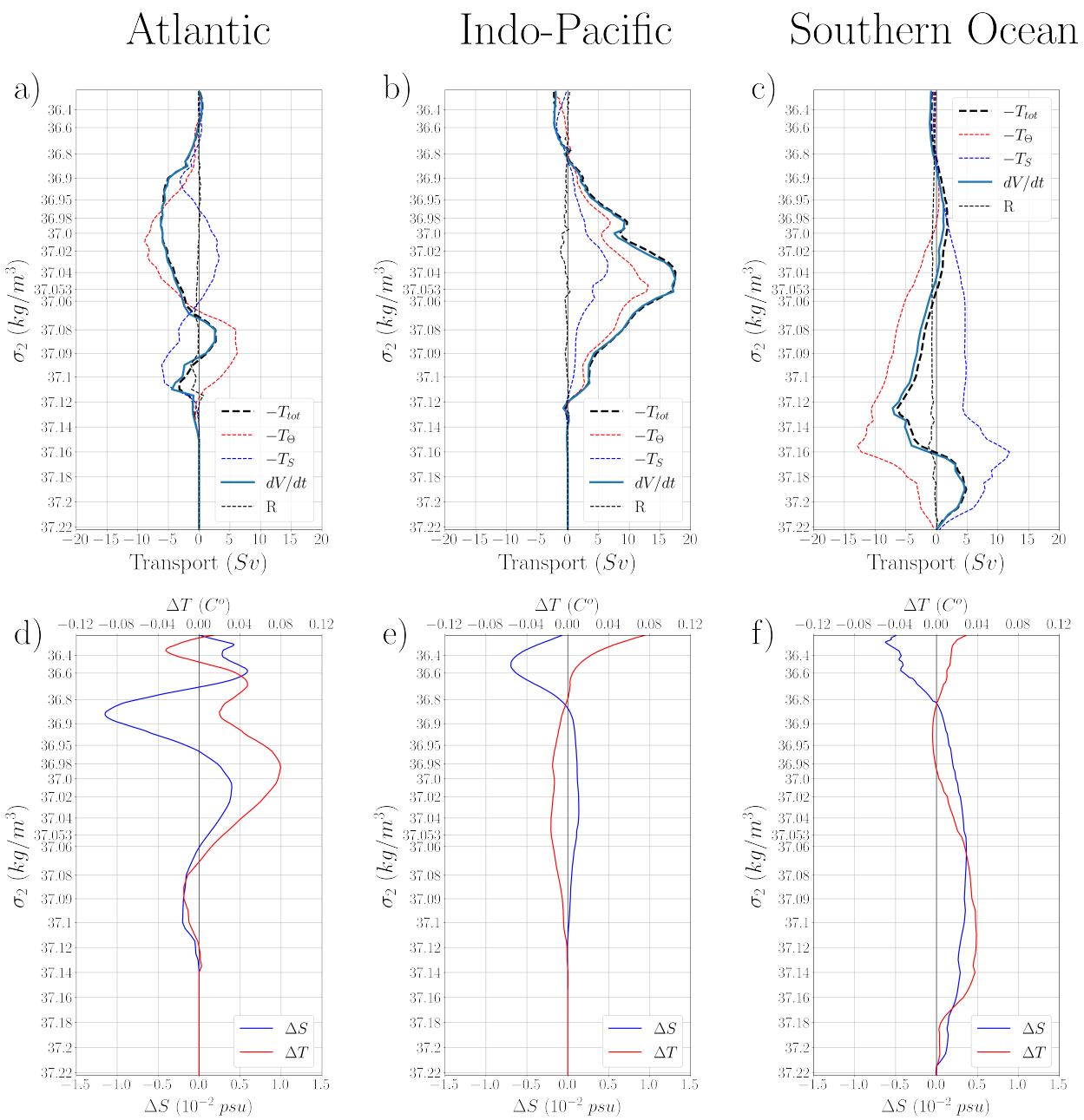

Figure 2.5: Volume tendency decompositions and net temperature and salinity changes over the ECCO time period (1992-2017) across the Atlantic Ocean (a, d), Indo-Pacific Ocean (b, e), and Southern Ocean (c, f). In (a), (b), and (c), total isopycnal volume change (solid cyan, Figure 2.4) across each basin is shown together with the estimated volume change from the total buoyancy tendency, $-T_{tot}$=$-T_\Theta-\ T_S$ (c.f. Eq. 9, bold dashed black), and its temperature and salinity components, $-T_\Theta$ and $-T_S$ (thin dashed red and thin dashed blue, respectively). Panels (d) to (f) show the corresponding basin-averaged temperature (ΔT, red) and salinity (ΔS, blue) changes over the 26-year ECCO time period.

although this trend is partially compensated by a salinity-driven lightening that dominates below $\sigma_2 = 1037.09\text{kg/m}^3$.

In the Indo-Pacific, cooling plays the leading role in the isopycnal shoaling between $\sigma_2 = 1036.8\text{kg/m}^3$ and $\sigma_2 = 1037.12\text{kg/m}^3$, the main density range of the abyssal cell. Here, a basin-averaged cooling of about $0.016C^\circ$ occurs over the ECCO period and accounts for -13.1Sv of abyssal upwelling at $\sigma_2 \sim 1037.05$. Volume tendency due to salinity trends also drive densification in the Indo-Pacific, peaking at -6.5Sv at $\sigma_2 \sim 1037.035$ and corresponding to a basin-averaged increase in salinity of around 0.001 psu over the ECCO period.

The deep Southern Ocean is warming and salinifying in ECCO. The trends have partially compensating effects on the density and hence the isopycnal volume budget. Temperature-driven isopycnal deepening peaks at 12.9Sv at $\sigma_2 \sim 1037.157$ and is associated with a basin-averaged warming of around $0.03C^\circ$ over the ECCO period, while salinity-driven isopycnal shoaling peaks at -11.88Sv at $\sigma_2 \sim 1037.16$, corresponding to a basin-averaged salinity increase of around 0.001 psu over the ECCO period. Note that the salinity trend below $\sigma_2 = 1037.18\text{kg/m}^3$ appears to be primarily associated with the salt plume forcing (Figure 2.4).

2.4 Summary and Discussion

ECCO supports an interconnected view of the MOC (summarized in Figure 2.6), with substantial linkages between the AMOC and the abyssal cell. It is clear that substantial diapycnal upwelling (or isopycnal rising) in the Indo-Pacific is needed to balance the inflow of dense NADW into the Southern Ocean. We also find significant up- and down-welling within the Atlantic, the latter of which is not typically included in idealized depictions of the mid depth cell.

In both the Indo-Pacific and Atlantic ocean basins, much of the net up- and down-welling is primarily balanced by isopycnal volume changes, rather than mixing-driven water mass transformations as usually assumed in theoretical models. The associated isopycnal depth

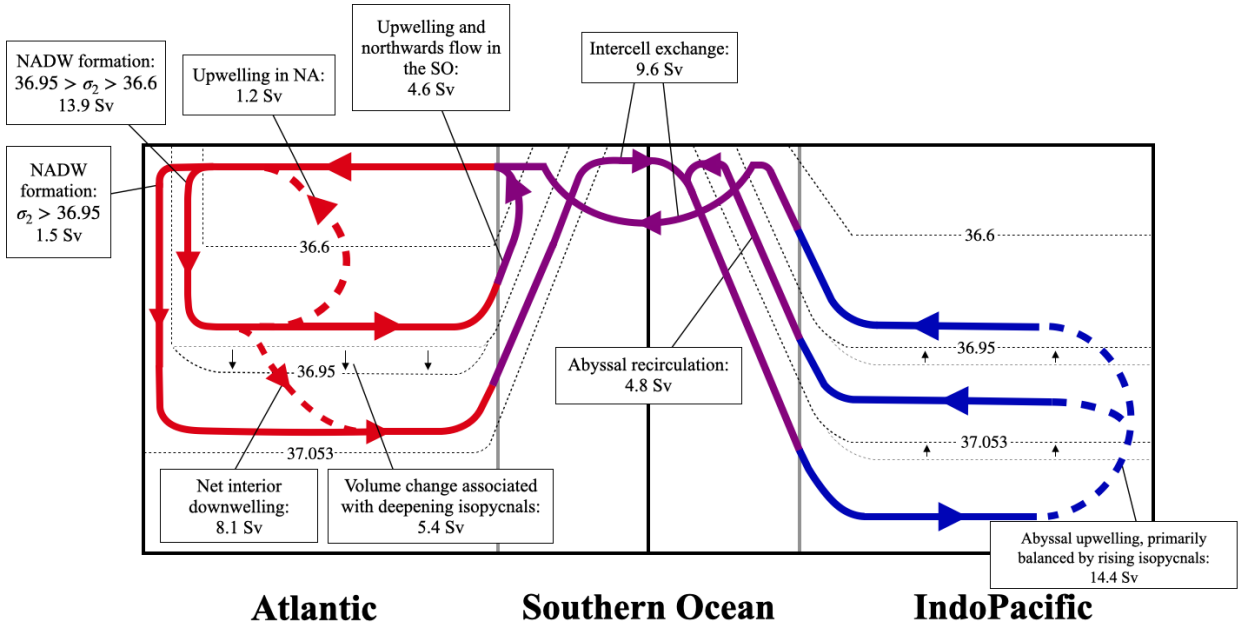

Figure 2.6: Schematic representation of the overturning, inferred from the stream function and volume budget decomposition (Figure 2.3, Figure 2.4). Net transport within the Atlantic Ocean (red arrows), Southern Ocean (purple arrows), and Indo-Pacific Ocean (blue arrows), are shown. Arrows denote direction of flow. Solid and dashed arrows below the surface denote primarily along- and across-isopycnal pathways, respectively. Dashed black lines denote the specific densities discussed in Figure 2.3, and isopycnal depth changes are indicated where they are the dominant contributor balancing up- and down-welling.

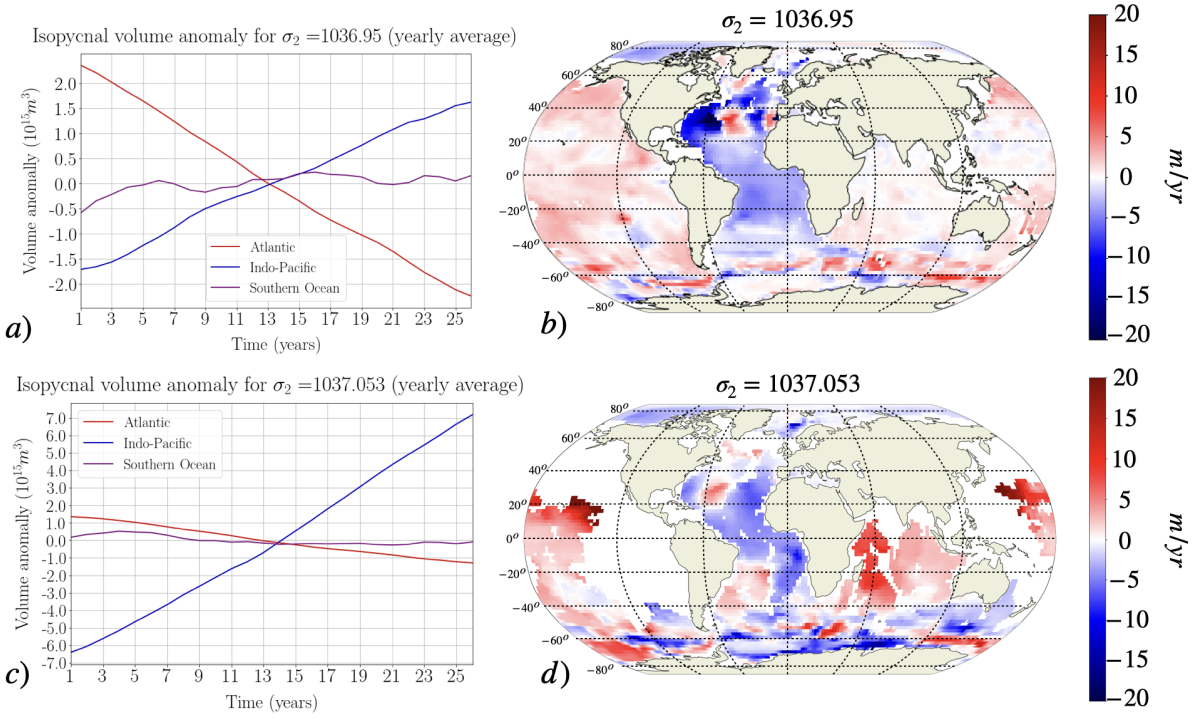

Figure 2.7: Trends in overall isopycnal volumes as calculated from yearly means and subdivided by basin (a, c), and spatial fields of time-averaged vertical isopycnal velocities, in meters per year, b), d) for σ_2=1036.95kg/m^3 (top) and σ_2=1037.053kg/m^3 (bottom) over the ECCO (1992-2017). Striking linear trends are visible in the Atlantic and Indo-Pacific Oceans.

trends in ECCO represent vertical isopycnal displacement velocities on the order of 5-20 m/yr and persist over the entire ECCO period (Figure 2.7ac). These trends are present in all of the major ocean basins and are relatively horizontally homogeneous over the Atlantic and Indo-Pacific basins (Figure 2.7bd).

In the Atlantic, we find deepening mid depth isopycnals and an overall lightening of the deep ocean associated with warming temperatures and decreasing salinity (Figure 2.5ad). A warming deep Atlantic is broadly consistent with previous studies such as Palmer et al. (2015), Desbruyères et al. (2017), and Zanna et al. (2019), although these studies rely on many of the same data sources as ECCO and are accompanied by large uncertainties. It is also possible that an under-representation of dense water inflows across the GIS ridges in ECCO may lead to biases in deep Atlantic density trends by limiting the amount of dense

water entering the Atlantic basin (Rossby et al., 2018; Lumpkin and Speer, 2007; Lee et al., 2019; Tesdal and Haine, 2020). Indeed, preliminary analysis undertaken here suggests that the rate of overflow for the densest waters over the GIS ridge system is too low to replenish the densest NADW in ECCO (see Appendix B, Figure 2.9).

In the Indo-Pacific, meanwhile, we see isopycnal shoaling primarily associated with a cooling of the abyssal ocean (Figure 2.7be) (c.f. Wunsch and Heimbach, 2014; Liang et al., 2015), which is in disagreement with Purkey and Johnson (2010) who suggest broad warming in the Indo-Pacific. This isopycnal shoaling is a leading order term in ECCO's abyssal isopycnal volume budget, where abyssal upwelling is balanced primarily by isopycnal shoaling as opposed to diapycnal mixing, as usually assumed in equilibrium theories such as Munk (1966) or Nikurashin and Vallis (2012). Unfortunately, as argued by Wunsch and Heimbach (2014), it is impossible to be sure whether these trends are the result of long-term trends in ocean climate, intrinsic ocean variability, or modeling and/or sampling biases, given the large uncertainties and sparseness of measurements in the deep ocean. However, it is plausible that isopycnal shoaling in ECCO's deep Indo-Pacific is the result of an under-representation of diapycnal mixing in the abyssal ocean interior (Figure 2.8, de Lavergne et al. (2020a), compare with Trossman et al. (2022)), leading to mixing-driven water mass transformations that are too small to compensate for the in-flow of dense AABW.

Numerical diapycnal diffusion also appears to play a significant role in the volume budget of all basins and is especially prevalent in ECCO's abyssal Indo-Pacific (Figure 2.6b). The presence of numerical diffusion in ECCO is not surprising, as nonphysical numerical diffusion is an inherent property of depth-coordinate circulation models (Griffies et al., 2000), and previous studies have shown that it can be large enough to exceed the rate of explicit mixing (Lee et al., 2002; Urakawa and Hasumi, 2014; Megann, 2017). In addition, the slope clipping invoked in ECCO's isopycnal mixing scheme is likely to have a significant effect on diapycnal mixing in the Southern Ocean. These spurious sources of diapycnal mixing should be taken into consideration in future model development.

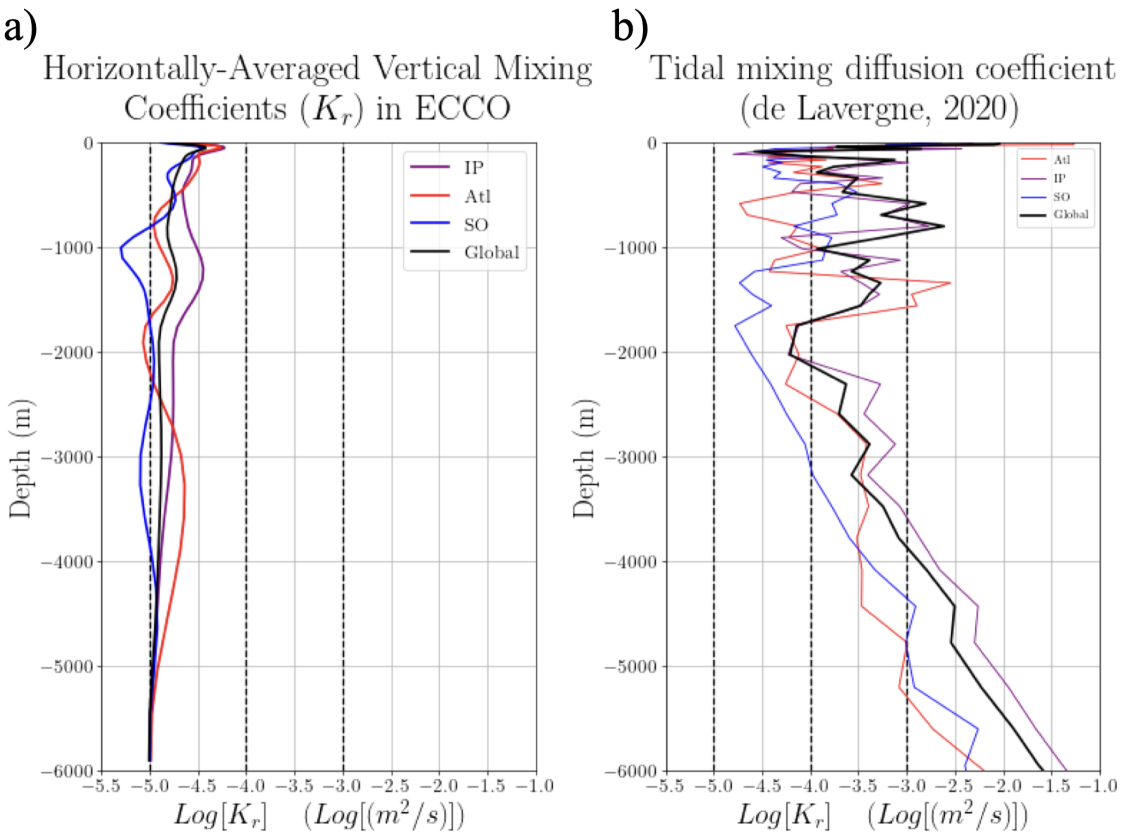

Figure 2.8: a) Vertical diffusivities k_r (m^2/s) in ECCO horizontally averaged over the major ocean basins. Notice that these are the "background" diffusivities optimized by the inversion, and do not include mixing parameterized via the GGL scheme (diagnostics for which are not available). b) Estimated vertical diffusivities from de Lavergne et al. (2020a) averaged over the major ocean basins. These diffusivities are estimated based off of two-dimensional maps of internal tide dissipation. The averages presented in a) and b) are area-weighted horizontal averages, and masked using the same spatial mask as in Figure S1. Colored lines refer to the Indo-Pacific (purple), Atlantic (red), and Southern Ocean (blue). The black lines gives the global average. Vertical dashed lines serve as references to $\log[K_r]$ ranges typical of the deep ocean (de Lavergne et al., 2020a).

The transient evolution of ECCO's deep ocean must be accounted for when interpreting ECCO results and comparing the circulation to theoretical models that are based on an equilibrium assumption. In the equilibrium view, deep water formation in the high latitudes must be balanced by wind-driven upwelling along isopycnals, or irreversible processes in the ocean interior, which in turn are typically assumed to be dominated by diapycnal mixing (e.g. Nikurashin and Vallis, 2012; Marshall and Speer, 2012; Ferrari et al., 2017). Such a balance does not hold in ECCO; instead, the model depicts a global ocean in a transient state with regions of net warming (Atlantic), cooling (Indo-Pacific), and both (the deep Southern Ocean), where much of the apparent diapycnal up- and down-welling is not balanced by water mass transformations. Interestingly, the transient term tends to be small in the North Atlantic and Southern Ocean surface layers wherein dense water formation occurs (See Appendix B), which may explain why previous watermass budget decompositions using ECCO have not identified its importance (e.g. Buckley et al., 2023). If the ECCO solution is correct, prevailing equilibrium theories of the overturning circulation cannot be applied to the present-day ocean. However, there is evidence to suggests that at least some of the trends in ECCO may be unrealistic, which would imply that ECCO's representation of the overturning circulation and water mass transformations are inconsistent. In either case, the presence of isopycnal volume trends is important when interpreting ECCO's climatological mean state, as the assumption of an equilibrium state leads to apparent interior water mass transformations that are actually associated with trends in the water mass volumes.

2.5 Appendices

2.5.1 Appendix A: Estimating water mass transformation due to numerical diffusion

Here we present a method for estimating the contribution of numerical diffusion to the isopycnal volume budget by treating it as the residual between the advective transport inferred

from the volume budget and that inferred from the temperature and salinity tendencies provided by ECCO's advection scheme.

First, we note that the net horizontal transport beneath an isopycnal, $\Delta\Psi$, can be directly related to the advective density tendency on the bounding isopycnal. Consider an isopycnal volume, V, of ocean bounded by meridional walls in the zonal, latitudes y_1 and y_2 in the meridional, and the seafloor and the depth of the σ_2 isopycnal surface in the vertical. For a Boussinesq fluid, conservation of volume implies there is no net advective transport across the volume's boundaries and thus:

$$\Psi(y_2,\sigma_2) - \Psi(y_1,\sigma_2) + \iint_{S(y_1,y_2,\sigma_2,t)} \mathbf{v}\cdot\hat{\eta}\; dS = 0, \tag{2.11}$$

where $S(y_1, y_2, \sigma_2, t)$ is the isopycnal surface bounding the volume at the top, and $\hat{\eta} = \nabla\sigma_2/|\nabla\sigma_2|$ is the unit vector normal to the isopycnal surface. Using that $dS = |\nabla\sigma_2|/|\partial_z\sigma_2|dA$, where dA is the projected horizontal area of the isopycnal surface element dS, we find:

$$\begin{aligned}
\Delta\Psi = \Psi(y_2,\sigma_2) - \Psi(y_1,\sigma_2) &= -\iint_{S(y_1,y_2,\sigma_2,t)} \mathbf{v}\cdot\frac{\nabla\sigma_2}{|\partial_z\sigma_2|}\; dA \\
&= -\iint_{S(y_1,y_2,\sigma_2,t)} \frac{1}{|\partial_z\sigma_2|}\left(\mathbf{v}\cdot\frac{\partial\sigma_2}{\partial\theta}\nabla\theta + \mathbf{v}\cdot\frac{\partial\sigma_2}{\partial S}\nabla S\right)\; dA \\
&= \frac{\partial}{\partial\sigma_2}\iiint_{V(y_1,y_2,\sigma_2,t)} \frac{\partial\sigma_2}{\partial\theta}\mathbf{v}\cdot\nabla\theta + \frac{\partial\sigma_2}{\partial S}\mathbf{v}\cdot\nabla S\; dV.
\end{aligned} \tag{2.12}$$

We now express the temperature and salinity tendencies due to the numerical advection sheme in the model, $\dot{\theta}_{adv}$ and $\dot{S}_{adv}$ (which can be computed from the ECCO output – see Piecuch (2017)), as the sum of the true tendencies and an error that includes the numerical diffusion; i.e. $\dot{\theta}_{adv} = -\mathbf{v}\cdot\nabla\theta + \dot{\theta}_{num}$ and $\dot{S}_{adv} = -\mathbf{v}\cdot\nabla S + \dot{S}_{num}$. Defining the associated water mass conservation rates as

$$T_{adv} = \frac{\partial}{\partial \sigma_2} \iiint_{V(y_1,y_2,\sigma_2,t)} \frac{\partial \sigma_2}{\partial \theta} \dot{\theta}_{adv} + \frac{\partial \sigma_2}{\partial S} \dot{S}_{adv} \; dV. \tag{2.13}$$

and

$$T_{num} = \frac{\partial}{\partial \sigma_2} \iiint_{V(y_1,y_2,\sigma_2,t)} \frac{\partial \sigma_2}{\partial \theta} \dot{\theta}_{num} + \frac{\partial \sigma_2}{\partial S} \dot{S}_{num} \; dV. \tag{2.14}$$

and using (12), we find:

$$T_{num}(y_1, y_2, \sigma_2, t) = \Delta\Psi(y_1, y_2, \sigma_2, t) + T_{adv}(y_1, y_2, \sigma_2, t). \tag{2.15}$$

2.5.2 Appendix B: Surface Layer Water Mass Budgets in ECCO

Here we present a short water mass decomposition of the overturning circulation in the surface layer, defined as the region with between the ocean surface and the isopycnal corresponding to the minimum density outcrop at each latitude. Note that this decomposition follows Abernathey et al. (2016) and does not include a separation between numerical and explicit mixing. Instead, we treat the two as a combined residual of the other terms as in Buckley et al. (2023).

Ultimately, any diapycnal transport in the surface layer must be balanced by buoyancy exchange with the atmosphere and/or sea ice and mixing. We perform a volume budget decomposition within the surface layer, which is analog to the interior volume budget decomposition described in the main text with the addition of surface forcing terms. As in the interior volume budget discussed in the main text, we assume that the volume transport at the base of the surface layer, ψ_{surf} (minus the transport across the Greenland-Iceland-Scotland (GIS) ridge system, Ψ_{GIS}, in the case of the North Atlantic), must be balanced

by heat- and freshwater-driven surface transformations, $T_{surf} = T_\Theta + T_S$, isopycnal volume change within the surface mixed layer, $\frac{d}{dt}V_{surf}$, and horizontal and vertical mixing, T_{mix}:

$$\overline{\Delta\psi(\sigma_2,t)} = \overline{\frac{d}{dt}V_{surf}(\sigma_2,t)} + \overline{T_{surf}(\sigma_2,t)} + \overline{T_{mix}(\sigma_2,t)}, \tag{2.16}$$

where all terms are defined as positive towards higher buoyancy (lower density). Here $\Delta\psi = \psi_{GIS} - \psi_{surf}$ in the North Atlantic and $\Delta\psi = \psi_{surf}$ in the Southern Ocean. We compute $\frac{d}{dt}V_{surf}(\sigma_2,t)$ as in the main text, this time including only volume changes that occur within the surface layer. We compute diapycnal transport associated with heat- and freshwater-driven surface density forcing, T_Θ and T_S, as in Newsom et al. (2016):

$$\begin{aligned} T_\Theta(\sigma_2,t) &= -\frac{\partial}{\partial\sigma_2}\iint_{A_O(\sigma_2,y_1,y_2,t)} \frac{\alpha}{c_p} Q_{surf}(x,y,t)dA \\ T_S(\sigma_2,t) &= -\frac{\partial}{\partial\sigma_2}\iint_{A_O(\sigma_2,y_1,y_2,t)} \frac{\rho_0}{\rho_{fw}}\beta S_0 f_{fw}(x,y,t)dA \end{aligned} \tag{2.17}$$

where the integration area, $A_O(\sigma_2, y_1, y_2, t)$, is the outcropping region where the surface potential density is larger than σ_2 within the particular basin of interest (in this case the Southern Ocean and the North Atlantic), Q_{surf} is the surface heat flux and f_{fw} is the surface freshwater flux. $\alpha = -\frac{1}{\sigma_2}\frac{\partial\sigma_2}{\partial\Theta}$ and $\beta = \frac{1}{\sigma_2}\frac{\partial\sigma_2}{\partial S}$ are the thermal expansion and haline contraction coefficients, respectively, $c_p = 3994$J/kg/K is the heat capacity of seawater, $\rho_0 = 1029.$kg/m^3 is the reference seawater density in ECCO, $\rho_{fw} = 1000.$kg/m^3 is the reference density of freshwater in ECCO, and $S_0 = 35$g/kg is a reference salinity. Here we define the heat- and freshwater-driven transformation rates, $T_\Theta(\sigma_2,t)$ and $T_S(\sigma_2,t)$, as positive for transport towards lower densities. In the North Atlantic, we calculate the rate of deep water inflow across the GIS ridge system, $\Psi_{GIS}(\sigma,t)$, by measuring the rate of meridional transport across the northern boundary of the integration area. We denote the effect of horizontal and vertical diabatic mixing within the surface layer as T_{mix}, and calculate it as the residual of the time-means of the other terms in 2.16.

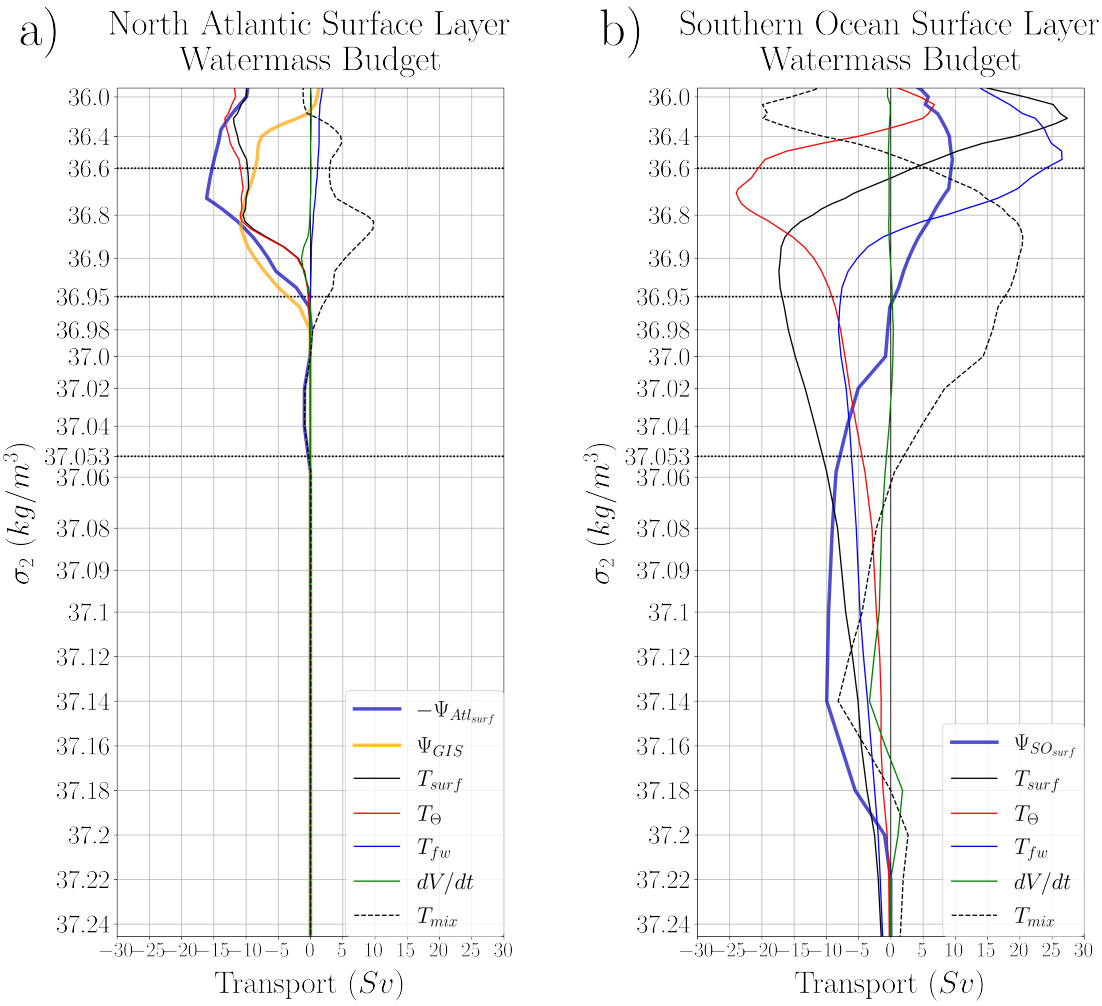

Figure 2.9: Water-mass-transformation decompositions in the surface layers of the North Atlantic a) and Southern Ocean b) high latitudes. All terms are defined positive for transformations towards higher buoyancy (lower density). Shown are the total surface transformation rate, T_{surf}, (thin, solid black) and its heat-driven, T_Θ, (thin, solid red) and freshwater-driven, T_{fw}, (thin, solid blue) components, as well as contributions from isopycnal volume change within the surface layer, dV/dt, (thin, solid green). Dense water inflow across the Greenland-Iceland-Scotland (GIS) ridge system, Ψ_{GIS}, is included in a) (thick, solid orange). Stream function values at the bottom of the surface layer (thick, solid blue) are shown in the North Atlantic, $-\Psi_{Atl_{surf}}$, and the Southern Ocean, $\Psi_{SO_{surf}}$. Note the sign of stream function values in the North Atlantic is flipped such that negative values denote transport towards higher density. Any contributions from surface-layer mixing, numerical mixing, and error in our methodology are calculated as a residual, T_{mix}, (dashed, black).

The numerical implementation of the surface transformation terms follow that used by Abernathey et al. (2016) and is evaluated by discretizing σ_2 into evenly spaced bins at $\Delta\sigma_2 = 0.02\text{kg/m}^{-3}$ spacing. Equations 2.17 are then evaluated numerically as

$$\begin{aligned} T_\Theta(\sigma_2, t) &= \frac{1}{\Delta\sigma_2} \sum_{i=1}^{N_x} \sum_{j=1}^{N_y} A_{c_{ij}} \frac{\alpha}{c_p} \, Q_{surf} \, \delta(\sigma_2 - \sigma_2') \\ T_S(\sigma_2, t) &= \frac{1}{\Delta\sigma_2} \sum_{i=1}^{N_x} \sum_{j=1}^{N_y} A_{c_{ij}} \frac{\rho_0}{\rho_{fw}} \beta S_0 \, f_{fw} \, \delta(\sigma_2 - \sigma_2') \end{aligned} \tag{2.18}$$

where A_c is the horizontal area of each grid cell and N_x and N_y are the zonal and meridional extents of the model domain. The discrete delta function, $\delta(\sigma_2 - \sigma_2')$, is defined as

$$\delta(\sigma_2 - \sigma_2') = \begin{cases} 1 & \text{if } (\sigma_2 - \Delta\sigma_2/2) <= \sigma_2' < (\sigma_2 + \Delta\sigma_2/2) \\ 0 & \text{else} \end{cases} \tag{2.19}$$

Our results are shown in Figure 2.9. We find that, overall, transient volume change plays a small role in the transport balance of the surface layer in both the North Atlantic and the Southern Ocean. Our results in the North Atlantic agrees with an identical water mass transport decomposition of ECCO's North Atlantic by Buckley et al. (2023). However, we note that ECCO fails to generate very dense NADW to balance the dense water export at the southern end of the Atlantic, a result that may contribute to deepening isopycnals in the Atlantic Ocean. This may be due to a lack of dense water overflow over the GIS ridge system (Figure 2.9a), where the highest density of southward water export appears to be much lower than observations suggest (Koltermann et al., 2011).

Our results in the Southern Ocean generally agree with previous watermass decompositions of the Southern Ocean's surface layer in the Southern Ocean State Estimate (SOSE) (i.e. Abernathey et al., 2016) where density loss due to brine rejection plays a large role in the formation of AABW (Figure 2.9b), However, Southern Ocean surface watermass trans-

formations due to heat loss appear to play a slightly larger role in ECCO than in SOSE, although an in depth investigation into the nature of this disagreement is beyond the scope of our study. As in the North Atlantic, transient volume change plays a small role in the overall Southern Ocean watermass budget.

CHAPTER 3

THE EFFECT OF SOUTHERN OCEAN TOPOGRAPHY ON THE GLOBAL MOC AND ABYSSAL WATER MASS DISTRIBUTION

3.1 Introduction

In this chapter we investigate the influence of topographic asymmetries in the Southern Ocean on the global ocean circulation, paying particular attention to the response of the mid depth cell and water mass composition of the abyssal ocean. The Southern Ocean plays a central role within the MOC by facilitating the return of dense Atlantic and Indo-Pacific waters to the ocean surface via wind-driven upwelling along the length of the Antarctic Circumpolar Current (ACC). The Southern Ocean circulation governs the exchange of water masses between the Atlantic and Indo-Pacific ocean basins (Talley, 2013; Jones and Cessi, 2016; Thompson et al., 2016; Ferrari et al., 2017) and has particular importance in setting the strength of the adiabatic circulation of the mid depth cell (Toggweiler and Samuels, 1995a; Vallis, 2000; Wolfe and Cessi, 2011), which in turn plays a critical role in vertical oceanic heat transport and the broader climate (Srokosz et al., 2012). Furthermore, Southern Ocean topographic features have been associated with carbon outgassing and uptake (Balwada et al., 2018) and with poleward heat transport at the surface (Morrison et al., 2023; Prend et al., 2024). However, our theoretical understanding of the structure of its circulation remains largely limited to zonally-integrated theory. For example, the relationship between submarine topography in the Southern Ocean and localized deep water upwelling has only recently been characterized in GCMs (Tamsitt et al., 2017; Youngs and Flierl, 2023) and the role of Southern Ocean topography in the global MOC has only relatively recently become a focus of theoretical research (Nadeau and Ferrari, 2015; Kong and Jansen, 2021; Youngs and Flierl, 2023). Here, we build upon these recent advancements and investigate the

relationship between zonal topographic asymmetries in the Southern Ocean and the water mass composition of the abyssal ocean from an idealized perspective.

In the zonally integrated picture of the two-cell MOC, zonal wind-stress forcing along the length of the Southern Ocean channel drives an equator-ward transport of surface waters that is balanced by deep water upwelling along tilted isopycnals in the Southern Ocean (Toggweiler and Samuels, 1995a; Wolfe and Cessi, 2011; Nikurashin and Vallis, 2012). This wind-driven transport is partially compensated by baroclinic eddies, which act to flatten the isopycnals and transport upwelled deep waters poleward (Marshall and Radko, 2003). The residual circulation that results from these two processes governs the pathway of tracers as they upwell adiabatically along isopycnals to the surface of the Southern Ocean (Walin, 1982; Gnanadesikan, 1999; Nikurashin and Vallis, 2012; Marshall and Speer, 2012). The upwelling deep water, commonly referred to as Circumpolar Deep Water (CDW), consists of both former North Atlantic Deep Water (NADW) as well deep waters from the Indo-Pacific return branch of the abyssal cell (Lumpkin and Speer, 2007; Marshall and Speer, 2012).

Once upwelled CDW reaches the surface of the Southern Ocean it travels either southward towards the bottom water formation regions off the coast of Antarctica, entering the abyssal cell, or northwards to close the upper branch of the mid depth cell (Talley, 2013). Ferrari et al. (2014) suggests that the sign of the yearly-averaged buoyancy flux over the deep water upwelling regions determines the direction of this surface flow, with surface flow directed poleward in regions of net negative surface buoyancy flux and equatorward in regions of net positive buoyancy flux and with the horizontal extent of the two regions largely determined by the quasi-permenant (summer) sea ice extent around Antarctica. In the current climate, a large proportion of mid depth NADW is thus thought to upwell to the south of the positive-negative buoyancy flux transition and flow into the abyssal cell, leading to a configuration dubbed the "figure eight" circulation by Ferrari et al. (2014) whereby the mid depth cell exchanges its densest water masses with the lightest water masses of the abyssal cell in the Southern Ocean (Lumpkin and Speer, 2007; Talley, 2013, Chapter 2). CDW sourced

from the Indo-Pacific abyssal circulation is thought to upwell in regions of both positive and negative buoyancy restoring and is thus split between the bottom water formation regions in the South and the surface waters to the north of the ACC (Talley, 2013; Cessi, 2019, Chapter 2).

Recent studies point towards the importance of topographic zonal asymmetries for water mass pathways in the Southern Ocean, although it remains unclear how these zonal asymmetries affect our theoretical picture of the global MOC. Both outcropping and submarine topographic features are present in the Southern Ocean, which are associated with large-scale standing meanders in the ACC (Thompson and Garabato, 2014), gyres (Nadeau and Ferrari, 2015; Patmore et al., 2019), and AABW export (Stewart and Hogg, 2017). Topographically-induced standing meanders and gyres are thought to carry a significant amount of surface water towards bottom water formation regions (Schröder and Fahrbach, 1999; Reeve et al., 2019) and have been shown to facilitate a large portion of southward oceanic heat transport in idealized, eddy-resolving models (Wilson et al., 2022; Xing et al., 2023).Tamsitt et al. (2017) and Youngs and Flierl (2023) further suggest that deep water upwelling in the Southern Ocean is highly localized near submarine topography, a fact that is obscured in the zonally integrated view and largely ignored in zonally symmetric theory. How these zonal topographic asymmetries affect our idealized theoretical view of the global overturning circulation and water mass properties remains unclear.

A deeper understanding of the role of zonal topographic asymmetries in the Southern Ocean's circulation has implications for our understanding of past climates. The tectonic opening of the Tasmanian Gateway and Drake Passage and the concurrent formation of the ACC are thought to have played a key role in the dramatic global cooling experienced during the early Cenozoic and the glaciation of Antarctica (Kennett, 1977; Zachos et al., 2001), although the role of these topographic changes relative to atmospheric CO_2 drawdown during the Eocene-Oligocene transition is uncertain (Goldner et al., 2014; Anagnostou et al., 2016; Toumoulin et al., 2020). The unblocking of the Southern Ocean and rise of the ACC

have also more directly been linked to the formation and strengthening of the mid depth cell in the Atlantic (Toggweiler and Bjornsson, 2000; Sijp and England, 2004), reduced southward heat transport by polar gyres and subsequent Southern Ocean cooling (Sauermilch et al., 2021), and to Antarctic Bottom Water formation (Kennedy et al., 2015), although the exact mechanisms at play can be difficult to extract from complex coupled climate models. Thus in this study we attempt to isolate the effect of changing Southern Ocean topography on the global ocean circulation by considering the effect of changing Drake Passage ridge heights in a highly simplified setting.

Here we investigate the influence of Southern Ocean topography on the global ocean circulation in an idealized two-basin ocean model, paying particular attention to the effect of Southern Ocean topography on the strengths of the overturning cells and on the water mass composition of the abyssal ocean. For simplicity we limit our study to modifying the height of a meridional ridge in the vicinity of Drake Passage and measuring its effects on the large-scale circulation under various wind stress forcings. We employ passive tracers in a setup similar to that of Jones and Abernathey (2019) (see also Haine and Hall, 2002; Primeau, 2005) to characterize the response of the deep ocean water mass composition to changes in topography and wind stress. Finally, we introduce “exchange" tracers which are not subject to restoring at the surface of the Southern Ocean, allowing us to identify the origin of the upwelled deep waters and surface waters that supply bottom water formation at the surface south of the ACC.

Our results indicate that the addition of a meridional ridge in Drake Passage can significantly alter the structure of the large scale ocean circulation by weakening the mid-depth cell and by spinning up a Southern Ocean gyre. Furthermore, our tracer experiments indicate that such circulation shifts can have a large impact on the water mass composition of the abyssal ocean, leading to decreased direct transfer of NADW between the Atlantic and Indo-Pacific and increased entrainment of surface tracers southwards across the ACC into the AABW formation sites.

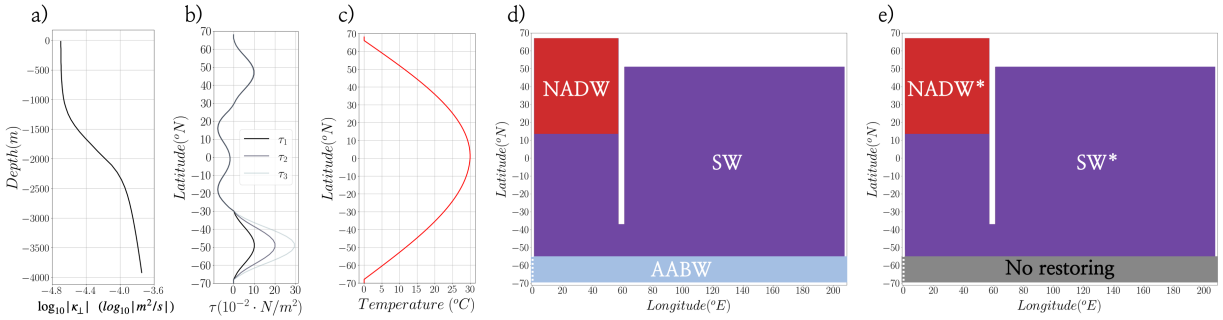

Figure 3.1: Simulation setup. a) Vertical diffusivity profile used for tracer and buoyancy diffusion. b) Meridional, zonally symmetric zonal wind stress profile, including modified wind stress forcings over the Southern Ocean. c) Meridional, zonally symmetric surface temperature restoring profile in ^oC. d) Surface regions corresponding to surface restoring fields for ventilation tracers "NADW", "AABW", and "SW" (reflecting "North Atlantic Deep Water," "Antarctic Bottom Water," and "Surface Water" ventilation tracers, see methods). Ventilation tracers are restored to 1 at the surface in regions labeled here and zero elsewhere. e) Surface regions corresponding to surface restoring fields for exchange tracers "NADW*" and "AABW*" (reflecting "North Atlantic Deep Water"and "Surface Water" exchange tracers, see methods). Exchange tracers are restored to 1 over the labeled regions shown, are not restored over the grey-shaded area in the Southern Ocean, and are restored to zero elsewhere. Dashed white lines near the southern end of the domain show the location of the Southern Ocean ridge.

3.2 Methods

3.2.1 Model setup and experiments

We employ an idealized, ocean-only GCM to simulate the response of an Earth-like MOC to changes in Southern Ocean topography and wind stress forcing. We use the Massachusetts Institute of Technology General Circulation Model (MITgcm) (Marshall et al., 1997a) with a horizontal domain that consists of a spherical sector extending from 70^oS to 70^oN in the meridional and 210^o in the zonal directions, with a horizontal resolution of 2^ox2^o (equivalent to a meridional grid spacing of $\sim$ 200km and a zonal grid spacing that ranges from $\sim$ 80km at the northern and southern ends of the domain to $\sim$ 220km at the equator). Our models are thus not eddy resolving and rely on parameterizations to capture the effects of mesoscale eddies, a tradeoff that is discussed further in the limitations section. The vertical domain

is 4000 m deep and consists of 40 vertical levels of varying thickness, from 37 meters at the surface to 159 meters at the bottom.

We apply a simplified, Earth-like topography consisting of a reentrant channel along the southern end of the domain extending from 68^oS to 56^oS, and two ocean basins to the north: a narrow ocean basin extending to 68^oN, and a wide basin to 50^oN (for brevity we refer to these basins as the "Southern," "Atlantic," and "Indo-Pacific" Oceans, respectively). The basins are separated by a long, 4^o wide continent centered at 0^oE extending from 56^oS to 68^oN representing the Americas and a short 4^o wide continent centered at 60^oE extending from 36^oS to 68^oN representing Africa / Eurasia. This topographic setup is based on studies such as Jones and Abernathey (2019), Baker et al. (2020), and Nadeau and Jansen (2020), all of which successfully recreate an Earth-like two-cell MOC. For simplicity, we limit additional Southern Ocean topography to a 4^o wide meridional ridge of varying heights centered at 0^oE and spanning the latitudinal width of Drake Passage across all runs.

We use a linear, temperature-only equation of state such that buoyancy is given by $b = g\alpha\theta$, where $g = 9.81m/s^2$ is gravitational acceleration, $\alpha = 2 \cdot 10^{-4}K^{-1}$ is the thermal expansion coefficient and θ is potential temperature. Temperature and passive tracers are advected using the Prather (1986) second-order moments advection scheme. The unresolved eddy-induced advection is parameterized via the Gent and Mcwilliams (1990) (GM) scheme and isopycnal and diapycnal mixing is parameterized via a rotated diffusivity tensor, following Redi (1982). The along-isopycnal diffusivity and GM coefficient are spatially constant $1000m^2/s$, while the vertical diffusivity increases with depth to simulate enhanced deep ocean mixing due to turbulent wave breaking (Figure 3.1a). We force the model with zonally uniform wind stress and temperature restoring fields, both broadly based on observations (Figure 3.1bc) and similar to the temperature and wind-stress forcing fields used in Jones and Cessi (2016) and Nadeau and Jansen (2020). The surface temperature restoring time is 30 days across all models.

We configure all models using the setup described above but with varying wind stress

maximums over the Southern Ocean (Figure 3.1b) and ridge heights in Drake Passage (Figure 3.1de). We test three different wind stress cases: a low wind case with Southern Ocean wind stress maximum of $\tau_1 = 0.1N/m^2$, a medium wind stress maximum of $\tau_2 = 0.2N/m^2$, and a high wind stress maximum of $\tau_3 = 0.3N/m^2$. We test our model's response to each of these wind stress cases under 6 different Drake Passage ridge heights (0m, 1000m, 2000m, 2500m, 3000m, 3500m), for a total of 18 model setups. All models are spun up from rest for at least 12,000 years until equilibrium (when temporal variations in both tracer and temperature fields are negligible) has been reached. All simulations have deep/bottom water formation (defined as deep convection reaching depths $> 1km$) in two regions: the North Atlantic north of 64°N and the Southern Ocean south of $66°S$ between $0°E$ and $10°E$.

3.2.2 Passive tracers

In addition to temperature, we employ five passive tracers to track the pathways of water masses through the global circulation. We apply three "ventilation" tracers that track the pathways of water that originates at the surface of the North Atlantic (which broadly captures the production of North Atlantic Deep Water, and is hereafter referred to as "NADW"), in the Southern Ocean in the latitude range of Drake Passage (which broadly captures the production of Antarctic Bottom Water, and is hereafter referred to as "AABW")[1], and over the remainder of the global ocean, including the entire Indo-Pacific and the northern Southern Ocean (for simplicity we refer to this water mass as "surface water," or "SW"). Each ventilation tracer is restored to 1 over different regions of the ocean surface and zero everywhere else (Figure 3.1d). Similar to the setup used in Jones and Abernathey (2019) the restoring fields for NADW, SW, and AABW are non-overlapping and together cover the entire ocean surface. The restoring time for passive tracers at the surface is 5.8 days.

1. Note that the restoring fields for "NADW" and "AABW" presented here encompass much larger horizontal domains than the actual deep water formation sites occupy in our models. Despite this, we have found that the abyssal Indo-Pacific ventilation tracer concentrations for AABW and NADW are generally unchanged if the restoring is applied over more restrictive areas, and choose the above restoring fields for easy comparison with the "exchange" tracers.

We introduce additional “exchange" tracers (hereafter referred to as NADW* and SW*) which allow us to separate AABW into contributions from former NADW versus other lower latitude sources. The restoring fields of NADW* and SW* mirror those of the ventilation NADW and SW tracers but with no restoring applied in the latitudes of Drake Passage (Figure 3.1e). Removing the surface restoring condition in the Southern Ocean allows NADW* and SW* tracers to surface along the upwelling branch of the Southern Ocean MOC and reenter the deep ocean via the deep water formation regions off the coast of Antarctica. The concentration of NADW* in the deep ocean therefore describes both NADW that reaches the deep ocean via internal pathways and any NADW that upwells in the Southern Ocean and renters the deep ocean via deep water formation regions. The restoring time for the exchange tracers at the surface is 5.8 days.

The exchange tracer concentration in the abyssal Indo-Pacific measures the relative importance of the advective pathway of former NADW into the abyssal cell versus diffusive ventilation in the Indo-Pacific. In the perfect “figure 8" limit (Ferrari et al., 2017; Nadeau and Jansen, 2020), where NADW is entirely transformed into AABW around Antarctica (where NADW* is not restored in our models) we would expect the abyssal Indo-Pacific to be mostly NADW* with any abyssal SW* concentration the result of downwards diffusion in the Indo-Pacific, a process that is expected to be less efficient than the advective pathway. If, by contrast, all NADW that enters the Southern Ocean returns northward in the Atlantic, thereby creating two separate overturning cells, the exchange tracer in the abyssal Indo-Pacific would only be ventilated by diffusion and thus be dominated by SW*.

We note that both the ventilation and exchange tracer concentrations should each sum up to 1 throughout the ocean domain. However in practice we find that ventilation tracers experience some degree of loss such that their sum is slightly less than 1 within the abyssal ocean (See Figure 3.5 in Section 4). The exact source of this discrepancy is difficult to verify, and may be the result of incomplete equilibration, surface restoring, and/or numerical inaccuracies.

3.2.3 Circulation response to wind stress and topographic forcing

We characterize the strength of the ACC using the barotropic streamfunction given by:

$$\psi_{bt}(x,y) = \int_{y=y}^{y=68^oN} \int_{-H}^{0} \overline{u}(x,y,z)dzdy, \tag{3.1}$$

where H is the ocean depth, $\overline{u}(x,y,z)$ is the time averaged local eulerian velocity in the zonal direction taken over the last 50 years of our simulations (although we note that due to the non-eddy resolving resolution and time-constant boundary conditions there is no significant temporal variability in our simulations once equilibrated). The addition of a meridional ridge in the vicinity of Drake Passage forces a polar gyre to the east of the Drake Passage, in a geographically similar location to the Weddell Gyre[2]. As in Patmore et al. (2019) we define the strength of the ACC as the net barotropic transport across Drake Passage:

$$\psi_{acc} = \psi_{bt}(0^oE, 68^oS), \tag{3.2}$$

and define the strength of the Southern Ocean gyre as the difference between the maximum barotropic stream function in the latitude band of Drake Passage, $\max\left|\psi_{bt}(x,y)\right|_{y=68^oS}^{y=54^oS}$, and the ACC transport:

$$\psi_{gyre} = \max\left|\psi_{bt}(x,y)\right|_{y=68^oS}^{y=54^oS} - \psi_{acc}. \tag{3.3}$$

We quantify the response of the global overturning circulation to changes in Southern Ocean topography and wind forcing using the isopycnal MOC, $\psi(y,b)$, which gives a useful representation of the material transport pathways of the deep ocean (Nurser and Lee, 2004;

2. We note that while the polar gyre generated in our simulations shares features with the real Weddell and Ross Gyres, it represents a significant simplification of the gyre dynamics in the real southern Ocean. In particular, the Weddell gyre is associated with an outcropping ridge to the east and both the Weddell and Ross gyres are associated with a submarine zonal barrier to the north. Exploring the effects of these additional topographic features on the circulation is left for future study.

Ferrari and Ferreira, 2011):

$$\psi(y,b') = \int_{x_0}^{x_1}\int_{-H}^{0}(\overline{v}(x,y,z)+\overline{v}^*(x,y,z))\mathcal{H}(b'-\overline{b}(x,y,z,t))dxdz, \tag{3.4}$$

where y denotes latitude, x_0 and x_1 give the zonal extent of the ocean basin, H is the ocean depth, $\overline{v}(x,y,z,t)$ and $\overline{v}^*(x,y,z)$ are the time averaged local meridional velocity and eddy transport velocity due to the GM scheme, respectively, $\mathcal{H}$ is the heavyside step function, b' is any given buoyancy level, and $\overline{b}(x,y,z)$ is the time averaged local buoyancy taken over the last 50 years of our simulations. We define the strength of the mid depth cell as the the maximum strength of $\psi(y,b')$ between $b = 0.002m/s^2$ and $b = 0.019m/s^2$ integrated over the southern end of the Atlantic basin (36^oS):

$$\psi_{atl} = \max\left|\int_{2^oE}^{58^oE}\int_{-H}^{0}(\overline{v}(x,36^oS,z)+\overline{v}^*(x,36^oS,z))\mathcal{H}(b'-\overline{b}(x,36^oS,z))dxdz\right|_{b=0.002m/s^2}^{b=0.019m/s^2}. \tag{3.5}$$

Note that we choose this definition rather than using the maximum mid-depth cell strength in the North Atlantic because it is most relevant to the transport of NADW into the abyssal Indo-Pacific, discussed in Section 4. Either metric can be used to characterize the magnitude of the mid-depth cell strength and we note that the two metrics are highly correlated ($R^2 = 0.99$). We define the strength of the abyssal cell, ψ_{ip}, using the minimum value of the streamfunction in the Indo-Pacific (north of 36^oS) between the buoyancy levels of $b = 0.0004m/s^2$ and $b = 0.005m/s^2$:

$$\psi_{ip} = \min\left|\min\left|\int_{62^oE}^{208^oE}\int_{-H}^{0}(\overline{v}(x,y,z)+\overline{v}^*(x,y,z))\mathcal{H}(b'-\overline{b}(x,y,z))dxdz\right|_{y=36^oS}^{y=50^oN}\right|_{b=0.0004m/s^2}^{b=0.005m/s^2}. \tag{3.6}$$

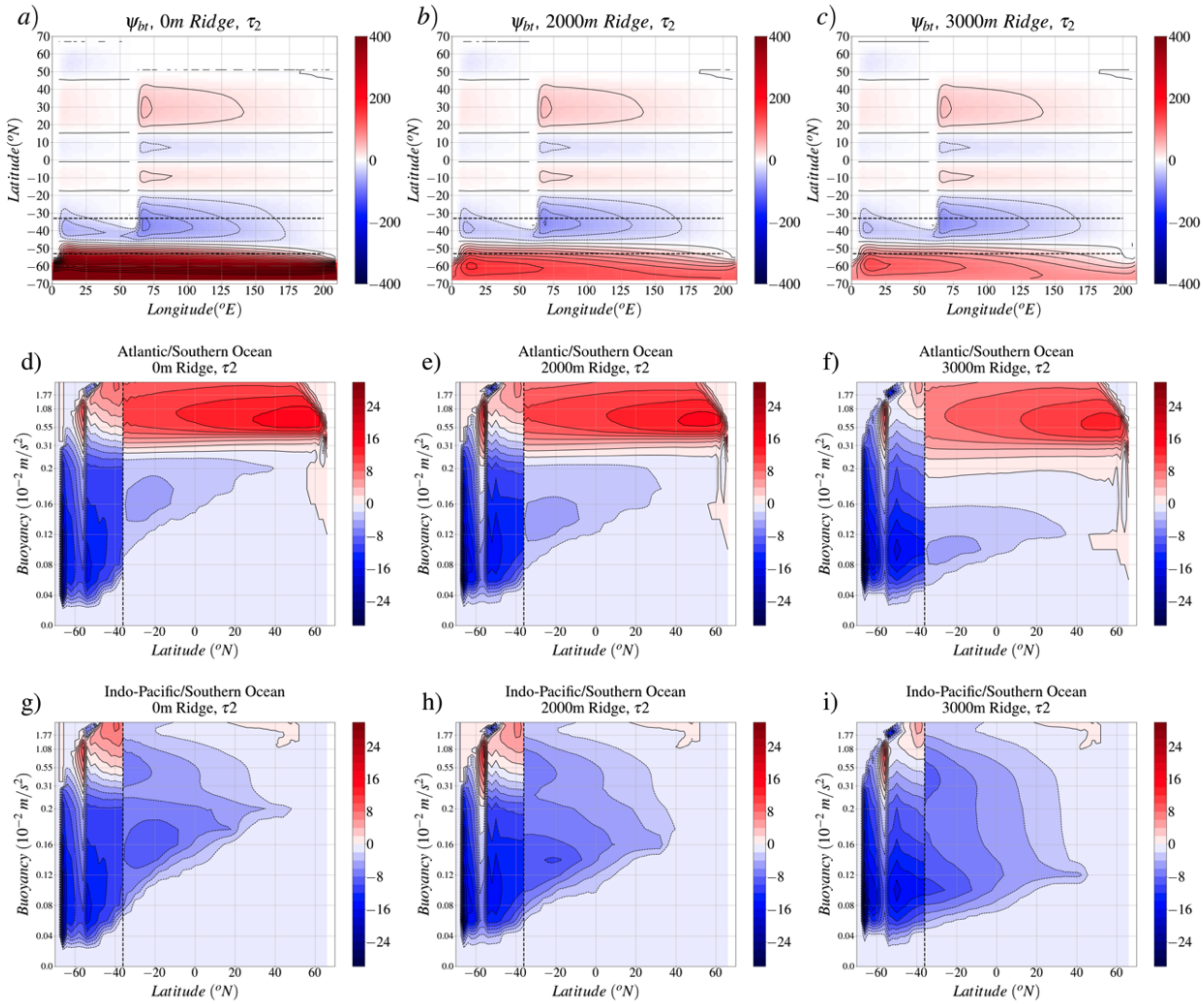

Figure 3.2: Ocean circulation states for various topographic configurations in our models for (from left to right) the no ridge case, 2000 meter ridge case, and 3000 meter ridge cases, under $0.2N/m^2$ Southern Ocean maximum wind stress. a-c) barotropic stream functions. d-f) isopycnal overturning stream functions for the Atlantic (north of 36^oS) and Southern Ocean (south of 36^oS). Here the y-axis is stretched to the average z-space height of the corresponding isotherms in the Atlantic Ocean. g-j) as in d-f) but showing the Indo-Pacific overturning streamfunction north of 36^oS. Contour intervals are 10Sv for the barotropic stream functions (a-c) and 2Sv for the isopycnal meridional stream functions (d-j).

3.3 Results: ocean circulation

3.3.1 Barotropic circulation

The Southern Ocean's barotropic circulation is highly sensitive to both wind stress and ridge height (Figure 3.2a-c, Figure 3.3ab). The flat bottom cases exhibit a strong ACC, ranging

from 228Sv for $0.1N/m^2$ wind stress to 665Sv for 0.3 N/m^2 wind stress. As found in previous work (e.g. Nadeau and Ferrari, 2015), the strength of the ACC shows a rapid weakening once even a modest (1000m) ridge is introduced, dropping to 93Sv for $0.1N/m^2$ wind stress and 193Sv for $0.3N/m^2$ wind stress. ACC strength falls off further as ridge height increases beyond 1000m, reaching as little as 31Sv for the 3500m ridge case (Figure 3.3a). Although ACC strength generally increases under larger wind stresses, this relationship weakens as ridge height increases and becomes mostly flat for the 3500m ridge height case (c.f. Kong and Jansen, 2021; Shakespeare and Hogg, 2012). Here it is worth noting that our model's coarse resolution does not explicitly resolve transient eddies and necessitates the use of a constant background GM diffusivity, which has been shown previously to lead to an overrepresentation of ACC sensitivity to wind stress (Mak et al., 2018; Kong and Jansen, 2021), although the presence of topography has been found to significantly reduce the sensitivity of the ACC transport to mesoscale eddy representation (and hence resolution) as standing meanders modulate the effective eddy diffusivity (Kong and Jansen, 2021; Stewart et al., 2023). The results of Kong and Jansen (2021) suggest that the response of the ACC transport to wind stress changes may be overestimated by almost an order of magnitude compared to eddy resolving simulations in the limit of a flat bottom. In the presence of significant topography the difference between eddy resolving and coarse resolution simulations was found to be substantially reduced (but still present), with the sensitivity to wind stress changes enhanced by up to a factor of two in coarse resolution simulations.

A Southern Ocean ridge is required for Southern Ocean gyre formation in our models. No gyre forms in the flat bottom Southern Ocean cases, while a gyre extending from the coast of Antarctica to the southern edge of the ACC forms in the lee of Drake Passage following the introduction of a 1000m ridge (Figure 3.2a-c). Consistent with results from previous studies (Nadeau and Ferrari, 2015; Patmore et al., 2019), the Southern Ocean gyre strengthens in response to both increasing ridge height and wind stress (Figure 3.3b). The Southern Ocean gyre shows a strong dependance on both wind stress and ridge height, ranging in strength

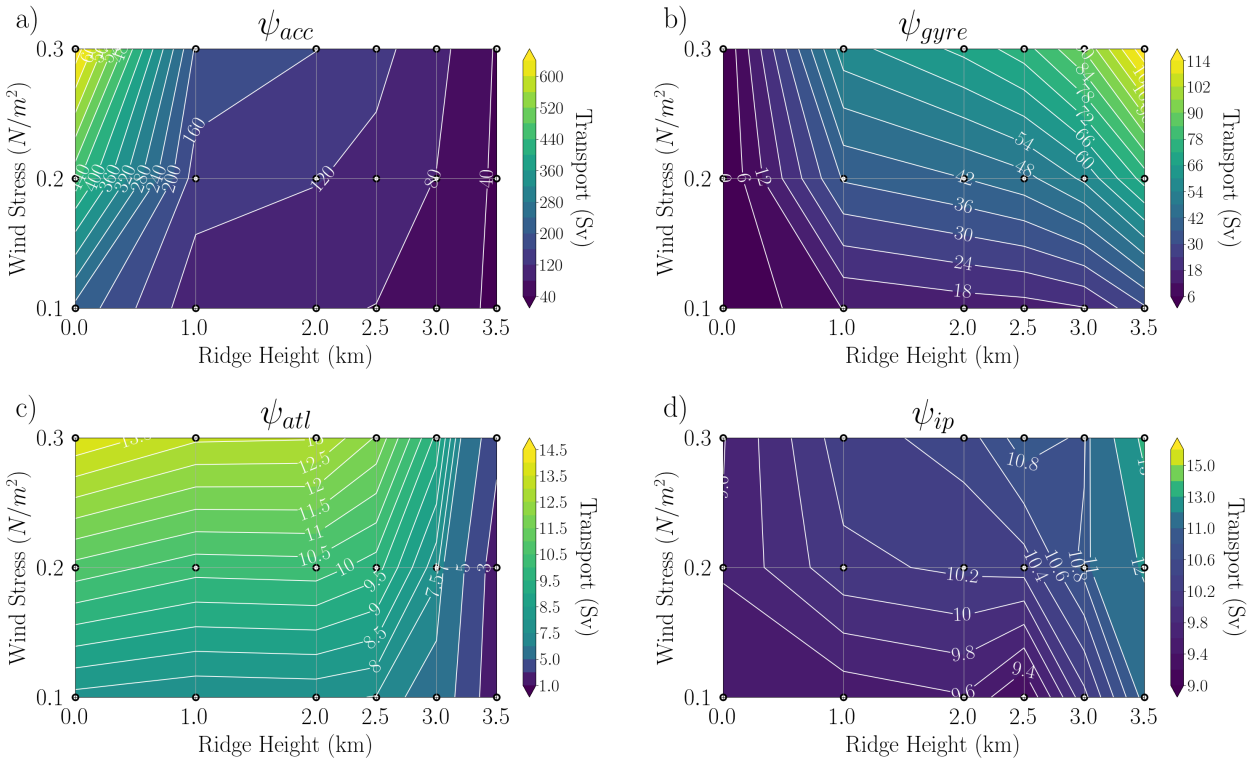

Figure 3.3: Bivariate plots of MOC response to various wind-stress and ridge height configurations as functions of ridge height (in x) and wind stress (in y). a) Maximum barotropic ACC transport at Drake Passage. b) Southern Ocean gyre transport. c) Maximum mid-depth cell strength at 36^oS. d) Maximum abyssal cell strength north of 36^oS. Circular markers denote the wind stress / ridge height combinations used in this study.

from 12Sv in the 1000m, $0.1N/m^2$ case to 119Sv in the 3500m, $0.3N/m^2$ case, a range that encompasses values similar to observational (Dotto et al., 2018; Reeve et al., 2019) and model-derived (Mazloff et al., 2010; Wang, 2013) estimates of the strengths of the Ross and Weddell polar gyres.

The close relationship between the strength of the ACC / the Southern Ocean gyre and Southern Ocean submarine topography is well documented in the literature and is a consequence of the topographic form stress (Munk and Palmén, 1951; Olbers, 1998; Nadeau and Ferrari, 2015; Patmore et al., 2019). As ridge height increases, the ACC slows and a Southern Ocean gyre forms in the lee of the meridional ridge (Abernathey and Cessi, 2014), as topographic-form drag replaces bottom friction as the momentum sink balancing surface wind stress (Thompson and Garabato, 2014; Patmore et al., 2019).

3.3.2 MOC

Our simulations successfully recreate the two-cell MOC structure observed in the real ocean (e.g. Lumpkin and Speer, 2007; Cessi, 2019), with a mid-depth cell largely confined to the narrow, active basin (c.f. Jones and Cessi, 2016) and an AABW-fed abyssal cell that dominates the Indo-Pacific sector. The isopycnal MOC under medium wind forcing ($\tau_2 = 0.2N/m^2$) for the 0m, 2000m, and 3000m ridge cases is shown in Figure 3.2d-i. Overall, the response of the overturning circulation to changes in topography and wind-stress is similar to that found by previous targeted studies of the overturning in the Southern Ocean (Toggweiler and Samuels, 1995b; Abernathey et al., 2011; Kong and Jansen, 2021; de Boer et al., 2022), and in single-basin models such as Chang and Jansen (2021).

The strength of the mid-depth cell at the northern end of the Southern Ocean, ψ_{atl}, is largely insensitive to ridge heights (Figure 3.3c) between 0m to 2000m and is instead primarily a function of the maximum wind stress over the Southern Ocean, ranging from 7.7Sv in the 2000m ridge case under low wind stress to around 13.8Sv for high wind stress in the flat-bottom case. Mid-depth cell strength falls off as ridge heights pass 2500m, reaching a minimum of 1.6Sv for the 3500m ridge case under low wind stress. An eventual fall off of the mid-depth cell strength may be expected as the topography approaches the limit of a closed Drake Passage where no or only a substantially weakened cross-equatorial mid-depth cell is expected (Bryan, 1986; Toggweiler and Samuels, 1995a). In our models, the onset of a substantial decline at a ridge height of 2500m is associated with the intrusion of the ridge into the depth range of the mid-depth cell in the Southern Ocean, when mid depth cell isopycnals begin to intersect with the ridge at the northern end of Drake Passage (not shown). The relative insensitivity of the mid-depth cell to intermediate-depth topography is similar to that observed in another targeted idealized study of the MOC, Abernathey et al. (2011), although that study involved a more complex Southern Ocean topography and a sponge layer north of the Southern Ocean.

The strength of the abyssal cell, ψ_{ip}, varies between about 9.4 and 10.9Sv across our

simulations with ridge heights $\leq 3000m$, increasing only weakly with increasing topographic height and wind stress (Figure 3.3d). The abyssal cell increases to 13.3Sv for the 3500m ridge case under high wind stress (c.f. Xing et al., 2023). The muted abyssal cell response over medium and low ridge heights is consistent with similar studies such as Bishop et al. (2016) and Chang and Jansen (2021), who find that the abyssal cell in the northern basins is largely dependent on the buoyancy boundary conditions over the Southern Ocean and the vertical diapycnal diffusivity in the abyss, both of which are held constant in our study. Here we note that our metric for abyssal cell strength does not capture the response of the Southern Ocean channel's maximum abyssal circulation or the net northward AABW export, both of which have been shown to be more sensitive to Southern Ocean topography (Chang and Jansen, 2021; Schmidgall et al., 2023).

3.4 Results: water mass tracers

3.4.1 Tracer concentrations

Zonally-averaged time-mean tracer concentration fields in the Indo-Pacific and Southern Ocean for the middle (τ_2) wind stress case and for three different ridge heights ($0m, 2000m, 3000m$) are shown in Figure 3.4. NADW tracer enters the deep Southern Ocean at depth, visible here as the maximum NADW concentration between 1000m-1500m in the northern Southern Ocean (Figure 3.4a-c), and either travels into the mid-depth Indo-Pacific via zonal exchange (Nadeau and Jansen, 2020) or upwells directly to the surface of the Southern Ocean, with isopycnal mixing contributing to a decline in NADW concentration as it approaches the Southern Ocean surface. The concentration of NADW ventilation tracer that reaches the abyssal Indo-Pacific ranges from 4-17% (Figure 3.5), indicating that relatively little NADW is able to enter the Indo-Pacific directly at depth. The concentration of NADW ventilation tracer in the abyssal Pacific generally trends downwards with decreasing wind stress and higher bottom topography (Figure 3.5).

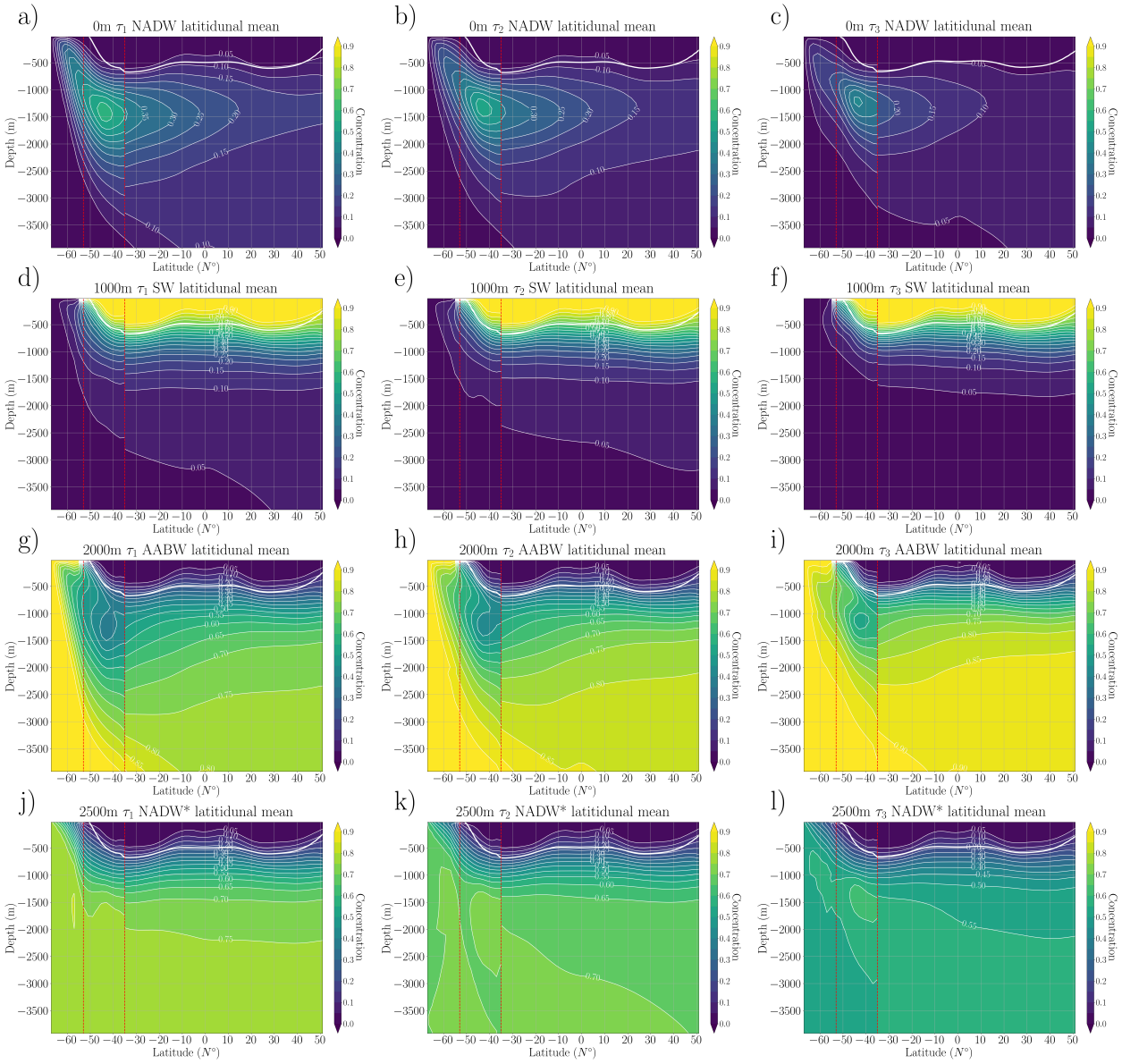

Figure 3.4: Zonally averaged tracer concentrations over the Southern Ocean (south of 36^oS) and Indo-Pacific (north of 36^oS) for NADW (a-c), SW (d-f), AABW (g-i), and NADW* (j-l) for 0m, (left), 2000m (center) and 3000m (right) topograpgy and with $\tau = 0.2N/m^2$ wind stress. Vertical dashed lines at 54^oS and 35^oS give the northern latitudinal extent of "Drake Passage" (i.e., the southern tip of the long continent) and the latitude of "Cape Horn" (i.e., the southern tip of the short continent), respectively. The solid white line indicates the isopycnal corresponding to the minimum buoyancy outcrop in the Southern Ocean, $b_{SO_{min}}$.

AABW makes up the primary component of the abyssal Indo-Pacific in all cases, with average abyssal concentrations ranging from 68% (in the 0m ridge, τ_3 wind-stress forcing case) to 93% (in the 3500m ridge, τ_1 wind-stress forcing case). AABW concentrations in the

abyssal (below 2000m) Indo-Pacific are fairly uniform (Figure 3.4g-i), and generally increase with ridge height and decrease with wind stress (Figure 3.5). Finally, SW tracer is generally limited primarily to the thermocline of the Indo-Pacific and northern Southern Ocean and falls off quickly with depth (Figure 3.4d-f), with mean abyssal SW concentrations in the abyssal Indo-Pacific ranging from 10% for 0m ridge, high wind stress case, to $< 1\%$ for a 3500m ridge, low wind stress case.

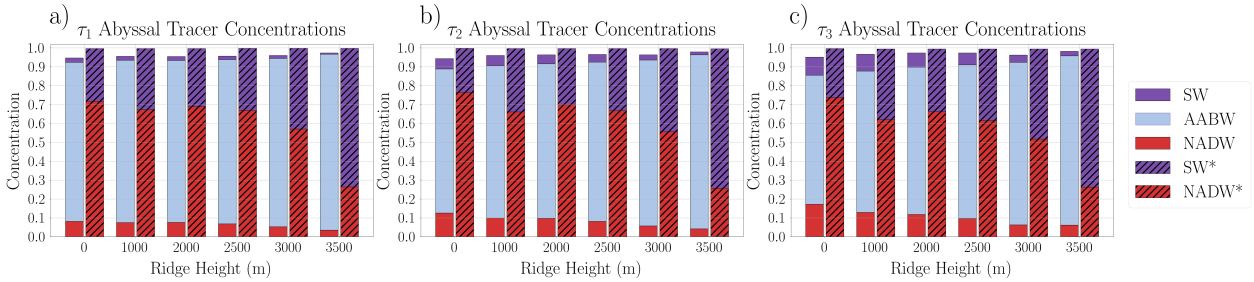

Figure 3.5: Horizontally-averaged time-mean ventilation and exchange tracer concentrations in the abyssal Indo-Pacific below 2000m. Horizontal mean ventilation tracer concentrations are given by SW (Surface Water, solid purple), AABW (Antarctic Bottom Water, solid light blue), and NADW (North Atlantic Deep Water, solid red). Horizontal mean exchange tracers are shown using hatched bars and are plotted adjacent to the ventilation tracer concentrations for each run. Exchange tracers are given by SW* (exchange Surface Water, purple with black hatches) and NADW* (exchange North Atlantic Deep Water, red with black hatches). Notice that NADW* includes NADW as well as the part of AABW that is sourced from former NADW* (and similarly for SW*).

NADW ventilation of the abyssal Indo-Pacific is highly correlated with the strength of the mid-depth cell at the southern end of the Atlantic (Figure 3.6a), which measures the volume of NADW that makes it into the Southern Ocean. SW concentration in the abyssal Indo-Pacific falls off with increasing ridge height and decreasing wind stress and is highly correlated with ψ_{surf} (Figure 3.6b), the net rate of subduction by the upper branch of the mid-depth cell in the Southern Ocean. We diagnose ψ_{surf} as the maximum stream function at the bottom of the surface layer in the Southern Ocean north of Drake Passage:

$$\psi_{surf} = \max |\psi(y, b_{SO_{min}})|_{y=54^o S}^{y=32^o S}, \tag{3.7}$$

where $b_{SO_{min}}$ is the bottom of the surface layer defined as the minimum buoyancy in the top grid level at each latitude in the Southern Ocean (Figure 3.4).

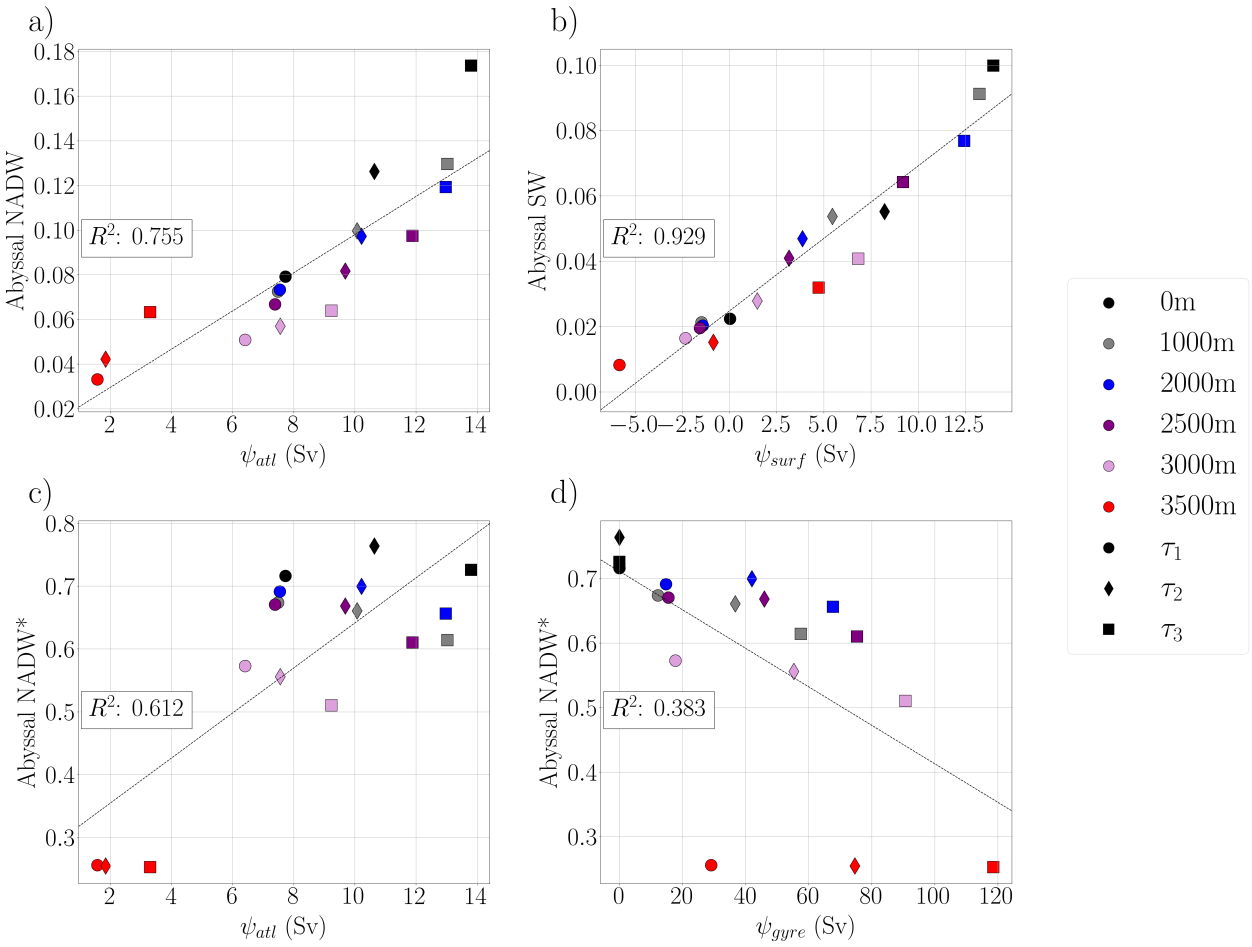

Figure 3.6: a) Mean abyssal NADW concentrations vs mid-depth cell strength. b) Mean abyssal SW concentrations vs intermediate water formation (ψ_{surf}). c) Mean NADW* concentration vs mid-depth cell strength. d) Mean NADW* concentration vs gyre strength. The ridge height and wind stress used in each run is given by marker color and shape, respectively (see legend).

The exchange tracer composition of the abyssal Indo-Pacific is broadly made up of similar parts SW* and NADW*, with weak spatial variations below the lower thermocline (∼1000m) (Figure 3.4j-l). NADW* dominates the abyssal Indo-Pacific composition for the 0-2000m ridge cases (Figure 3.5). As ridge height increases past 2000m NADW* is gradually replaced by SW* in the abyssal Indo-Pacific until by 3500m NADW* makes up only about 25% of the abyssal Indo-Pacific tracer composition. The concentration of NADW* in the

abyssal Indo-Pacific can be thought of as the sum of ventilation NADW that enters the abyssal Indo-Pacific directly at depth and the NADW*-derived AABW that is formed in the Southern Ocean. The proportion of AABW-derived NADW* in the abyssal Indo-Pacific (i.e. (NADW*-NADW)/NADW*) is high, ranging from approximately 91% for the 3000m ridge, low wind stress case to approximately 76% for the 0m ridge and 3500m ridge height cases under high wind stress, indicating that most NADW upwells in the Southern Ocean before making its way into the abyssal Indo-Pacific.

The fall off in NADW* concentrations in the abyssal Indo-Pacific with increasing ridge height exhibits some correlation with mid-depth cell strength, although the fit is weaker than for ventilation NADW and the wind-stress-dependence is not captures (Figure 3.6c). In fact, much of the correlation between NADW* in the abyssal Indo-Pacific and ψ_{atl} can be explained by the strong concurrent fall off in both quantities in the 3500m ridge cases, suggesting that mid-depth cell strength alone is a poor predictor for exchange tracer concentration for low to intermediate ridge heights. Abyssal Indo-Pacific NADW* also exhibits a weak negative correlation with the strength of the Southern Ocean gyre (Figure 3.6d). As will be discussed in the following subsection, the variations in NADW* in the abyssal Indo-Pacific can be well described by the combined effect of the mid-depth cell and gyre strengths.

3.4.2 A simple model describing exchange tracer transport

The response of abyssal NADW* to increasing ridge height and wind stress cannot be explained by any one transport process (Figure 3.6cd). With that in mind, we build a simple model based on conservation of tracer and mass that captures the variations in NADW*. The model considers a single volume comprised of the deep Indo-Pacific and Southern Ocean below the isopycnal $b_{SO_{min}}$ that outcrops at the northern end of the Southern Ocean channel region (Figure 3.4), such that there is no surface restoring of NADW* (or SW*) within the volume. The concentration of NADW* (and thus SW*=1-NADW*) in this volume is

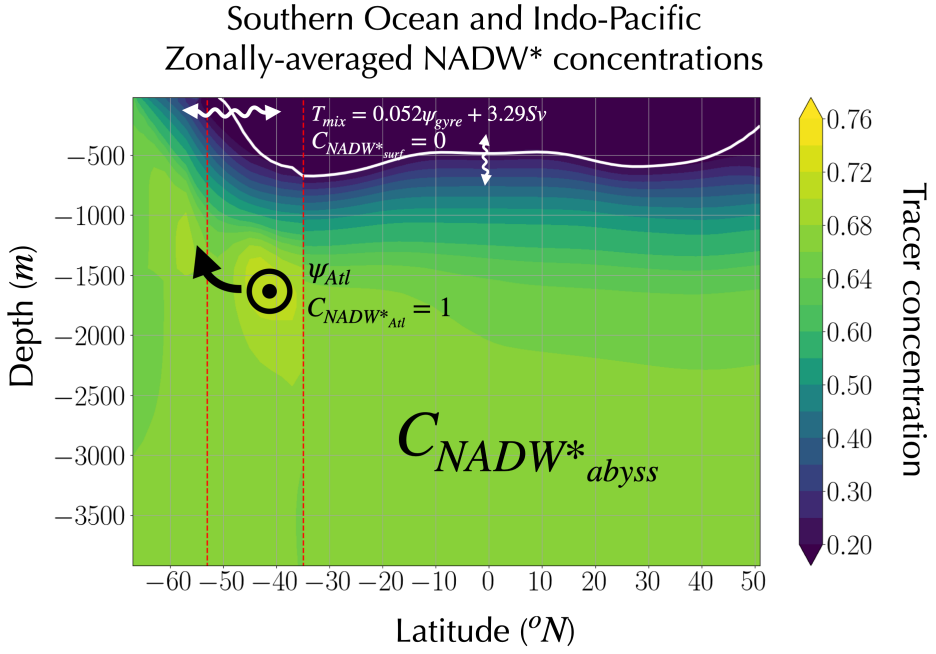

Figure 3.7: Schematic illustrating our box model for the deep Indo-Pacific NADW* concentration, overlaid on the zonally-averaged C_{NADW^*} for the 2000m, $\tau_2 = 0.2N/m^2$ case. The white contour line in the upper ocean denotes the buoyancy level corresponding to the minimum buoyancy outcrop in the Southern Ocean, above which C_{NADW^*} is close to zero. White wavy arrows denote diapycnal exchange transport between the surface layer and the deep ocean, and, combined, capture both vertical mixing in the ocean basin and horizontal mixing at the surface of the Southern Ocean. Net transport of NADW into the Southern Ocean and Indo-Pacific, ψ_{atl}, is shown by $\odot$ and corresponds to a maximum in zonally-averaged C_{NADW^*} in the Southern Ocean. Note that the C_{NADW^*} concentration in the abyssal ocean is fairly uniform throughout the deep Southern Ocean and Indo-Pacific. Thin red dashed lines give the northern latitude of Drake Passage and the southern tip of Africa at 56^oS and 36^oS, respectively.

thus governed by two processes: 1) mixing across the upper bounding isopycnal (both in the interior and at the surface of the Southern Ocean), which we characterize via an exchange transport T_{mix}, and 2) an advective source of NADW from the Atlantic with a rate ψ_{atl} (Figure 3.7). With T_{mix} and ψ_{atl} as the only two source terms that determine the ratio of NADW* and SW* in the abyssal ocean, we can construct a budget for the concentration of NADW* (c.f. Gebbie and Huybers, 2010) in the deep ocean as:

$$C_{NADW^*_{abyss}} = \frac{\psi_{atl} C_{NADW^*_{atl}} + T_{mix} C_{NADW^*_{surf}}}{\psi_{atl} + T_{mix}}, \tag{3.8}$$

where ψ_{atl} is the strength of the mid-depth cell transport into the Southern Ocean as defined previously (3.5), $C_{NADW^*_{atl}}$ and $C_{NADW^*_{surf}}$ are the time-mean concentrations of exchange NADW tracer in the incoming NADW and in the volume above $b_{SO_{min}}$, respectively, and $C_{NADW*_{abyss}}$ is the time-mean concentration of $NADW*$ in the abyssal Indo-Pacific (here taken below 2000m). Rearranging (3.8) and assuming the concentrations $C_{NADW^*_{surf}}$ and $C_{NADW^*_{atl}}$ are 0 and 1. respectively, we can derive a simple expression to infer the strength of T_{mix} from known quantities:

$$T_{mix} = \frac{\psi_{atl}(1 - C_{NADW^*_{abyss}})}{C_{NADW^*_{abyss}}}. \tag{3.9}$$

We find that T_{mix} is closely correlated with the strength of the Southern Ocean gyre (Figure 3.8a). As gyre strength increases the rate of the net diapycnal mixing transport increases as well, ranging from 3.1Sv in the 0m ridge cases where no gyre is present to 9.7Sv for the high wind stress, 3500m ridge case. A simple least-squares fit yields a linear scaling between T_{mix} and ψ_{gyre} of $T_{mix} = 0.052 \cdot \psi_{gyre} + 3.29Sv$, which matches the results with an R^2 value of 0.79. We note that T_{mix} necessarily includes contributions from both horizontal surface mixing across the ACC, which we expect to increase with the gyre strength, and interior diapycnal mixing, which is not expected to change much across our simulations and likely explains the constant offset in the least square fit. The relatively small interior diapycnal mixing-driven transport is consistent with our ventilation tracer results (Figure 4), which show very small SW ventilation tracer concentrations in the abyssal Pacific and with the majority of SW* consisting of former AABW.

Applying the scaling for T_{mix} with gyre strengths to (3.8) gives us a predictive model for the NADW* concentration in the abyssal Indo-Pacific ocean as a function of the mid-depth cell and gyre strength:

$$C_{NADW^*_{abyss}} = \frac{\psi_{atl}}{\psi_{atl} + 0.052 \cdot \psi_{gyre} + 3.29Sv}, \tag{3.10}$$

where the coefficients are determined from the linear scaling derived from (3.9). We find that (3.10) works well across all ridge cases and wind stress values, explaining about 95% of the variance in $C_{NADW*^*_{abyss}}$ (Figure 3.8b).

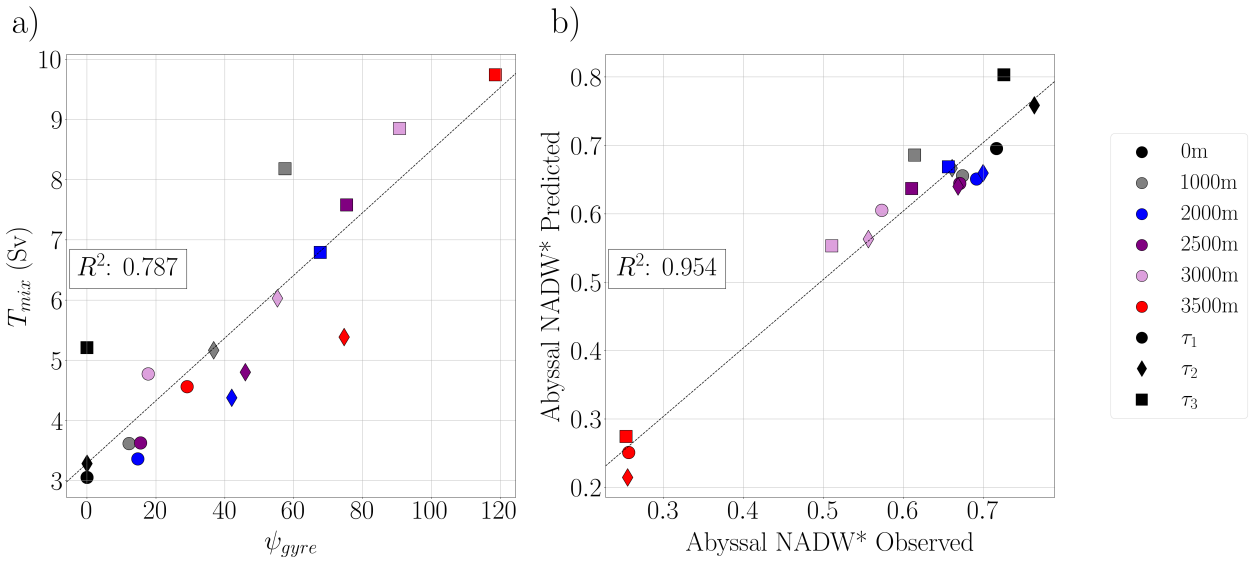

Figure 3.8: a) T_{mix} estimated from Eq. (3.9) vs the strength of the Southern Ocean gyre. b) Predicted deep ocean NADW* concentrations derived from Eq. (3.10) vs the deep ocean NADW* concentrations observed in our numerical models. As in Figure 3.6, the ridge height and wind stress used in each run is given by marker color and shape, respectively (see legend).

In summary, NADW* concentrations in the Indo-Pacific decrease with a higher Drake Passage ridge and decreasing wind stress, a relationship that is primarily associated with the weakening mid-depth cell and the strengthening of the Southern Ocean gyre. The net transport of basin waters into the abyssal ocean that must balance NADW* injection by the mid-depth cell, T_{mix}, is highly correlated with the strength of the gyre south of the ACC. T_{mix}'s strong dependance on the gyre circulation combined with the low concentration of ventilation SW in the abyssal ocean suggests that horizontal transport at the surface of the Southern Ocean plays a large role in setting the overall NADW* concentration, likely by exchanging NADW with surface waters north of the ACC.

3.5 Discussion

3.5.1 Limitations

The idealized configuration used in this study has allowed us to explore the mechanistic role of topographic barriers and wind stress in the Southern Ocean in affecting deep ocean water mass pathways. However, although this approach allows for relatively clean sensitivity experiments, care must be taken when interpreting our results in the context of the real ocean. In addition to the idealized topography, our model lacks salinity, which can modulate the circulation response via salt-advection feedbacks (e.g. Wolfe and Cessi, 2014; Buckley and Marshall, 2016; Ferreira et al., 2018), sea ice, which is likely to play a key role in AABW formation processes (e.g. Ohshima et al., 2013; Jansen, 2017), and coupled interactions with the atmosphere, which would further modulate the ocean boundary conditions. Our quantitative results are also specific to our model setup, as both basin width (Jones and Cessi, 2017; Nadeau and Jansen, 2020) and the configuration of the narrow ("Atlantic") basin (Ragen et al., 2022) can affect the rate of NADW and NADW* transport into the Southern Ocean via their influence on the strength and depth of the mid depth cell. The role of variations in the continental configuration, sea ice, and coupling to the atmosphere should be explored in future studies.

Our model's coarse resolution moreover requires mesoscale eddy effects to be parameterized, which is a major, but unfortunately unavoidable, limitation. Mesoscale eddies play an important role for the transport of tracers and buoyancy in the Southern Ocean (Sauermilch et al., 2021; Xing et al., 2023) and tend to be enhanced near topography (Wilson et al., 2022). Idealized studies of the Southern Ocean employing eddy-resolving models, such as Kong and Jansen (2021) and Xing et al. (2023), generally confirm that large standing meanders and gyres in the Southern Ocean play a dominant role in meridional heat transport, and also reduce the sensitivity of the "effective diffusivity" (i.e. the combined effect of standing and transient eddies) to the representation of mesoscale eddies, although some sensitivity

to eddy representation clearly remains (Kong and Jansen, 2021). Resolved mesoscale eddies may also result in an enhancement of the Southern Ocean gyre strength (Sauermilch et al., 2021), an effect that could enhance the gyre-correlated mixing pathway we have identified in this study.

In addition to the representation of mesoscale eddy effects via along-isopycnal diffusion and skew fluxes with a constant eddy diffusivity, and GM coefficient, we use a constant vertical diffusivity which means that we are missing the potential effects of enhanced diapycnal mixing near topography (Mashayek et al., 2017). The effect of isopycnal and diapycnal mixing rates on abyssal watermass composition has previously been investigated by Jones and Abernathey (2019), who find that enhanced isopycnal mixing increases the AABW concentration relative to NADW in the abyssal ocean, while increased diapycnal mixing leads to gradual replacement of NADW and AABW by Indo-Pacific surface waters. We note that we generally find larger AABW concentrations and smaller NADW concentrations in the abyssal ocean than those found by Jones and Abernathey (2019) [3]. We attribute this distinction to different choices in model configuration between our two studies that influence the overall circulation –most notably, the setup employed by Jones and Abernathey (2019) generates a substantially deeper mid-depth cell, which likely explains the greater overall abundance of ventilation NADW in the abyssal ocean seen in their results.

Our limited resolution, as well as the highly idealized topography, also limit our ability to fully capture the role of the Southern Ocean gyres. Although the overall size of the gyre (about $10 - 20^{\circ}$ in latitude and $20 - 50^{\circ}$in longitude) is sufficiently large to be reasonably resolved in our model, the northward branch (which is effectively a western boundary current) is likely affected by the limited resolution and almost certainly affected by the details of the topography. More work is therefore needed to quantify the role of the gyre under more realistic topography and higher resolution. Wilson et al. (2022), for example, found

3. Our “AABW" restoring domain is roughly equivalent to the combined “Channel" tracer restoring fields in Jones and Abernathey (2019)

that a zonal ridge north of a polar gyre in the Southern Ocean (broadly representative of the Pacific-Antarctic Ridge in the real ocean) can reduce poleward heat transport by the gyre in an eddy-resolving simulation, although this effect is partially compensated by an increased southward transport by transient eddies across the zonal barrier. Qualitatively consistent with our results, Sauermilch et al. (2021) found that the enhanced Southern Ocean gyres present during the initial opening of the Tasman / Drake Passage gateways heavily influenced southwards heat transport and the overall composition of the Southern Ocean in eddy-resolving simulations. Similar tracer experiments to the one performed here could examine the extent to which the linear relationship between the gyre strength and the meridional mixing towards Antarctic Bottom Water formation regions holds in the presence of zonal topographic barriers and/or Earth-like topography in present and past continental configurations.

3.5.2 Implications

Our results highlight the role of Southern Ocean topography in affecting the pathways of abyssal water masses, an effect that is qualitatively consistent with previous studies. Specifically, the role of the gyre in modulating the prevalence of former NADW versus surface waters in the abyssal cell is broadly consistent with Talley (2013) and Reeve et al. (2019), who suggest that most of the upwelled NADW that enters the ACC is fed into bottom water formation regions near the Weddell and Ross Gyres along with entrained water masses that are able to cross the Subantarctic Front. The limited amount of direct NADW ventilation in the abyssal Indo-Pacific is consistent with the general picture of the modern day overturning circulation (i.e. Talley, 2013; Lee et al., 2019), which suggests that most NADW entering the SO upwells before making its way into the Indo-Pacific as AABW. The strong relationship we observe between direct NADW ventilation in the abyssal Indo-Pacific and the strength of the mid-depth cell is expected, given the necessity of NADW to enter the Southern Ocean before it can make its way into the Indo-Pacific. The approximately linear relationship be-

tween ventilation NADW in the abyssal Indo-Pacific and mid-depth cell strength suggests that the proportion of NADW entering the Southern Ocean that makes it directly into the abyssal Indo-Pacific is relatively constant, although we note that this proportionality is likely to only hold for given rates of isopycnal and diapycnal mixing (c.f. Jones and Abernathey, 2019). The relative concentration of NADW in the abyssal Indo-Pacific is also expected to be sensitive to the AABW formation rate (Li et al., 2023), which does not vary much across the simulations considered here.

The role of the Southern Ocean gyre in diluting upwelling NADW and shifting AABW composition may have implications for the climate during the Last Glacial Maximum (LGM), during which time the Southern Ocean is believed to have played a central role in reducing atmospheric CO_2 (Broecker, 1991; Sigman et al., 2010). It has been hypothesized that an expansion of permanent sea ice around Antarctica drove a shoaling of NADW, an isolation of the abyssal cell, and a subsequent reduction in atmospheric CO_2 as upwelling deep water remained insulated from the atmosphere and thus able to store carbon for a longer time (Stephens and Keeling, 2000; Ferrari et al., 2014; Marzocchi and Jansen, 2019; Nadeau et al., 2019). Our results suggest that a gyre-driven exchange between upwelling deep water and northern surface waters may alter the overall composition of the abyssal cell, a processes which could damp the effect of increased sea ice cover on abyssal carbon storage.

It is important to note that the surface mixing accomplished here by the Southern Ocean gyre is not readily apparent in the zonally integrated MOC, which points to the limitations of relying on zonally-integrated theory or diagnostics to describe the structure of the ocean's large-scale circulation. This is particularly important when attempting to account for the net exchange of water masses between the mid-depth and abyssal cells. Previous work has suggested that the overlap between the mid-depth and abyssal cells in potential density space provides a key metric for the advective exchange between the mid-depth and abyssal cells (e.g. Ferrari et al., 2014; Nadeau et al., 2019; Baker et al., 2020; Nadeau and Jansen, 2020). While our exchange tracer results do not directly measure the advective exchange between

the mid-depth and abyssal cells, they suggest that the net transfer of tracers between NADW and the abyssal Indo-Pacific may be more affected by the overall strength of the mid-depth cell and the Southern Ocean gyres then by the overlap between the two overturning cells.

3.6 Summary and conclusions

In this work we have investigated the effect of topography and wind-forcing in the Southern Ocean on the composition of the abyssal ocean, using an idealized ocean GCM. As found in previous studies, the introduction of Southern Ocean topography results in changes to the large-scale circulation, most notably a reduction in mid-depth cell strength and a gyre spin-up with increasing ridge height. We characterized the effect of these circulation changes on the abyssal ocean water mass composition in terms of 'ventilation' tracers that reflect the surface-origin of deep water masses and 'exchange' tracers that are allowed to circulate through the high-latitude Southern Ocean without being subject to surface restoring, thus allowing us to decompose AABW into former NADW versus water from lower latitude sources. Our main findings are summarized as follows:

- The mid depth cell is largely insensitive to Southern Ocean topography until the topographic height begins to intersect with the lower NADW isopycnals, after which mid depth cell strength drops substantially. The abyssal cell in the Indo-Pacific is largely insensitive to higher Drake Passage ridges until the very high (3500m) ridge case is reached.

- In our two-basin configuration the concentration of NADW tracer that directly enters the abyssal Indo-Pacific without contact with the surface is generally small (4-17%), indicating that relatively little NADW directly makes its way into the abyssal Indo-Pacific at depth.

- A large portion of the abyssal Indo-Pacific (26%-76%) is composed of "exchange" NADW (NADW*), indicating that a significant amount of NADW surfacing in the

Southern Ocean enters the abyssal cell as AABW, although this fraction shows significant sensitivity to Southern Ocean topography and wind stress.

- Both the abyssal concentrations of NADW that reaches the abyssal Indo-Pacific directly and of NADW* decrease with increasing ridge height and decreasing Southern Ocean wind stress.

- The changing abyssal concentrations of NADW and NADW* in the Indo-Pacific can be explained primarily by the weakening of the mid-depth cell in the South Atlantic, whereby less NADW makes it out of the Atlantic, and secondarily by the strengthening of the Southern Ocean gyre,whereby upwelling NADW* is exchanged with thermocline and intermediate waters from the northern basins.

Our results highlight the combined role of the mid-depth cell and the Southern Ocean gyre circulation in controlling the transport of tracers into the abyssal Indo-Pacific, a finding that has implications for both our conceptual picture of the current overturning circulation and for deep ocean tracers and carbon storage in past and future climates. However, more work is needed to quantify the role of these mechanisms in more realistic model configurations and in the real ocean.

CHAPTER 4

THE MOC RESPONSE UNDER MORE COMPLEX TOPOGRAPHY

4.1 Introduction

Here we extend our Chapter 3 investigation to more complex topographic setups in an effort to test the robustness of our Chapter 3 results in more complex / Earth-like topographic configurations. The real bathymetry of the Southern Ocean is complex, containing topographic features with both large meridional and zonal extents, and it is unclear whether the exchange pathway described in Chapter 3 will be modified in the presence of more realistic topography. It is thus important to ask how the results from Chapter 3 might or might not be reflected in setups more similar to the real Southern Ocean. The results presented in this chapter take a step towards addressing this question by showing the effect of more complex topography on the surface pathway described in Chapter 3 and the overall ocean circulation.

The topography of the Southern Ocean consists of a system of undersea ridges, seamounts, and outcropping landmasses (Figure 4.1), which act to steer the overlying flow in the horizontal and vertical directions (Killworth, 1992; Youngs and Flierl, 2023) and modify the strength of the ACC and polar gyres (Nadeau and Ferrari, 2015; Patmore et al., 2019). Major topographic features in the Southern Ocean include the Antarctic Peninsula and the nearby Scotia Arc, which together force the Weddell Gyre, the Pacific-Antarctic Ridge, which is associated with the Ross Gyre, and the Kerguelen Plateau, which forces the Kerguelen Plateau Gyre (also referred to as the Australian-Antarctic Gyre). These features differ in multiple ways: the outcropping Antarctic Peninsula effectively acts as a western boundary in the Southern Ocean, for example, and the dynamics of the Weddell Gyre thus more directly resemble those of the northern wind-driven gyres described by the Stommel solution (Sverdrup, 1947; Gordon et al., 1981). The zonal extension of the Scotia Arc, meanwhile, may act to thermally isolate the Weddell Gyre from the ACC (Wilson et al., 2022). The

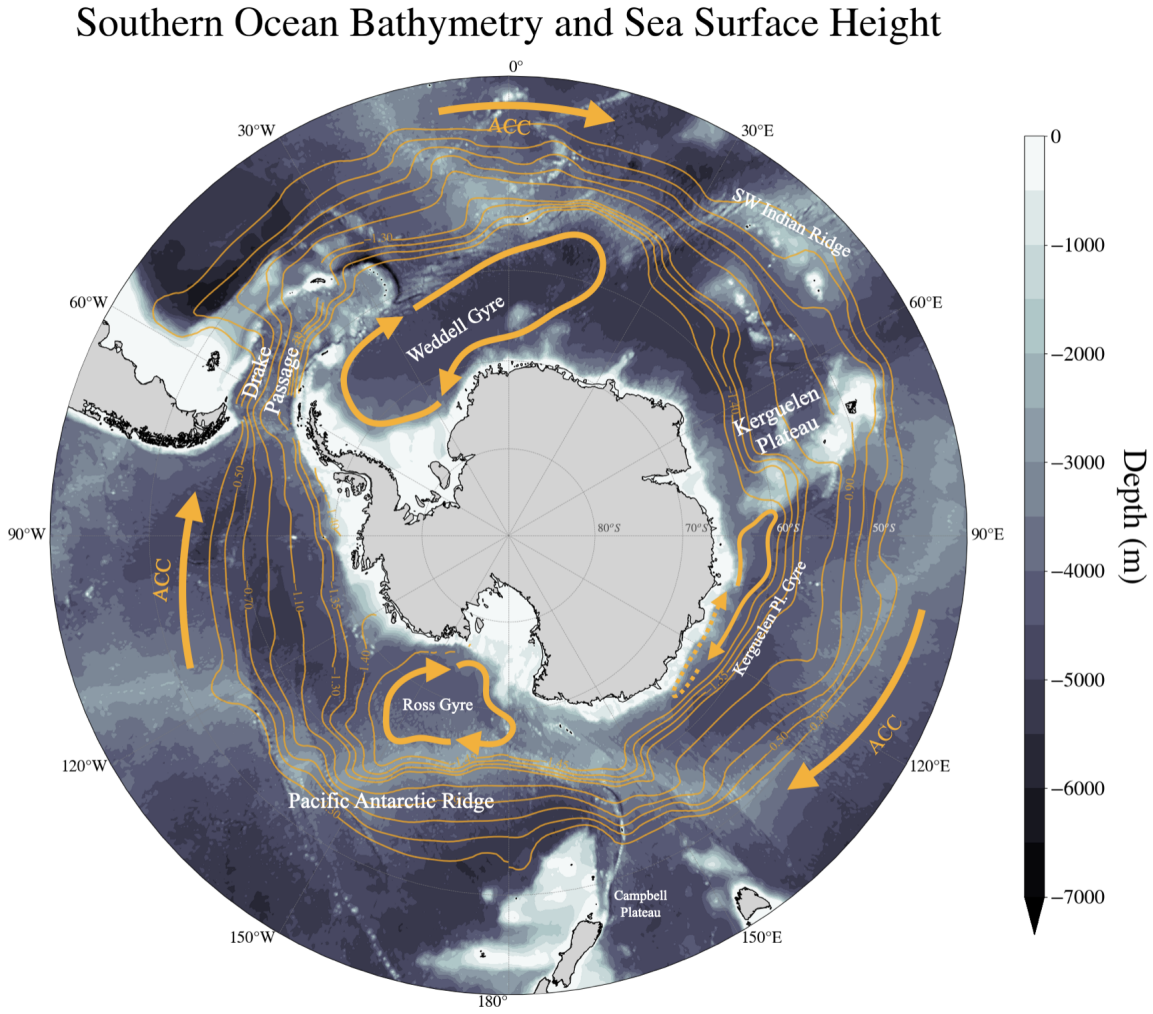

Figure 4.1: Schematic of Southern Ocean bathymetry (filled contours), dynamic sea surface height (thin orange contours), and sketches of major polar gyre circulation features (solid arrows). Bathymetry is taken from the ETOPO 2022 15 Arc-Second Global Relief Model (NOAA National Centers for Environmental Information, 2022). Dynamic sea surface height contours are derived from smoothed yearly-mean SSH values taken from ECCO Central Estimate (Version 4 Release 4) (ECCO Consortium et al., 2022) and are plotted from -0.3m to -1.45m, values roughly corresponding to the Sub-Antarctic Front and the Antarctic Polar Front and enclose the path of the ACC. Major bathymetric features discussed in the text are labeled and include Drake Passage, Kerguelen Plateau, and the Pacific-Antarctic Ridge. Orange arrows outline the major large scale circulation patterns including the polar gyres of the Southern Ocean and the ACC. The dashed arrow corresponding to the eastern return limb of the Kerguelen Plateau Gyre reflects the gyre's weak SSH signal along it's return limb.

Pacific-Antarctic Ridge and the Kerguelen Plateau are in some ways more similar to the submarine ridge used in Chapter 3 due to a lack of outcropping features, but are situated far from Drake Passage and lack significant outcropping meridional boundaries to the north (NOAA National Centers for Environmental Information, 2022). Thus, the gyre circulations associated with the Pacific-Antarctic Ridge and the Kerguelen Plateau arise largely as a consequence of form stress governed by topographic Rossby waves (Stevens and Ivchenko, 1997; Thompson and Naveira Garabato, 2014) without the need for blocked geostrophic contours (Patmore et al., 2019).

The importance of each of the Southern Ocean topographic features to the overall circulation is far from uniform. Both Drake Passage and the Pacific-Antarctic/Campbell Plateau region are associated with the strong Weddell and Ross Gyres, for example, while the polar gyre associated with Kerguelen Plateau is relatively weak (Masich et al., 2015a). Furthermore a majority of the form stress balancing zonal momentum input into the Southern Ocean and modulating the strength of the ACC and polar gyres is across Drake Passage and the outcropping tip of South America (which is also the region associated with the highest rates of deep water upwelling (Tamsitt et al., 2017)) followed by the Campbell Plateau / Pacific-Antarctic Ridge region, with other features such as the Kerguelen Plateau playing a more minor role (Masich et al., 2015a; Wang et al., 2016).

It is thus unclear to what extent the presence of multiple and/or zonal barriers is important to our overall understanding of the Southern Ocean's circulation. Evidence for a strong relationship between multiple ridges and the strength of the ACC is mixed: Wang et al. (2016), for example, found that if one removes the Kerguelean Plateau from the Southern Ocean, the associated form stress becomes redistributed across other topographic features resulting in little change to the overall strength of the ACC. Boer et al. (2022), meanwhile, found that removing different Southern Ocean barriers generally led to an increase in ACC strength, although their models were not run to equilibrium and hence only captured a transient response. Finally, Wilson et al. (2022) found that the addition of a submerged

zonal extension to Drake Passage led to a modest increase in polar gyre strength and a large ($\approx 50\%$) decrease in the strength of the ACC, although their study was carried out using a relatively small Southern Ocean channel extending only $\approx 70^o$ in longitude.

How the MOC and the T_{mix} pathway identified in Chapter 3 may respond to more complex, Earth-like topography is unclear. Efforts to develop analytical theory describing the influence of Southern Ocean topography under present climate are mostly limited to studies characterizing the response of channel models of the Southern Ocean to a single ridge, and tend to find a larger response in the ACC and Southern Ocean gyres with the MOC appearing mostly insensitive to topographic changes (Abernathey et al., 2011; Stewart and Hogg, 2017; Kong and Jansen, 2021; Boer et al., 2022; Wilson et al., 2022). Some effort has been made to characterize the MOC's response to the opening of Drake Passage during the Eocene-Oligocene Transition such as Toumoulin et al. (2020); Sauermilch et al. (2021) and Xing et al. (2022) but these efforts are often restricted to the Southern Ocean and do not generate a mid depth cell. One study by Wang et al. (2016) characterized the response of the AMOC to removing Kerguelen Plateau under Earth-like topography and modern climate, but found a nearly negligible ($< 1\%$) increase in AMOC strength. The response of the MOC and the water mass composition of the abyssal ocean to changing Southern Ocean topography thus remains poorly understood.

Here we take a step towards better characterizing the ocean circulation's relationship to changing Southern Ocean topography by examining the sensitivity of the MOC, the barotropic circulation, and the surface mixing pathway identified in Chapter 3 to slightly more complex Southern Ocean topographic setups. To do so we reconfigure the topographic setups of our Chapter 3 experiments for the moderate wind stress (τ_2) case to include zonal topographic features and additional meridional barriers in the Southern Ocean. We find that the barotropic circulation does respond to these additional topographic features, while the response of the MOC is relatively small. Repeating our tracer release experiments under new topographic setups shows modest changes in ventilation and exchange tracer concentration

that are broadly consistent with the strength of the gyre and mid depth cells as predicted by our conceptual model.

4.2 Methods

4.2.1 Model domain and topographic setup

We use the same overall model setup as that employed in Chapter 3 and some of the earlier description is repeated here. As in Chapter 3, we employ an idealized, ocean-only GCM to simulate the response of an Earth-like MOC to changes in Southern Ocean topography and wind stress forcing. Our model is based on that used in the previous study and on that employed by Nadeau and Jansen (2020) and uses the Massachusetts Institute of Technology General Circulation Model (MITgcm) (Marshall et al., 1997a) with the same vertical and horizontal extent and resolution as that used in Chapter 3.

We employ the flat-bottom "box" ocean basin configuration used in Chapter 3 as a base for the modified topography experiments carried out in this chapter (Figure 3.1). Using our setup, we test the response of the ocean circulation under moderate ($\tau = 0.2N/m^2$) maximum Southern Ocean wind stress to four different topographic configurations under four different ridge height cases (1000m, 2000m, 3000m, and 3500m) for a total of 16 topographic configurations. The modified topographic setups we test here consist of adding a) a 16^o zonal extension of the Drake Passage Ridge, b) a 24^o zonal extension of the Drake Passage Ridge, c) one additional Southern Ocean ridge, and d) two additional Southern Ocean ridges to our base single ridge setup. The modified topographic setups for the 2000m ridge case are shown in 4.2. Note that the additional topography added to each base setup is the same height as the original ridge in each setup, and is 4^o thick in all cases.

We employ an equation of state, surface forcing, and various parameterizations for sub-grid scale mixing and eddy advection identically to those used in Chapter 3 (see section 3.2 for details).

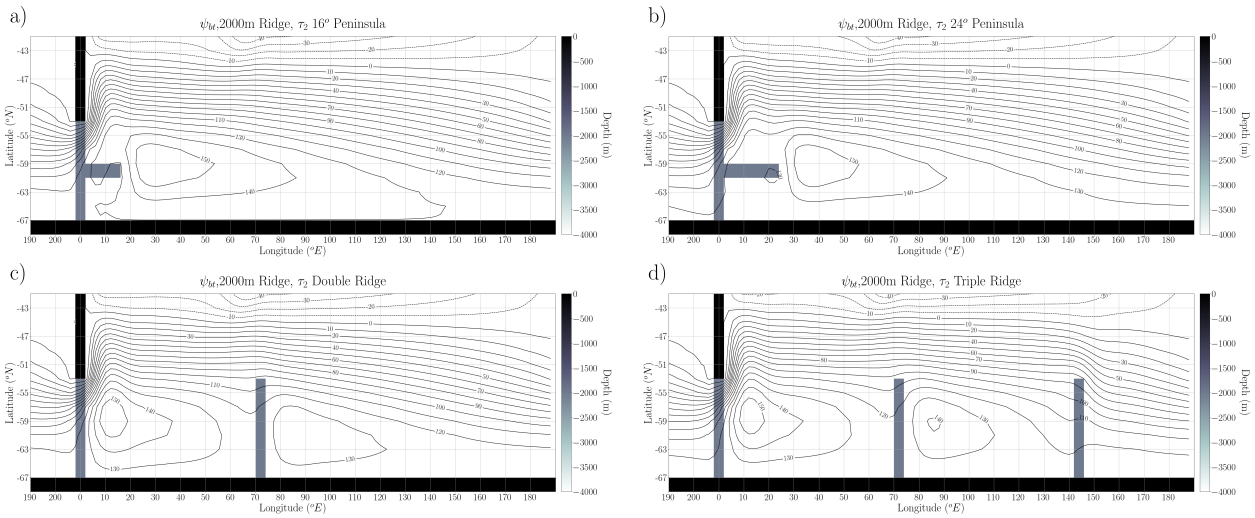

Figure 4.2: Modified topographic setups shown here for the 2000m ridge case with a) a 16^o zonal ridge, b) a 24^o zonal ridge, c) an extra ridge at 70^oE, and d) an extra ridge at 70^oE and an extra ridge at 142^oE. Black contour lines give the barotropic stream function in each case and are spaced at 10Sv intervals. Additional topography is raised to the same depth as the base Drake Passage ridge.

4.2.2 Tracer release experiments

We repeat our tracer release experiment from Chapter 3, employing five passive tracers to track the pathways of water masses through the global circulation. As before, we apply three "ventilation" tracers that track the pathways of water that originates at the surface of the North Atlantic ("NADW"), in the Southern Ocean in the latitude range of Drake Passage ("AABW"), and over the remainder of the global ocean, including the entire Indo-Pacific and the northern Southern Ocean ("surface water," or "SW"). We employ two "exchange" tracers (NADW* and SW* as in Chapter 3) to track the pathways of NADW and SW in the case where they are allowed to travel through the Southern Ocean surface without being restored. As before, the restoring fields of NADW* and SW* mirror those of the ventilation NADW and SW tracers but with no restoring applied in the latitudes of Drake Passage (Figure 3.1e). Refer to Chapter 3 Section 3.2 for further details.

4.2.3 Characterizing the ocean circulation

We characterize the ACC and gyre transport using the barotropic streamfunction given by:

$$\psi_{bt}(x,y) = \int_{y=y}^{y=68^oN} \int_{-H}^{0} \overline{u}(x,y,z)dzdy, \tag{4.1}$$

where H is the ocean depth, $u(x,y,z)$ is the local eulerian velocity in the zonal direction, and the overbar, $(\bar{\cdot})$, denotes the time mean. As in Patmore et al. (2019) and Chapter 3, we define the strength of the ACC, ψ_{acc}, as the net barotropic transport across Drake Passage (measured by taking the barotropic stream function at the southern end of Drake Passage, i.e. $\psi_{bt}(0^oE, 68^oS)$).

We modify our calculation of gyre strength slightly to account for the presence of multiple gyres in the double and triple ridge cases. Here, we define the strength of each gyre as the difference between the maximum barotropic stream function in the longitude band occupied by each gyre and the total ACC transport described by (4.1):

$$\begin{aligned}
\psi_{gyre\ 1} &= \max\left|\max\left|\psi_{bt}(x,y)\right|_{y=68^oS}^{y=54^oS}\right|_{x=0^oE}^{x=70^oE} - \psi_{bt}(0^oE, 68^oS), \\
\psi_{gyre\ 2} &= \max\left|\max\left|\psi_{bt}(x,y)\right|_{y=68^oS}^{y=54^oS}\right|_{x=70^oE}^{x=142^oE} - \psi_{bt}(0^oE, 68^oS), \\
\psi_{gyre\ 3} &= \max\left|\max\left|\psi_{bt}(x,y)\right|_{y=68^oS}^{y=54^oS}\right|_{x=142^oE}^{x=210^oE} - \psi_{bt}(0^oE, 68^oS),
\end{aligned} \tag{4.2}$$

where $\psi_{gyre\ 2}$ and $\psi_{gyre\ 3}$ are only calculated for the double ridge and triple ridge cases, respectively.

As in Chapter 3, we quantify any response of the global overturning circulation to changes in Southern Ocean topography using the isopycnal streamfunction, $\psi(y,b)$, as defined in Eq. 3.4, which gives a useful representation of the material transport pathways of the deep ocean (Nurser and Lee, 2004; Ferrari and Ferreira, 2011). As before, we characterize the MOC in terms of the mid depth cell, ψ_{atl}, and the abyssal cell, ψ_{ip}, and the rate of intermediate

water production, ψ_{surf}. Refer to Chapter 3, Section 3.2 for details.

4.3 Results

4.3.1 ACC and gyre transport

We quantify the response of the Southern Ocean's barotropic circulation to changing topographic configuration in terms of the strength of the ACC (ψ_{acc}, (4.1)) and the strengths of the Southern Ocean gyres (4.2) (Figure 4.3). The strength of the ACC is, as in Chapter 3, dependent on the height of the topographic barriers to first order (Figure 4.3a): the average ACC strength for the modified topography cases falls off with increasing topographic height from a maximum of 142Sv in the 1000m height case to 40 Sv in the 3500m height cases. The effects of modified topography tend to be much smaller than overall topographic height. The introduction of a zonal ridge tends to strengthen the ACC slightly, with longer peninsulas leading to further ACC strengthening, on the order of 5% to 10%. The response of the ACC to the double ridge case is small, with little change in strength for the 1000m height case and modest increases of 4.1% and 5.0% in the 2000m and 3000m height cases, respectively. The response of ACC strength to the triple ridge case is lower than that for the double ridge case, generally only leading to a decrease of $1\% - 3\%$ in ACC strength.

In contrast to the ACC, the Southern Ocean gyres respond strongly to changing topographic setup (Figure 4.3b), with all additional topographic setups leading to a of weakening in the Drake Passage gyre. The introduction of zonal barriers tends to decrease the gyre strength by a similarly large amount across different heights: the 37.1Sv gyre present in the 1000m height case sees a decline of -14.6 Sv with a -16^o ridge and a decline of -16.7Sv with a 24^o ridge. The decline in gyre strength due to the zonal ridge is somewhat less severe for the 2000m and 3000m height cases and is approximately -12.5Sv and -12.7Sv for a 16^o ridge in the 2000m and 3000m cases, respectively, and -15Sv and -16Sv for the 24^o ridge in the 2000m and 3000m cases, respectively. The decline due to the zonal ridge in the 3500m

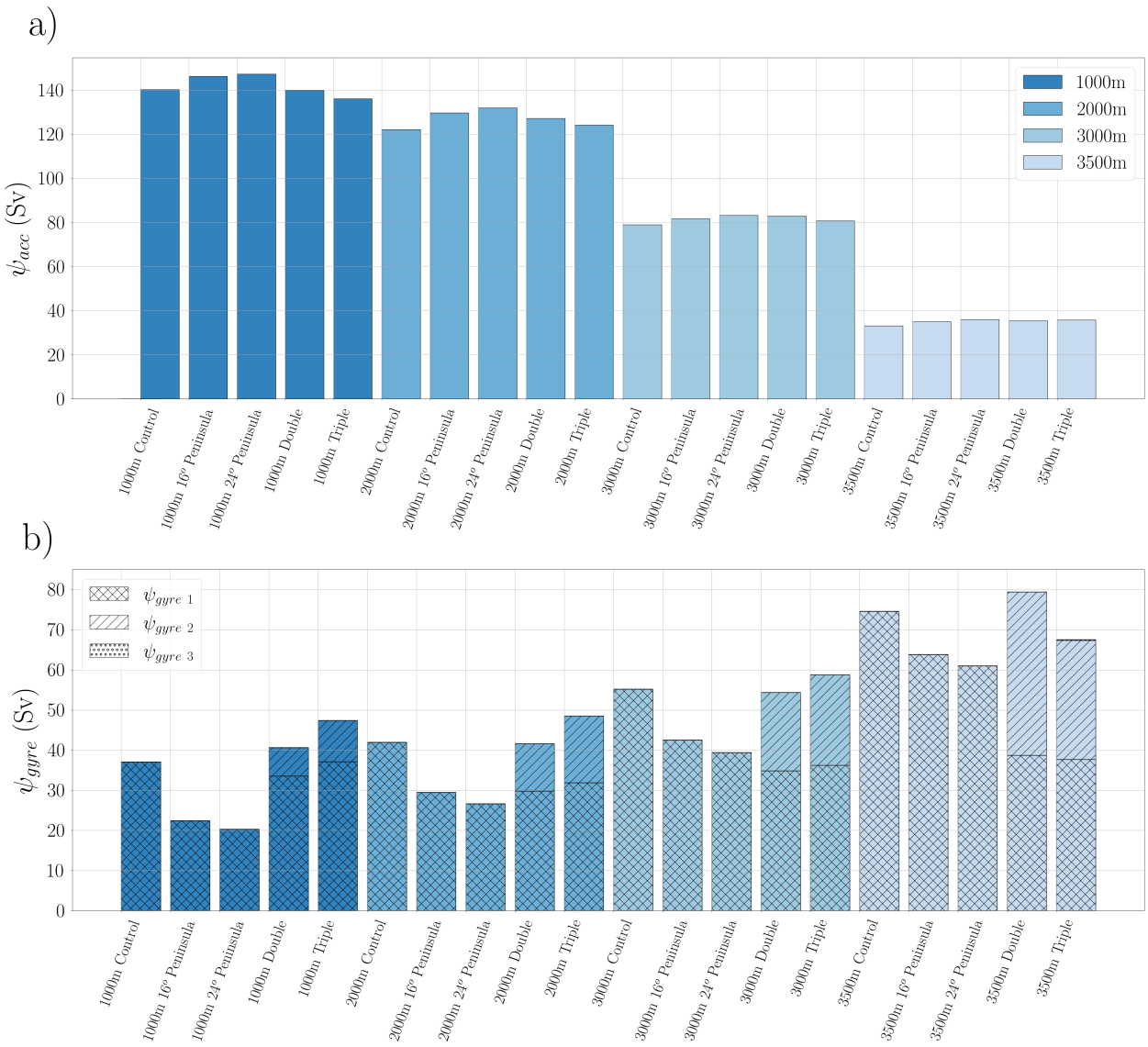

Figure 4.3: Summary of the barotropic response across all runs. a) ACC strength, ψ_{ACC} and b) gyre strength, ψ_{gyre} vs topographic setup. Bar color denotes the height of the topographic features used in each case. Control runs using a single ridge in the vicinity of Drake Passage (ie.e the setups employed in Chapter 3) are also shown. In the case of multiple Southern Ocean gyres the strength of each resolved gyre is shown using hatches (see legend).

case amounts to a -10.8v and -13.6Svdecline for the 16^o and 24^o ridges, respectively.

Additional ridges generate a secondary gyre circulation in the Southern Ocean in both the double and triple ridge cases (Figure 4.2, Figure 4.3), but no significant third gyre is generated when a third ridge is added. Here we refer to the gyre closest to Drake Passage as the "primary" gyre ($\psi_{gyre\ 1}$), the gyre that forms in the lee of the 70^oE ridge as the "secondary" gyre ($\psi_{gyre\ 2}$), and any gyre that forms in the lee of the 142^oE ridge as the "tertiary" gyre ($\psi_{gyre\ 3}$). In the 1000m, 2000m, and 3000m height double ridge cases the strongest gyre forms in the lee of Drake Passage (with 33.5Sv, 29.8Sv, 34.9Sv, for the 1000m, 2000m, and 3000m heights, respectively), with a weaker secondary gyre forming in the lee of the additional ridge (7.1Sv, 11.8Sv, 19.5Sv, for the 1000m, 2000m, and 3000m heights, respectively). The 3500m double ridge height case is an exception, with the secondary gyre strength (40.7Sv) slightly exceeding that of the primary gyre (38.7Sv). The third ridge does not generate a significant tertiary gyre, but modifies the strength of both the primary and secondary gyres. With a triple ridge setup we generally see a small increase in both the strength of primary and secondary gyres over the double ridge case. The 3500m triple ridge case is an exception, with a weakening of both the primary gyre and the secondary gyre and the formation of a very weak tertiary gyre (0.17Sv).

4.3.2 MOC response

The MOC responds to different topographic configurations (Figure 4.4), although the relationship is subtle and does not differ substantially from the single ridge control runs. The mid depth cell (ψ_{atl}) ranges from a minimum of 1.9Sv in the 3500m, double ridge case, to a maximum of 10.5Sv in the 2000m, 16^o zonal ridge case (Figure 4.4a). As in Chapter 3, the mid depth cell appears largely insensitive to changing topographic configuration for low topography (1000m-2000m height cases), likely due to lower Southern Ocean topography failing to intersect NADW isopycnals as they upwell through the Southern Ocean. The mid depth cell weakens substantially once topography passes 3000m (reaching an average strength

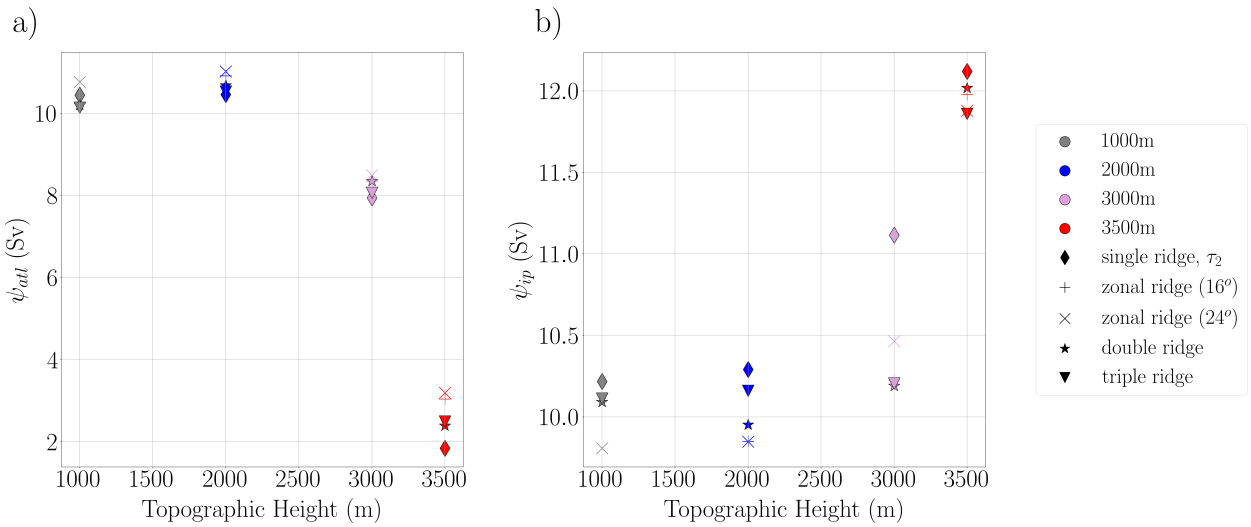

Figure 4.4: MOC response to changing topographic features across all runs vs topographic height. a) Mid depth cell strength, ψ_{atl}, vs topographic height (m). b) Abyssal cell strength, ψ_{ip}, vs topographic height (m). Marker colors and shapes give the height and topographic configuration and wind stress, respectively, of the undersea topographic features used in each run (see legend). Note that we include control runs from our Chapter 3 results that only include a Drake Passage ridge (diamond markers).

of 8.2Sv and 2.2Sv over all 3000m and 2500m height cases, respectively), but appears to be largely insensitive to the specific topographic configuration employed.

The strength of the abyssal cell (ψ_{ip}) changes in response to both topographic configuration and height (Figure 4.4b), although the overall range is fairly weak, varying between $10Sv$ and $12Sv$ across all simulations. Modified topography leads to a small weakening of the abyssal cell over the control (single ridge) cases for each of the 1000m, 2000m and 3000m height cases of around $O(0.5\text{Sv})$. As in Chapter 3, the strongest abyssal cell strength occurs for the 3500m cases.

4.3.3 Passive tracer response

Additional topography modifies the ventilation tracer composition of the abyssal ocean, but the overall relationships between tracer concentrations and circulation changes remain consistent with those observed in Chapter 3. Average tracer concentrations below 2000m in the abyssal Indo-Pacific vs the various circulation metrics used in Chapter 3 are shown

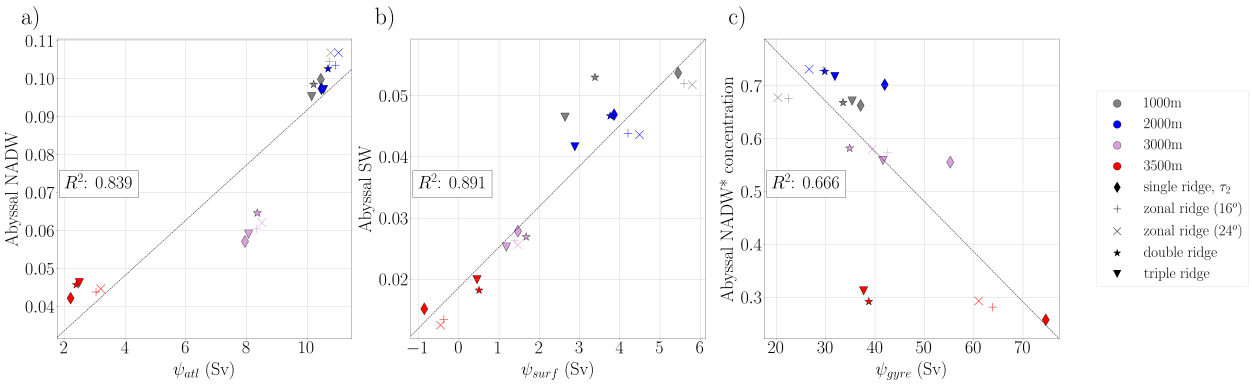

Figure 4.5: Ventilation and exchange tracer concentrations in the abyssal (>2000m depth) Indo-Pacific across runs with additional topography and control ridge setups. a) Abyssal NADW concentration vs mid depth cell strength, ψ_{atl}. b) Abyssal SW concentration vs ψ_{surf}. c) Abyssal NADW* concentration vs primary gyre strength, $\psi_{gyre\ 1}$. Marker colors give the height of undersea topographic features used in each run. Marker shape give the topographic configuration used in each run (see legend).

in Figure 4.5. The concentrations of NADW that make up the abyssal Indo-Pacific are generally small, ranging from $\sim$ 4.0% for the 3500m control case to $\sim$ 10% in the 1000m double ridge case, and are correlated with the strength of the mid depth cell ($R^2 = 0.839$, Figure 4.5a). Abyssal SW concentrations are small across all topographic setups, ranging between 1.5% and 5.2%, and are tightly correlated with the rate of intermediate water production ($R^2 = 0.891$, Figure 4.5b), as found in Chapter 3. The majority of the abyssal Indo-Pacific is composed of AABW, which ranges between 80.0% in the 1000m 24^o peninsula case to 93.6% in the 3500m double ridge case, and is negatively correlated with the strength of the mid depth cell ($R^2 = 0.840$, not shown).

As with the ventilation tracers, exchange tracers exhibit a somewhat weaker correlation with the strengths of the primary gyre and mid depth cell that can be reconciled using our conceptual model from Chapter 3.

4.3.4 Revisiting our analytical model under modified topography

In Chapter 3 we presented a simple conceptual model that predicts the abyssal exchange tracer concentration via T_{mix}, an exchange pathway between the surface of the mid- to

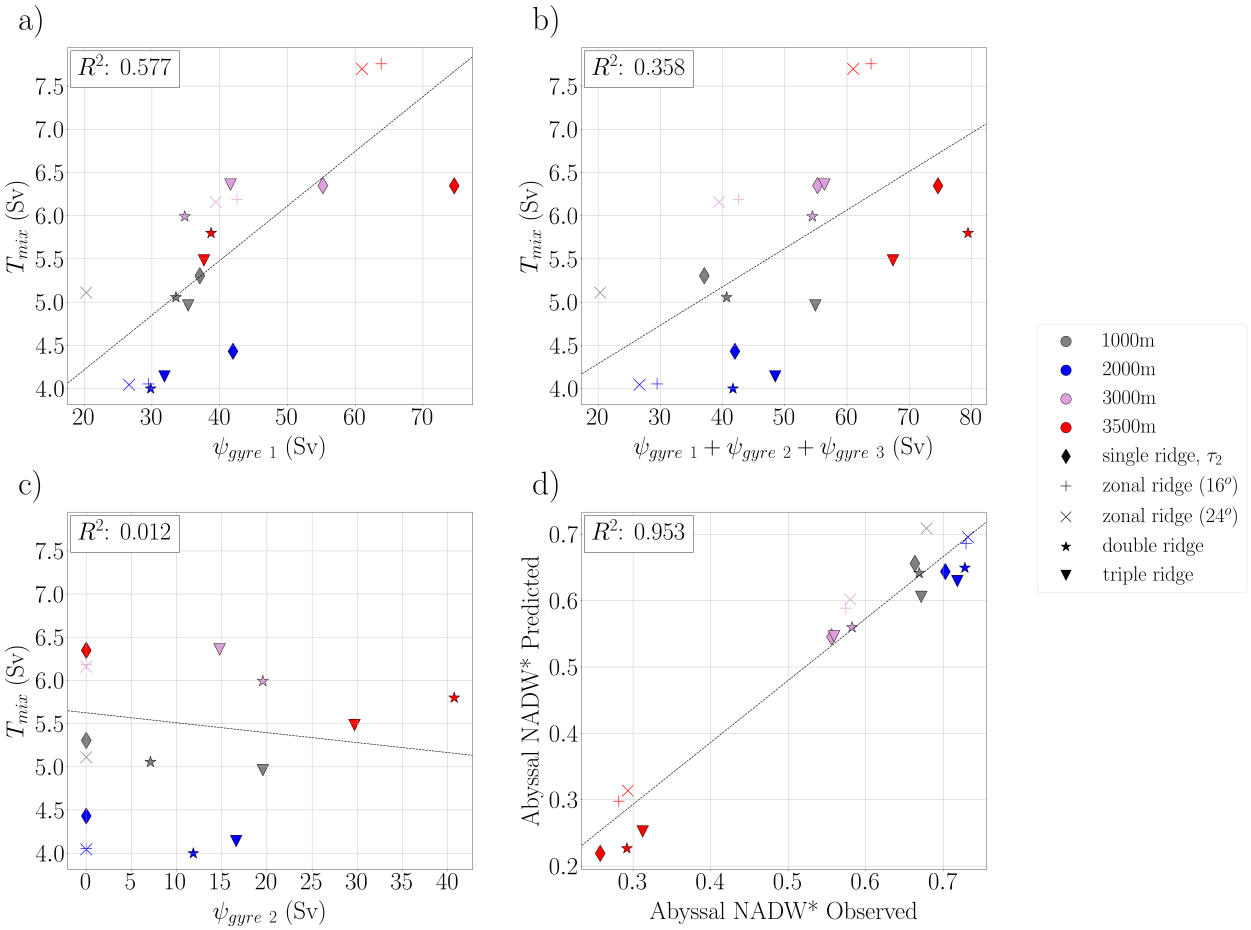

Figure 4.6: Applying our previous analytical framework for T_{mix} calculated via (3.9) (Chapter 3) to our results under modified topography. a) T_{mix} vs the primary gyre, ie. $\psi_{gyre} = \psi_{gyre\ 1}$. b) T_{mix} vs the cumulative gyre strength, i.e. $\psi_{gyre} = \psi_{gyre\ 1} + \psi_{gyre\ 2} + \psi_{gyre\ 3}$. c) T_{mix} calculated via (3.9) vs the secondary gyre, i.e. $\psi_{gyre} = \psi_{gyre\ 2}$. d) Predicted abyssal NADW* concentration (using $\psi_{gyre} = \psi_{gyre\ 1}$) vs observed abyssal NADW*. Red dashed lines in a) and b) give the fitted relationship from Chapter 3, $T_{mix} = 0.062\psi_{gyre} + 3.14Sv$.

low-latitude ocean basins and the abyssal ocean. We revisit this relationship under the modified topographic setups employed in this chapter. Our results show that the response of abyssal NADW* to changing topographic setups closely resembles that derived in Chapter 3. Here we further test our conceptual model for a predominantly gyre-driven mixing pathway, T_{mix}, that links the strength of the gyre to the rate of exchange tracer uptake by the abyssal Indo-Pacific.

It is unclear how the presence of additional gyres in the double and triple ridge setups affect our ability to predict $C_{NADW^*_{abyss}}$ (3.10) using gyre strength. To that end, we compare T_{mix} to two different metrics of gyre strength, ψ_{gyre}: a) solely using the primary gyre, $\psi_{gyre} = \psi_{gyre\ 1}$ and b) using the cumulative strength of the additional gyres, should they be present, $\psi_{gyre} = \psi_{gyre\ 1} + \psi_{gyre\ 2} + \psi_{gyre\ 3}$. In general, the previous relationship between T_{mix} and ψ_{gyre} given by (3.9) holds relatively well when only the primary gyre is employed ($R^2 = 0.577$, Figure 4.6a) although with increased spread relative to the relationship found in Chapter 3. The fit degrades substantially with the addition of the secondary and tertiary gyres ($R^2 = 0.358$, Figure 4.6b) to the T_{mix} calculation, indicating that the secondary gyre circulation does not significantly contribute to T_{mix}. Indeed, the fit between T_{mix} and $\psi_{gyre\ 2}$ alone has R^2 value of 0.012, or almost no correlation (Figure 4.6c). Applying (3.9) with $\psi_{gyre} = \psi_{gyre\ 1}$ to (3.10), we are able to repeat the prediction of C_{NADW*} as performed in Chapter 3 quite well ($R^2 = 0.953$, Figure 4.6d).

4.4 Discussion

4.4.1 The ocean circulation under modified topography

Our simulations predict that topographic height is the main factor that influences the response of the ACC to changing topographic configuration, a relationship that holds between the simple ridge setups used in Chapter 3 and the more complex setups employed here. The relative insensitivity of the ACC to additional topography is consistent with previous

modeling studies (Ward and Hogg, 2011; Wang et al., 2016), and reflects the efficient redistribution of zonal momentum in the Southern Ocean to balance the ACC under changing topographic conditions. Our results agree with those of Wang et al. (2016), who showed that there is little change to the overall ACC transport through Drake Passage with the removal of large scale submarine features (i.e. the Kerguelen Plateau) under Earth-like topography. Wang et al. (2016) attribute this partially due to the fact that under removal of Southern Ocean submarine features, the topographic form stress that balances zonal momentum input by wind stress at the surface is redistributed efficiently across other Southern Ocean topographic barriers. We investigated the changes in topographic form stress that accompanied additional ridges in our case and conclude that this is happening in our simulations as well (not shown).

The Southern Ocean gyres show a mixed response to additional topographic features. The addition of zonal ridges in the vicinity of Drake Passage tends to result in a large decrease in primary gyre strength, in some disagreement with the modeling study of Wilson et al. (2022) which showed a modest increase in gyre strength with the addition of a zonal barrier. However, the gyre circulation described in Wilson et al. (2022) was localized south of the added zonal barrier in Drake Passage and partially forced by easterly winds near the Antarctic Coast, making its circulation distinct from the gyre present in our study. The reduction in gyre strength observed here may instead be related to the increase in effective zonal width of the topographic barrier: a study by Patmore et al. (2019), for example, showed that increasing the width of a meridional barrier in the Southern Ocean leads to a decrease in the cross-topographic pressure gradient and form stress across the barrier, which subsequently leads to a reduction in gyre circulation and an increase in ACC strength. In our models, the eastward displacement of the gyre with a zonal barrier may lead to an effective increase in topographic width and a reduction in topographic form stress in a manner similar to that described in Patmore et al. (2019).

The addition of secondary and tertiary ridges tends to generate a strong primary gyre

that is moderately weaker than in the single ridge case, a weak secondary gyre, but no tertiary gyre (with the addition of third ridge). The reduction in primary gyre strength with additional meridional barriers is to be expected as more barriers cause topographic form stress to become more evenly distributed throughout the channel (Masich et al., 2015b; Wang et al., 2016). The fact that the primary gyre tends to remain the stronger than the secondary gyre may be due to its geographic location: the primary gyre is situated in the vicinity of Drake Passage where a portion of the local geostrophic contours intersect with the southern tip of South America, while no such northern barrier exists in the vicinity of the other ridges. Blocked geostrophic contours lead to a recirculation due to Sverdrup balance (LaCasce and Isachsen, 2010) and have been shown to increase the strength of topographically-forced gyres in a Southern Ocean channel (Nadeau and Ferrari, 2015). However, gyre circulation in the Southern Ocean do not necessarily need blocked geostrophic contours to form (Patmore et al., 2019), and the secondary gyre that forms in our study is likely forced solely by bottom form stress acting to balance wind stress curl at the surface. With this in mind the resulting circulation is not surprising, with the strength of the primary gyre enhanced by blocked geostrophic contours and the secondary gyre, while contributing to the net topographic form stress in the channel, exhibiting a weaker circulation.

The response of the MOC to changing Southern Ocean topography has received less theoretical attention than the barotropic circulation, and studies examining the effect of Southern Ocean topographic features on the MOC are usually either a) restricted to the Southern Ocean south of Cape Horn Africa, or b) employ quasi-realistic topography, complicating theoretical insight (Abernathey et al., 2011; Toumoulin et al., 2020; Boer et al., 2022). Here we find that the strength of the mid depth and abyssal cells are relatively insensitive to alternative topographic setups beyond a simple ridge in Drake Passage, with topographic height being the main predictor of the strength of the mid depth cell while the abyssal cell only shows modest changes. An interesting result found in this study (as well as Chapter 3) is the relative insensitivity of the mid depth cell to Southern Ocean topography below

3000m, after which the mid depth cell drops off with increasing ridge height. This relationship holds in our study regardless of the topographic setup employed, and the drop off in mid depth cell strength coincides with the intersection of lower NADW isopycnals with the Drake Passage ridge in all cases (Figure 4.7). This robust result has not, to our knowledge, been explored previously in idealized modeling studies, but an in-depth investigation into its nature is beyond the scope of this study.

4.4.2 Passive tracers and gyre-driven surface mixing

The passive tracer concentrations presented above can give us an idea for how the NADW ventilation rate of the abyssal ocean (shown in Chapter 3 to be directly related to the strength of the mid depth cell) and the rate of exchange between the interconnected MOC and low latitude surface waters (shown in Chapter 3 to be related to the strength of the Southern Ocean gyre) respond to changing topographic setups. Our results indicate that the both the dependence of NADW on mid depth cell strength and the correlation between the Southern Ocean gyre strength and mixing driven exchange, T_{mix} (3.9), remains robust under modified topography. We attribute this result to the relative insensitivity of the mid depth cell to different Southern Ocean topographic configurations and on the robust effect of the primary gyre on tracer transport. Such a result is not necessarily surprising: all of the additional topographic features included here are localized to the Southern Ocean and only the Drake Passage ridge is observed to intersect substantially with upwelling NADW isopycnals (Figure 4.7). Still, it is useful to confirm that the rate of NADW injection into the abyssal Indo-Pacific remains proportional to the amount of NADW entering the Southern Ocean via the mid depth cell.

The strong relationship between the mixing-driven pathway, T_{mix}, as predicted by (3.9), and the strength of the Southern Ocean gyre holds up under varying topographic setups (Figure 4.6), supports our hypothesis that gyre-driven mixing at the surface of the Southern Ocean plays a key role in setting the composition of the abyssal ocean. Specifically, T_{mix} is

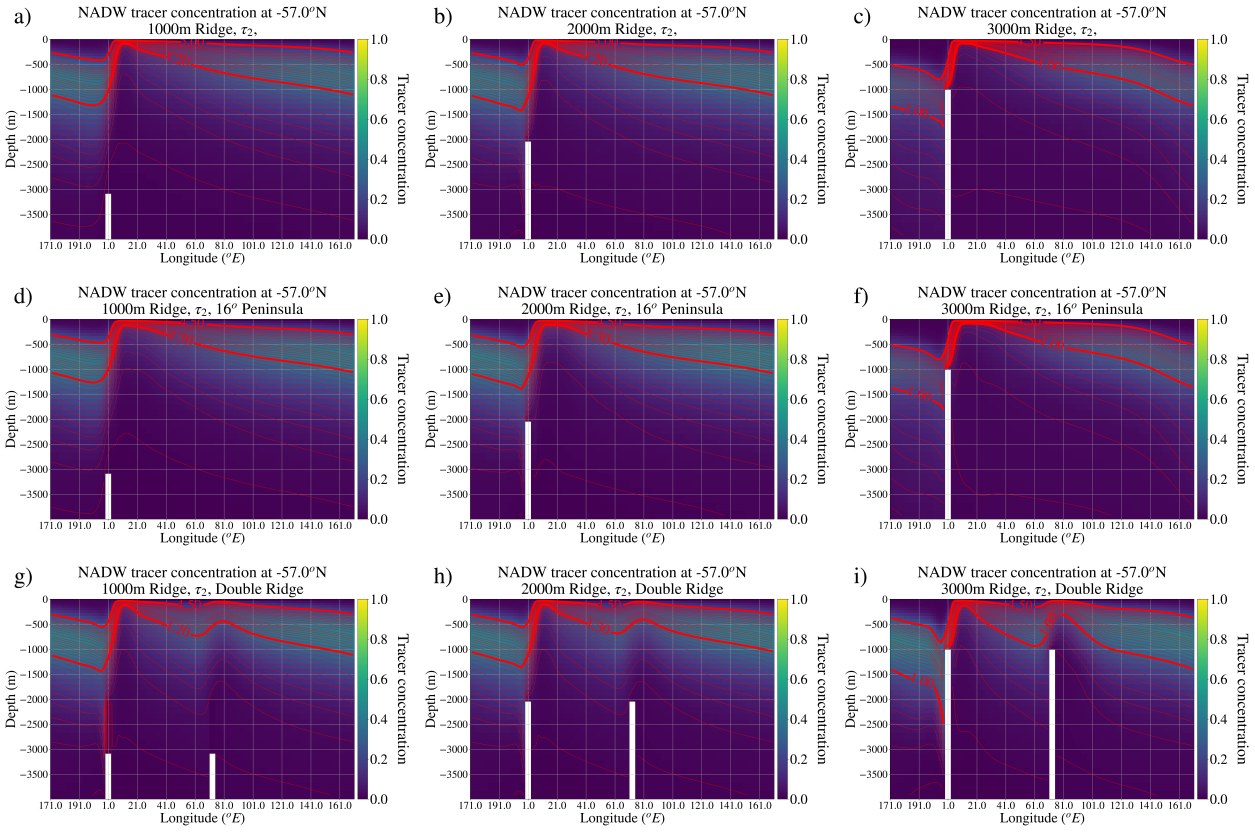

Figure 4.7: Evidence for NADW isopycnals intersecting with the Drake Passage ridge once topographic height reaches 3000m across several example topographic cases. Topographic height cases of 1000m, 2000m, and 3000m for the single ridge, 16^o peninsula ridge, and double ridge setups are shown. Longitude-depth transects of NADW concentration are shown taken at -55^oN, the northernmost latitude of Drake Passage. Isothermal surfaces are overlaid as red contours. The upper and lower bold contours give the isotherms corresponding to the maximum and minimum temperatures of NADW ($T_{NADW_{max}}$ and $T_{NADW_{min}}$ in the text) as it enters the Southern Ocean.

most highly correlated with the strength of the primary gyre, suggesting that the secondary (and tertiary) gyres do not play a similar role in delivering surface waters across the ACC and to the bottom water formation regions around Antarctica. However, both the primary and secondary gyres are associated with regions of high upwelling of former NADW (Figure 4.8) which, although not obviously related to the T_{mix} pathway, points to their importance in governing the net upwelling pathways of dense water to the surface.

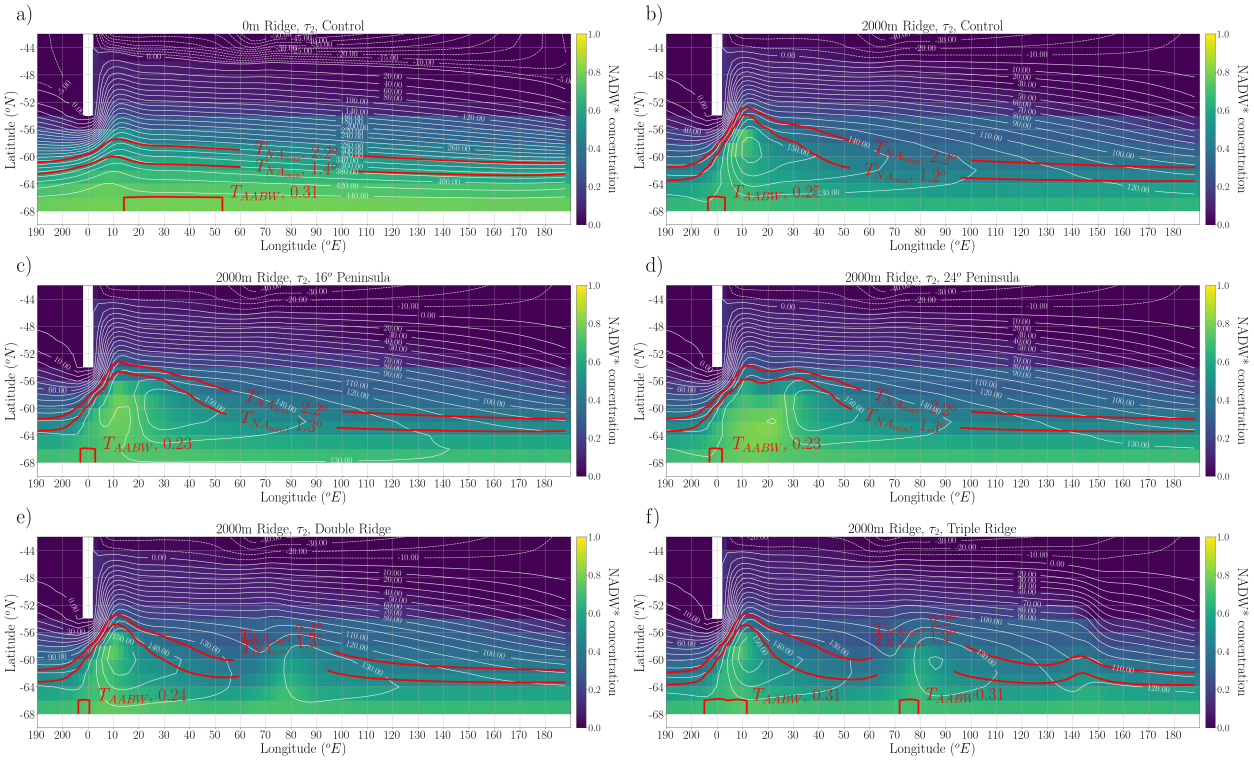

Figure 4.8: Surface NADW* tracer concentrations, barotropic circulations, and temperature across the 0m ridge and various 2000m ridge setups under medium wind stress forcing ($\tau = 0.2N/m^2$). Surface tracer concentrations of NADW* are shown for each run and are plotted between 0 and 1. The barotropic circulation is give by white contours at 10Sv intervals. Surface temperature contours are shown in red and show the maximum ($T_{NADW_{max}}$) and minimum ($T_{NADW_{min}}$) temperatures of NADW as it enters the Southern Ocean, as well as the temperature of AABW, T_{AABW}, defined here as the minimum temperature outcrop at the surface of the Southern Ocean. Absolute temperature values corresponding to each contour level are also shown.

Several characteristics of the primary gyre may point to why it is more important to T_{mix} than the secondary gyre in our simulations. The primary gyre generally reaches farther north towards the SW* restoring regions than the secondary gyre (Figure 4.8), which may enhance

the rate of horizontal mixing between upwelling NADW* and SW* at the northern boundary of the gyre circulation. The primary gyre also tends to be more closely associated with the primary AABW formation regions than the secondary gyre in our simulations (Figure 4.8), which may lead to greater control over the composition of the abyssal ocean. Finally, the primary gyre's close proximity to Drake Passage may play a role: the northern end of Drake Passage represents the southernmost deflection of the ACC and exhibits high surface SW* concentration, which may lead to increased exchange between SW* and NADW*. Given that we would eventually like to tie our results to the real ocean circulation, a more detailed investigation into the role of the different gyres in tracer exchange between the mid-latitudes and the AABW formation regions would be a fruitful avenue for future research.

4.5 Conclusions

Here we add to the current body of modeling studies exploring the response of the large scale ocean circulation to changes in Southern Ocean topography. Using our setup from Chapter 3 as a template, we have conducted a series of sensitivity experiments to investigate the effects of additional Southern Ocean topographic features on the global ocean circulation and on the horizontal mixing across the ACC. For simplicity and due to computational constraints we limit our investigation to a) adding zonal extensions to the Drake Passage sill and b) adding additional meridional ridges throughout the Southern Ocean domain. Our findings are summarized as follows:

- The response of the ocean's circulation to changing Southern Ocean topographic configuration largely comes in the form of changes to its barotropic streamfunction, i.e. the strength of the ACC, ψ_{acc}, and the strengths of the Southern Ocean gyres, $\psi_{gyre\ 1}$, $\psi_{gyre\ 2}$, and $\psi_{gyre\ 3}$, when present. In general, zonal extensions to the Drake Passage ridge lead to weakened Southern Ocean gyres and modest increases in ACC circulations, while additional ridges lead to the formation of secondary gyres while weakening

the primary gyre and having little effect on the overall strength of the ACC.

- The MOC as a whole is less sensitive to changing topography than the barotropic stream function, with the strength of the mid depth cell largely determined by overall topographic height as discussed in Chapter 3 and the abyssal cell showing a relatively small sensitivity to the topographic setup.

- The relationship between the mixing-driven exchange between the mid and low latitude surface waters and the abyssal ocean (here characterized by T_{mix}), and the Southern Ocean gyre is robust across all topographic setups and is associated with the strength of the primary gyre, i.e. the gyre that forms in the vicinity of Drake Passage.

This study gives preliminary insight into the effect of more complex Southern Ocean topography on the MOC and abyssal water mass composition. However, much work remains to connect our results to the real ocean and to the theoretical picture of the MOC pathways described in Chapter 1 and sketched in Ferrari et al. (2017). Potential avenues for further study are discussed in Chapter 5.

CHAPTER 5

CONCLUSIONS AND FUTURE STUDY

5.1 Conclusions

The MOC is a central component of Earth's climate system, setting the stratification and large scale circulation of the global ocean and controlling the abyssal storage of carbon and heat. The close feedback between the MOC and the broader climate makes its accurate characterization important to understanding shifts in past and future climate. However, fundamental questions remain regarding the overall structure and driving processes of the MOC, and their accurate characterization remains a crucial objective of researchers in our changing world.

In this dissertation we take a step towards establishing a more comprehensive view of the global MOC that accounts for modern, observation-based predictions of its structure and the role of complex topography in the Southern Ocean. In Chapter 1 we present the fully closed water mass decompositions of the major limbs of the MOC using ECCO, a state-of-the-art reanalysis product. We show that while ECCO's overall representation of the MOC is superficially similar to the MOC predicted by current theory (Cessi, 2019), the primary driving processes behind ECCO's deep and abyssal circulation are fundamentally different from what modern theory predicts. Our main results concerning the ECCO reanalysis product are as follows:

1. The ECCO reanalysis product largely supports the interconnected "figure-eight" view of the MOC, with substantial exchange occurring between AMOC and the abyssal cell. A circulation corresponding to an adiabatic mid depth cell is also evident, with a portion of the AMOC recirculating into the northern basins immediately after surfacing in the Southern Ocean.

2. Agreement between ECCO's representation of the MOC and other observational and

modeling estimates is mixed. AMOC strength in ECCO roughly coincides with those predicted by other observation-based reconstructions and modeling, while the abyssal cell is somewhat weaker than other contemporary estimates suggest. The abyssal cell also shows some weakening between the subsequent releases of the ECCO version 4 product (c.f. Cessi, 2019).

3. Isopycnal volume trends play a central role in ECCO's representation of the deep ocean overturning, a result that is in disagreement with the widespread picture of a global circulation that is near equilibrium. These trends are obscured in the climatological average of ECCO's deep overturning.

4. The widespread isopycnal volume changes in ECCO's deep oceans are accompanied by much lower rates of diapycnal mixing than inferred by contemporary observations, and may represent a systematic error in the ECCO model setup. However, the lack of strong observational constraints in the abyssal ocean makes it difficult to completely rule out the ECCO solution.

In Chapters 3 and 4 we investigate the influence of zonal asymmetries in Southern Ocean topography on our current view of the MOC in an idealized setting. Based on our results, we establish a simple model describing the effects of Southern Ocean topographic features on the abyssal ocean's composition and circulation. Finally, we test our model in the presence of more complex Southern Ocean topography and show that it remains robust. A summary of our main results from Chapters 3 and 4 are as follows:

1. To test how the pathways of the MOC may be influenced by Southern Ocean topography we carry out idealized experiments testing the sensitivity of the ocean circulation to the height of a submarine ridge in Drake Passage. Our results show that the mid depth cell is largely insensitive to Southern Ocean topography until the topographic height begins to intersect with the lower NADW isopycnals, after which mid depth

cell strength drops substantially. The abyssal cell only shows slight strengthening in response to higher Drake Passage ridges.

2. Tracer release experiments tracking the ventilation rate of the deep ocean reveal that the composition of the abyssal ocean is closely tied to changes in the MOC brought about by changing Drake Passage ridge height. Abyssal ventilation by NADW and other surface waters north of the ACC increase with a strengthening mid depth cell and increased intermediate water formation, both of which are closely tied to the height of the Drake Passage ridge.

3. "Exchange" tracer experiments, which allow us to trace back the origin of watermasses before they sink into the abyss around Antarctica, reveal that changes in the surface circulation of the Southern Ocean can also influence the composition of the abyssal ocean. We find that the presence of a Southern Ocean gyre leads to a substantial increase in horizontal mixing at the surface of the Southern Ocean, which leads to increased exchange between the upwelling branch of the overturning circulation and the surface waters to the north. This gyre-driven exchange pathway is significant and is currently absent from idealized models of the overturning circulation.

4. The MOC response to changing topographic height described in Chapter 3 persists when more complex topographic setups are employed. In particular, the relationship between NADW isopycnals intersecting with Southern Ocean topography and the strength of the mid depth cell is preserved. Furthermore, the abyssal cell remains largely insensitive to changing topographic configuration with changing topographic height leading to modest changes in abyssal cell strength.

5. The gyre-driven exchange pathway also persists in more complex Southern Ocean topographic configurations such as cases including a zonal extension to the Drake Passage ridge or additional meridional ridges spaced throughout the Southern Ocean channel. However, we find that the exchange pathway is only dependent on the strength of the

gyre in the vicinity of Drake Passage and is uncorrelated with any additional gyres that develop.

5.2 Future study

The results of this thesis can be built upon for future study. One avenue is to reconcile the disagreement between the ECCO state estimate and current theoretical models and observational predictions of the deep ocean circulation. Another avenue is to further explore the implications of our theory developed in Chapters 3 and 4, particularly with respect to the picture of an interconnected MOC such as that described by Ferrari et al. (2014). Details for each direction are discussed below.

5.2.1 Further refinement of the ECCO solution

The validity of the ECCO state estimate's representation of the abyssal ocean must be investigated if the ECCO product is to remain useful for studies of the deep ocean circulation. As discussed in Chapter 2, the core inconsistency between ECCO and the prevailing theoretical and observational pictures of the deep ocean is a lack of significant vertical diapycnal mixing in ECCO's abyssal ocean. Without significant vertical mixing in the abyssal ocean, northward flowing Antarctic Bottom Water is not fully consumed and is instead balanced by a steady upward movement of isopycnals. Over time this behavior will likely result in a significantly less stratified abyssal ocean than what we observe today, which may not be an accurate representation of the real ocean.

We propose a study to investigate whether the transient signal in ECCO's overturning water mass budgets can be accounted for by applying a more realistic vertical diffusivity field as a prior to the ECCO inversion. Independent estimates for the vertical diapycnal diffusivity in the abyssal ocean have been shown to be much larger than that present in the ECCO state estimate (de Lavergne et al., 2020b). This may be due to choices made in

the ECCO configuration: the ECCO adjoint treats the spatial vertical diffusivity field as a "control parameter" when fitting the model to observations, meaning that its value is adjusted away from some prior estimate as part of the optimization process (Forget et al., 2015). However, the prior vertical diffusivity used in ECCO is a uniform field of low diffusivity, $\kappa(x, y, z) = 10^{-5} m^2 s^{-1}$, which is much smaller than current estimates of abyssal vertical diffusivity, and the solution fails to adjust the vertical diffusivity field meaningfully in the abyssal ocean due to a lack of observational constraints for the evolution of the abyssal temperature and salinity fields (Trossman et al., 2022). Thus, we propose an experiment to re-optimize the ECCO solution starting from a prior diffusivity field that is based on current estimates of diapycnal mixing from internal tide energy dissipation rates (de Lavergne et al., 2020b). We expect that this change will yield an abyssal ocean in which isopcynal volume trends play a much smaller role in the overturning and a much improved representation of the abyssal circulation and water mass transformations in ECCO.

Other aspects of the ECCO model can be refined as part of future work. For example, ECCO lacks dense water overflows over the GIS ridge system, which may contribute to the lack of replenishment of the densest NADW water masses in the Atlantic and thus the negative density tendencies in ECCO's abyssal Atlantic. Further study could involve re-optimizing the ECCO state estimate with the addition of a dense water overflow parameterization, such as Briegleb et al. (2010) to better capture these processes. It is clear that the ECCO solution requires more refinement, and continued investigations of its accuracy will remain crucial for future development of the ECCO solution and our understanding of the abyssal ocean circulation.

5.2.2 Further exploration of the role of Southern Ocean topography

The results presented in Chapter 3 and Chapter 4 provide simple predictors for the response of the MOC to changing Southern Ocean topography in an idealized setting. However, work remains both in terms of characterizing the physical mechanisms behind these results and

verifying their significance to the real ocean circulation. We outline some potential avenues for continued study below.

First, we can further investigate the relationship between mid depth cell strength and Drake Passage ridge height. The mid depth cell is largely insensitive to low topographic heights across our simulations, but drops precipitously once Drake Passage topography begins to intersect with NADW isopycnals exiting the South Atlantic. This robust relationship has not been described previously making it an interesting target for future research. Theoretically, the weakening of the Southern Ocean's mid depth cell in the presence of a high ridge is likely attributable to the development of a pressure-contrast across the topography, which in turn allows for a geostrophic flow that compensates the wind-driven overturning. A predictive theory that quantifies this effect could be developed in future work, and our existing numerical results can be used to test the theory.

The simple box model derived in Chapter 3 gives a tool for quantifying the effect of the Southern Ocean polar gyres on the abyssal ocean's watermass composition in our idealized setups, but work remains if we wish to integrate it into our theoretical view of the MOC (e.g. in the "figure eight" configuration hypothesized by Ferrari et al., 2017). A useful first step would be to investigate how gyres affect tracer concentrations in the presence of dynamic sea ice. Sea ice modifies the surface buoyancy restoring fields and has been hypothesized to play a key role in setting the rate of intercell exchange during present day and the Last Glacial Maximum (LGM) (Ferrari et al., 2014, 2017; Nadeau et al., 2019). Thus, further study could examine the response of the exchange rate, T_{mix}, and the MOC to dynamic sea ice and salinity forcing in a similar setup to that used in Chapters 3 and 4. Following this, possible further steps include exploring the robustness of the T_{mix} pathway under the addition of seasonal surface forcing and a dynamic atmosphere.

We must verify the extent to which Southern Ocean topography's effect on T_{mix} and the mid depth cell are relevant to the real ocean beyond our idealized setups. Steps towards this goal include recreating our tracer release experiments under realistic topography and surface

forcing, paying particular attention to the rate of southward tracer transport by the Weddell and Ross Gyres towards AABW formation regions. Passive tracer experiments similar to those employed in our idealized cases using realistic topography, eddy-permitting resolution, and dynamic sea ice and seasonal surface forcing could be employed.

5.3 Summary

The results of this thesis provide guidance for the use and further development of ocean reanalysis products, refinement of idealized models of the MOC, and open the door to future study of the MOC and its representation in reanalysis. Our characterization of the isopycnal MOC as represented by ECCO in Chapter 2 simultaneously confirms some of our theoretical predictions of the ocean circulation (i.e. an interconnected MOC and a mostly adiabatic mid depth cell) and identifies disagreement between the ECCO solution and theoretical and model predictions. We highlight shortcomings in ECCO's representation of abyssal diapycnal mixing that can and should be corrected in future iterations of the ECCO reanalysis. Given that ECCO is a popular choice for studies seeking to characterization the abyssal ocean circulation, this result has consequences also for past studies that have based their conclusions off of ECCO's fundamentally transient ocean circulation. The results presented in Chapter 3 address the role of Southern Ocean topography in the MOC and deep ocean watermass properties, highlighting in particular the non-negligible role of gyre-induced exchange between the abyssal overturning cell and the surface waters north of the ACC, a process that has not previously been included in idealized models of the overturning circulation. The results in Chapter 4 further indicate that the gyre-driven mixing pathway that transports surface waters towards AABW formation regions, derived in Chapter 3, is robust across different topographic configurations and highlight the primary role of the gyre closest to Drake Passage in controlling the overall composition of the abyssal cell in our setups.

REFERENCES

Abernathey, R. and Cessi, P. (2014). Topographic enhancement of eddy efficiency in baroclinic equilibration. *Journal of Physical Oceanography*, 44(8):2107 – 2126.

Abernathey, R., Marshall, J., and Ferreira, D. (2011). The dependence of southern ocean meridional overturning on wind stress. *Journal of Physical Oceanography*, 41(12):2261 – 2278.

Abernathey, R. P., Cerovecki, I., Holland, P. R., Newsom, E., Mazloff, M., and Talley, L. D. (2016). Water-mass transformation by sea ice in the upper branch of the southern ocean overturning. *Nature Geoscience*, 9:596–601.

Anagnostou, E., John, E. H., Edgar, K. M., Foster, G. L., Ridgwell, A., Inglis, G. N., Pancost, R. D., Lunt, D. J., and Pearson, P. N. (2016). Changing atmospheric co2 concentration was the primary driver of early cenozoic climate. *Nature*, 533(7603):380–384.

Baker, J. A., Watson, A. J., and Vallis, G. K. (2020). Meridional overturning circulation in a multibasin model. Part I: Dependence on Southern Ocean buoyancy forcing. *Journal of Physical Oceanography*, 50(5):1159 – 1178.

Balwada, D., Smith, K. S., and Abernathey, R. (2018). Submesoscale vertical velocities enhance tracer subduction in an idealized antarctic circumpolar current. *Geophysical Research Letters*, 45(18):9790–9802.

Bishop, S. P., Gent, P. R., Bryan, F. O., Thompson, A. F., Long, M. C., and Abernathey, R. (2016). Southern Ocean overturning compensation in an eddy-resolving climate simulation. *Journal of Physical Oceanography*, 46(5):1575 – 1592.

Boer, A. M. D., Hutchinson, D. K., Roquet, F., Sime, L. C., Burls, N. J., and Heuzé, C. (2022). The impact of southern ocean topographic barriers on the ocean circulation and the overlying atmosphere. *Journal of Climate*, 35(18):5805 – 5821.

Brady, R. X., Maltrud, M. E., Wolfram, P. J., Drake, H. F., and Lovenduski, N. S. (2021). The influence of ocean topography on the upwelling of carbon in the southern ocean. *Geophysical Research Letters*, 48(19):e2021GL095088.

Briegleb, B., Danabasoglu, G., and Large, W. (2010). An overflow parameterization for the ocean component of the community climate system model. *University Corporation for Atmospheric Research*.

Broecker, W. S. (1987). The biggest chill. *Natural History*, 97:74–82.

Broecker, W. S. (1991). The great ocean conveyor. *Oceanography*, 4(2):79–89.

Bryan, F. (1986). High-latitude salinity effects and interhemispheric thermohaline circulations. *Nature*, 323(6086):301–304.

Buckley, M. W., Lozier, M. S., Desbruyères, D., and Evans, D. G. (2023). Buoyancy forcing and the subpolar atlantic meridional overturning circulation. *Philosophical Transactions of the Royal Society A: Mathematical, Physical and Engineering Sciences*, 381(2262):20220181.

Buckley, M. W. and Marshall, J. (2016). Observations, inferences, and mechanisms of the atlantic meridional overturning circulation: A review. *Reviews of Geophysics*, 54(1):5–63.

Cessi, P. (2019). The global overturning circulation. *Annual Review of Marine Science*, 11(1):249–270.

Chang, C.-Y. and Jansen, M. F. (2021). Distinct controls on the strength of the abyssal overturning circulation: Channel versus basin dynamics. *Journal of Physical Oceanography*, 51(7):2073 – 2086.

de Boer, A. M., Hutchinson, D. K., Roquet, F., Sime, L. C., Burls, N. J., and Heuzé, C. (2022). The impact of southern ocean topographic barriers on the ocean circulation and the overlying atmosphere. *Journal of Climate*, 35(18):5805–5821.

de Lavergne, C., Madec, G., Le Sommer, J., George Nurser, A. J., and Naveira Garabato, A. (2016). On the consumption of Antarctic Bottom Water in the abyssal ocean. *Journal of Physical Oceanography*, pages 635–661.

de Lavergne, C., Vic, C., Madec, G., Roquet, F., Waterhouse, A. F., Whalen, C. B., Cuypers, Y., Bouruet-Aubertot, P., Ferron, B., and Hibiya, T. (2020a). A parameterization of local and remote tidal mixing. *Journal of Advances in Modeling Earth Systems*, 12(5):e2020MS002065.

de Lavergne, C., Vic, C., Madec, G., Roquet, F., Waterhouse, A. F., Whalen, C. B., Cuypers, Y., Bouruet-Aubertot, P., Ferron, B., and Hibiya, T. (2020b). A parameterization of local and remote tidal mixing. *Journal of Advances in Modeling Earth Systems*, 12.

Desbruyères, D. G., McDonagh, E. L., King, B. A., and Thierry, V. (2017). Global and full-depth ocean temperature trends during the early twenty-first century from Argo and repeat hydrography. *Journal of Climate*, 30(6):1985–1997.

Donohoe, A., Armour, K. C., Roe, G. H., Battisti, D. S., and Hahn, L. (2020). The partitioning of meridional heat transport from the last glacial maximum to co2 quadrupling in coupled climate models. *Journal of Climate*, 33(10):4141 – 4165.

Dotto, T. S., Naveira Garabato, A., Bacon, S., Tsamados, M., Holland, P. R., Hooley, J., Frajka-Williams, E., Ridout, A., and Meredith, M. P. (2018). Variability of the ross gyre, southern ocean: Drivers and responses revealed by satellite altimetry. *Geophysical Research Letters*, 45(12):6195–6204.

Eady, E. (1957). The general circulation of the atmosphere and oceans. *The Earth and Its Atmosphere*, pages 130–151.

ECCO Consortium, Fukumori, I., Wang, O., Fenty, I., Forget, G., Heimbach, P., and Ponte, R. M. (2021). Synopsis of the ecco central production global ocean and sea-ice state estimate (version 4 release 4). *ECCO Consortium*.

ECCO Consortium, Fukumori, I., Wang, O., Fenty, I., Forget, G., Heimbach, P., and Ponte, R. M. (2022). Ecco central estimate (version 4 release 4). *ECCO Consortium*. last accessed on 3/20/2022.

Ferrari, R. and Ferreira, D. (2011). What processes drive the ocean heat transport? *Ocean Modelling*, 38(3-4):171–186.

Ferrari, R., Jansen, M., Adkins, J., Burke, A., Stewart, A., and Thompson, A. (2014). Antarctic sea ice control on ocean circulation in present and glacial climates. *Proceedings of the National Academy of Sciences*, 111(24):8753–8758.

Ferrari, R., Nadeau, L., Marshall, D. P., Allison, L. C., and Johnson, H. L. (2017). A model of the ccean circulation with two closed basins and a reentrant channel. *Journal of Physical Oceanography*, 47(12):2887–2906.

Ferreira, D., Cessi, P., Coxall, H. K., de Boer, A., Dijkstra, H. A., Drijfhout, S. S., Eldevik, T., Harnik, N., McManus, J. F., Marshall, D. P., Nilsson, J., Roquet, F., Schneider, T., and Wills, R. C. (2018). Atlantic-pacific asymmetry in deep water formation. *Annual Review of Earth and Planetary Sciences*, 46(Volume 46, 2018):327–352.

Forget, G., J.-M., C., Heimbach, P., Hill, C. N., Ponte, R. M., and Wunsch, C. (2015). ECCO version 4: an integrated framework for non-linear inverse modeling and global ocean state estimation. *Geoscientific Model Development*, 8(10):3071–3104.

Forget, G. and Ponte, R. (2015). The partition of regional sea level variability. *Progress in Oceanography*, 137:173–195.

Gaspar, P., Grégoris, Y., and Lefevre, J.-M. (1990). A simple eddy kinetic energy model for simulations of the oceanic vertical mixing: Tests at station Papa and long-term upper ocean study site. *Journal of Geophysical Research: Oceans*, 95(C9):16179–16193.

Gebbie, G. and Huybers, P. (2010). Total matrix intercomparison: A method for determining the geometry of water-mass pathways. *Journal of Physical Oceanography*, 40(8):1710 – 1728.

Gent, P. R. and Mcwilliams, J. C. (1990). Isopycnal mixing in ocean circulation models. *Journal of Physical Oceanography*, 20:150–155.

Gnanadesikan, A. (1999). A simple predictive model for the structure of the oceanic pycnocline. *Science*, 283(5410):2077–2079.

Goldner, A., Herold, N., and Huber, M. (2014). Antarctic glaciation caused ocean circulation changes at the eocene–oligocene transition. *Nature*, 511(7511):574–577.

Gordon, A., Martinson, D., and Taylor, H. (1981). The wind-driven circulation in the weddell-enderby basin. *Deep Sea Research Part A. Oceanographic Research Papers*, 28(2):151–163.

Gordon, A. L. (1986). Is there a global scale ocean circulation. *EOS, Transactions American Geophysical Union*, pages 109–110.

Griffies, S. M., Pacanowski, R. C., and Hallberg, R. W. (2000). Spurious diapycnal mixing associated with advection in a z-coordinate ocean model. *Monthly Weather Review*, 128:538–564.

Haine, T. W. N. and Hall, T. M. (2002). A generalized transport theory: water-mass composition and age. *Journal of Physical Oceanography*, 32(6):1932 – 1946.

Ito, T., Woloszyn, M., and Mazloff, M. (2010). Anthropogenic carbon dioxide transport in the southern ocean driven by ekman flow. *Nature*, 463(7277):80–83.

Jansen, M. F. (2017). Glacial ocean circulation and stratification explained by reduced atmospheric temperature. *Proceedings of the National Academy of Sciences*, 114(1):45–50.

Jones, C. S. and Abernathey, R. (2019). Isopycnal mixing controls deep ocean ventilation. *Geophysical Research Letters*, 46(22):13144–13151.

Jones, C. S. and Cessi, P. (2016). Interbasin transport of the meridional overturning circulation. *Journal of Physical Oceanography*, pages 1157–1169.

Jones, C. S. and Cessi, P. (2017). Size matters: Another reason why the atlantic is saltier than the pacific. *Journal of Physical Oceanography*, 47(11):2843–2859.

Kennedy, A. T., Farnsworth, A., Lunt, D. J., Lear, C. H., and Markwick, P. J. (2015). Atmospheric and oceanic impacts of antarctic glaciation across the eocene–oligocene transition. *Philosophical Transactions of the Royal Society A: Mathematical, Physical and Engineering Sciences*, 373(2054):20140419.

Kennett, J. P. (1977). Cenozoic evolution of antarctic glaciation, the circum-antarctic ocean, and their impact on global paleoceanography. *Journal of Geophysical Research (1896-1977)*, 82(27):3843–3860.

Killworth, P. D. (1992). An equivalent-barotropic mode in the fine resolution antarctic model. *Journal of Physical Oceanography*, 22(11):1379–1387.

Koltermann, K., Gouretski, V., and Jancke, K. (2011). *Hydrographic atlas of the world ccean circulation experiment (WOCE).*, volume Volume 3: Atlantic Ocean. International WOCE Project Office, Southampton, UK.

Kong, H. and Jansen, M. F. (2021). The impact of topography and eddy parameterization on the simulated Southern Ocean circulation response to changes in surface wind stress. *Journal of Physical Oceanography*, 51(3):825 – 843.

Kunze, E. (2017). The internal-wave-driven meridional overturning circulation. *Journal of Physical Oceanography*, pages 2673–2689.

Kunze, E., Firing, E., Hummon, J. M., Chereskin, T. K., and Thurnherr, A. M. (2006). Global abyssal mixing inferred from lowered adcp shear and ctd strain profiles. *Journal of Physical Oceanography*, 36(8):1553–1576.

LaCasce, J. H. and Isachsen, P. E. (2010). The linear models of the acc. *Progress in Oceanography*, 84(3):139–157.

Ledwell, J. R., Watson, A. J., and Law, C. S. (1998). Mixing of a tracer in the pycnocline. *Journal of Geophysical Research: Oceans*, 103(C10):21499–21529.

Lee, M.-M., Coward, A. C., and George Nurser, A. (2002). Spurious diapycnal mixing of the deep waters in and eddy-permitting global ocean model. *Journal of Physical Oceanography*, 32:1522–1535.

Lee, S.-K., Lumpkin, R., Baringer, M. O., Meinen, C. S., Goes, M., Dong, S., Lopez, H., and Yeager, S. G. (2019). Global meridional overturning circulation inferred from a data-constrained ocean & sea-ice model. *Geophysical Research Letters*, 46(3):1521–1530.

Li, L., Liu, Z., Du, J., Wan, L., and Lu, J. (2023). Mechanisms of global ocean ventilation age change during the last deglaciation. *EGUsphere*, 2023:1–25.

Liang, X., Piecuch, C. G., Ponte, R. M., Forget, G., Wunsch, C., and Heimbach, P. (2017). Change of the global ocean vertical heat transport over 1993–2010. *Journal of Climate*, pages 5319–5327.

Liang, X., Wunsch, C., Heimbach, P., and Gael, F. (2015). Vertical redistribution of oceanic heat content. *Journal of Climate*, pages 3821–3833.

Lumpkin and Speer (2007). Global ocean meridional overturning. *Journal of Physical Oceanography*, 37(10):2550–2562.

Mak, J., Maddison, J. R., Marshall, D. P., and Munday, D. R. (2018). Implementation of a geometrically informed and energetically constrained mesoscale eddy parameterization in an ocean circulation model. *Journal of Physical Oceanography*, 48(10):2363–2382.

Marshall, J., Adcroft, A. J., Hill, C., Perelman, L. T., and Heisey, C. W. (1997a). A finite-volume, incompressible navier stokes model for studies of the ocean on parallel computers. *Journal of Geophysical Research*, 102:5753–5766.

Marshall, J., Hill, C., and Perelman, L. (1997b). Hydrostatic, quasi-hydrostatic, and nonhydrostatic ocean modeling. *Journal of Geophysical Research: Oceans*, 102(C3):5733–5752.

Marshall, J., R. Scott, J., Armour, K., and et al. (2015). The ocean's role in the transient response of climate to abrupt greenhouse gas forcing. *Climate Dynamics*, pages 2287–2299.

Marshall, J. and Radko, T. (2003). Residual-mean solutions for the Antarctic circumpolar current and its associated overturning circulation. *Journal of Physical Oceanography*, 33(11):2341 – 2354.

Marshall, J. and Speer, K. (2012). Closure of the meridional overturning circulation through Southern Ocean upwelling. *Nature Geoscience*, 5(3):171–181.

Marzocchi, A. and Jansen, M. F. (2019). Global cooling linked to increased glacial carbon storage via changes in Antarctic sea ice. *Nature Geoscience*, 12(12):1001–1005.

Mashayek, A., Ferrari, R., Merrifield, S., Ledwell, J. R., St Laurent, L., and Garabato, A. N. (2017). Topographic enhancement of vertical turbulent mixing in the southern ocean. *Nature Communications*, 8(1):14197.

Masich, J., Chereskin, T. K., and Mazloff, M. R. (2015a). Topographic form stress in the southern ocean state estimate. *Journal of Geophysical Research: Oceans*, 120(12):7919–7933.

Masich, J., Chereskin, T. K., and Mazloff, M. R. (2015b). Topographic form stress in the southern ocean state estimate. *Journal of Geophysical Research: Oceans*, 120(12):7919–7933.

Mazloff, M. R., Heimbach, P., and Wunsch, C. (2010). An eddy-permitting southern ocean state estimate. *Journal of Physical Oceanography*, 40(5):880–899.

Megann, A. (2017). Estimating the numerical diapycnal mixing in an eddy-permitting ocean model. *Ocean Modelling*, 121:19–33.

Morrison, A. K., England, M. H., Hogg, A. M., and Kiss, A. E. (2023). Weddell sea control of ocean temperature variability on the western antarctic peninsula. *Geophysical Research Letters*, 50(15):e2023GL103018.

Munk, W. H. (1966). Abyssal recipes. *Deep Sea Research*, 13:707–730.

Munk, W. H. and Palmén, E. (1951). Note on the dynamics of the antarctic circumpolar current. *Tellus*, 3(1):53–55.

Nadeau, L., Ferrari, R., and Jansen, M. F. (2019). Antarctic sea ice control on the depth of North Atlantic deep water. *Journal of Climate*, 32(9):2537–2551.

Nadeau, L. and Jansen, M. F. (2020). Overturning circulation pathways in a two-basin ocean model. *American Meteorlogical Society*, 50:2105–2122.

Nadeau, L.-P. and Ferrari, R. (2015). The role of closed gyres in setting the zonal transport of the antarctic circumpolar current. *Journal of Physical Oceanography*, 45(6):1491 – 1509.

Newsom, E. R., Bitz, C. M., Bryan, F. O., Abernathey, R., and Gent, P. R. (2016). Southern ocean deep circulation and heat uptake in a high-resolution climate model. *Journal of Climate*, 29(7):2597–2619.

Nikurashin, M. and Vallis, G. (2012). A theory of the interhemispheric meridional overturning circulation and associated stratification. *Journal of Physical Oceanography*, 42(10):1652 – 1667.

NOAA National Centers for Environmental Information (2022). Etopo 2022 15 arc-second global relief model. NOAA National Centers for Environmental Information.

Nurser, A. J. G. and Lee, M.-M. (2004). Isopycnal averaging at constant height. Part II: Relating to the residual streamfunction in eulerian space. *Journal of Physical Oceanography*, 34(12):2740 – 2755.

Ohshima, K. I., Fukamachi, Y., Williams, G. D., Nihashi, S., Roquet, F., Kitade, Y., Tamura, T., Hirano, D., Herraiz-Borreguero, L., Field, I., Hindell, M., Aoki, S., and Wakatsuchi, M. (2013). Antarctic bottom water production by intense sea-ice formation in the cape darnley polynya. *Nature Geoscience*, 6(3):235–240.

Olbers, D. (1998). Comments on "on the obscurantist physics of 'form drag'in theorizing about the circumpolar current. *Journal of Physical Oceanography*, 28(8):1647–1654.

Palmer, M., Roberts, C., Balmaseda, M., Chang, Y.-S., Chepurin, G., Ferry, N., Fuji, Y., Good, S., Guinehut, S., Haines, K., Hernandez, F., Kohl, A., Lee, T., Martin, M., Masina, S., Masuda, S., Peterson, K., Storto, A., Toyoda, T., Valdivieso, M., Vernieres, G., Wang, O., and Xue, Y. (2015). Ocean heat content variability and change in an ensemble of ocean reanalysis. *Climate Dynamics*, 49:909–930.

Patmore, R. D., Holland, P. R., Munday, D. R., Garabato, A. C. N., Stevens, D. P., and Meredith, M. P. (2019). Topographic control of Southern Ocean gyres and the Antarctic circumpolar current: A barotropic perspective. *Journal of Physical Oceanography*, 49(12):3221 – 3244.

Piecuch, C. G. (2017). A note on practical evaluation of budgets in ecco version 4 release 3.

Prather, M. J. (1986). Numerical advection by conservation of second-order moments. *Journal of Geophysical Research: Atmospheres*, 91(D6):6671–6681.

Prend, C. J., MacGilchrist, G. A., Manucharyan, G. E., Pang, R. Q., Moorman, R., Thompson, A. F., Griffies, S. M., Mazloff, M. R., Talley, L. D., and Gille, S. T. (2024). Ross gyre variability modulates oceanic heat supply toward the west antarctic continental shelf. *Communications Earth & Environment*, 5(1):47.

Primeau, F. (2005). Characterizing transport between the surface mixed layer and the ocean interior with a forward and adjoint global ocean transport model. *Journal of Physical Oceanography*, 35(4):545 – 564.

Purkey, S. and Johnson, G. (2010). Warming of global abyssal and deep southern ocean waters between the 1990s and 2000s: Contributions to global heat and sea level rise budgets. *Journal of Climate*, 23(23).

Ragen, S., Armour, K. C., Thompson, L., Shao, A., and Darr, D. (2022). The role of atlantic basin geometry in meridional overturning circulation. *Journal of Physical Oceanography*, 52(3):475–492.

Redi, M. H. (1982). Oceanic isopycnal mixing by coordinate rotation. *Journal of Physical Oceanography*, 12:1154–1158.

Reeve, K. A., Boebel, O., Strass, V., Kanzow, T., and Gerdes, R. (2019). Horizontal circulation and volume transports in the Weddell Gyre derived from Argo float data. *Progress in Oceanography*, 175:263–283.

Rossby, T., Flagg, C., Chafik, L., Harden, B., and Søiland, H. (2018). A direct estimate of volume, heat, and freshwater exchange across the Greenland-Iceland-Faroe-Scotland ridge. *Journal of Geophysical Research: Oceans*, 123(10):7139–7153.

Rousselet, L. and Cessi, P. (2022). Diabatic transformations along the global routes of the mid-depth meridional overturning circulation. *American Meteorolgical Society*, 52.

Rousselet, L., Cessi, P., and Forget, G. (2021). Coupling of the mid-depth and abyssal components of the global overturning circulation according to a state estimate. *Science Advances*, 7(21).

Sauermilch, I., Whittaker, J. M., Klocker, A., Munday, D. R., Hochmuth, K., Bijl, P. K., and LaCasce, J. H. (2021). Gateway-driven weakening of ocean gyres leads to southern ocean cooling. *Nature Communications*, 12(1):6465.

Schmidgall, C. R., Si, Y., Stewart, A. L., Thompson, A. F., and Hogg, A. M. (2023). Dynamical controls on bottom water transport and transformation across the antarctic circumpolar current. *Journal of Physical Oceanography*, 53(8):1917–1940.

Schmitz, W. J. (1995). On the interbasin-scale thermohaline circulation. *Review of Geophysics*, pages 151–173.

Schröder, M. and Fahrbach, E. (1999). On the structure and the transport of the eastern Weddell Gyre. *Deep Sea Research Part II: Topical Studies in Oceanography*, 46(1):501–527.

Shakespeare, C. J. and Hogg, A. M. (2012). An analytical model of the response of the meridional overturning circulation to changes in wind and buoyancy forcing. *Journal of Physical Oceanography*, 42(8):1270 – 1287.

Sigman, D. M., Hain, M. P., and Haug, G. H. (2010). The polar ocean and glacial cycles in atmospheric CO2 concentration. *Nature*, 466(7302):47–55.

Sijp, W. P. and England, M. H. (2004). Effect of the drake passage throughflow on global climate. *Journal of Physical Oceanography*, 34(5):1254–1266.

Srokosz, M., Baringer, M., Bryden, H., Cunningham, S., Delworth, T., Lozier, S., Marotzke, J., and Sutton, R. (2012). Past, present, and future changes in the Atlantic meridional overturning circulation. *Bulletin of the American Meteorological Society*, 93(11):1663 – 1676.

Stephens, B. B. and Keeling, R. F. (2000). The influence of Antarctic sea ice on glacial–interglacial CO2 variations. *Nature*, 404(6774):171–174.

Stevens, D. P. and Ivchenko, V. O. (1997). The zonal momentum balance in an eddy-resolving general-circulation model of the southern ocean. *Quarterly Journal of the Royal Meteorological Society*, 123(540):929–951.

Stewart, A. L. and Hogg, A. M. (2017). Reshaping the Antarctic circumpolar current via Antarctic bottom water export. *Journal of Physical Oceanography*, 47(10):2577 – 2601.

Stewart, A. L., Neumann, N. K., and Solodoch, A. (2023). "eddy"saturation of the antarctic circumpolar current by standing waves. *Journal of Physical Oceanography*, 53(4):1161–1181.

Stommel, H. and Arons, A. B. (1959). On the abyssal circulation of the world ocean - II. An idealized model of the circulation pattern and amplitude in oceanic basins. *Deep Sea Research*, pages 217–233.

Sverdrup, H. U. (1947). Wind-driven currents in a baroclinic ocean; with application to the equatorial currents of the eastern pacific. *Proceedings of the National Academy of Sciences*, 33(11):318–326.

Talley, L. (2013). Closure of the global overturning circulation through the Indian, Pacific, and Southern oceans: Schematics and transports. *Oceanography*, 26(1):80–97.

Talley, L., Pickard, G., Emery, W., and Swift, J. (2011). Descriptive physical oceanography: an introduction (sixth edition). *Elsevier, Boston*.

Talley, L., Reid, J., and Robbins, P. (2003). Data-based meridional overturning streamfunctions for the global ocean. *Journal of Climate*, 16:3213–3226.

Tamsitt, V., Drake, H. F., Morrison, A. K., Talley, L. D., Dufour, C. O., Gray, A. R., Griffies, S. M., Mazloff, M. R., Sarmiento, J. L., Wang, J., and Weijer, W. (2017). Spiraling pathways of global deep waters to the surface of the Southern Ocean. *Nature Communications*, 8(1):172.

Tesdal, J.-E. and Haine, T. W. N. (2020). Dominant terms in the freshwater and heat budgets of the subpolar north atlantic ocean and nordic seas from 1992 to 2015. *Journal of Geophysical Research: Oceans*, 125(10).

Thompson, A., Stewart, A., and Bischoff, T. (2016). A multibasin residual-mean model for the global overturning circulation. *Journal of Physical Oceanography*, 46(9):2583–2604.

Thompson, A. F. and Garabato, A. C. N. (2014). Equilibration of the Antarctic circumpolar current by standing meanders. *Journal of Physical Oceanography*, 44(7):1811 – 1828.

Thompson, A. F. and Naveira Garabato, A. C. (2014). Equilibration of the antarctic circumpolar current by standing meanders. *Journal of Physical Oceanography*, 44(7):1811–1828.

Toggweiler, J. and Samuels, B. (1995a). Effect of Drake Passage on the global thermohaline circulation. *Deep Sea Research Part I: Oceanographic Research Papers*, 42(4):477–500.

Toggweiler, J. R. and Bjornsson, H. (2000). Drake passage and palaeoclimate. *Journal of Quaternary Science*, 15(4):319–328.

Toggweiler, J. R. and Samuels, B. (1995b). Effect of drake passage on the global thermohaline circulation. *Deep Sea Research Part I: Oceanographic Research Papers*, 42(4):477–500.

Toggweiler, J. R. and Samuels, B. (1998). On the ocean's large-scale circulation near the limit of no vertical mixing. *Journal of Physical Oceanography*, 28(9):1832–1852.

Toumoulin, A., Donnadieu, Y., Ladant, J. B., Batenburg, S. J., Poblete, F., and Dupont-Nivet, G. (2020). Quantifying the effect of the drake passage opening on the eocene ocean. *Paleoceanography and Paleoclimatology*, 35(8):e2020PA003889.

Trossman, D. S., Whalen, C. B., Haine, T. W. N., Waterhouse, A. F., Nguyen, A. T., Bigdeli, A., Mazloff, M., and Heimbach, P. (2022). Tracer and observationally derived constraints on diapycnal diffusivities in an ocean state estimate. *Ocean Science*, 18:729–759.

Urakawa, L. S. and Hasumi, H. (2014). Effect of numerical diffusion on the water mass transformation in eddy-resolving models. *Ocean Modelling*, 74:22–35.

Vallis, G. K. (2000). Large-scale circulation and production of stratification: Effects of wind, geometry, and diffusion. *Journal of Physical Oceanography*, 30(5):933 – 954.

Walin, G. (1982). On the relation between sea-surface heat flow and thermal circulation in the ocean. *Tellus*, 34(2):187–195.

Wang, J., Mazloff, M. R., and Gille, S. T. (2016). The effect of the kerguelen plateau on the ocean circulation. *Journal of Physical Oceanography*, 46(11):3385 – 3396.

Wang, Z. (2013). On the response of southern hemisphere subpolar gyres to climate change in coupled climate models. *Journal of Geophysical Research: Oceans*, 118(3):1070–1086.

Ward, M. L. and Hogg, A. M. (2011). Establishment of momentum balance by form stress in a wind-driven channel. *Ocean Modelling*, 40(2):133–146.

Waterhouse, A. F., MacKinnon, J. A., Nash, J. D., Alford, M. H., Kunze, E., SImmons, H. L., Polzin, K. L., St. Laurent, L. C., Sun, O. M., Pinkel, R., Talley, L. D., Whalen, C. B., Huusen, T. N., Carter, G. S., Fer, I., Waterman, S., Naveira Garabato, A. C., Sanford, T. B., and Lee, C. M. (2014). Global patterns of diapycnal mixing from measurements of the turbulent dissipation rate. *Journal of Physical Oceanography*, 44:1854–1872.

Webb, D. J. and Suginohara, N. (2001). Oceanography. vertical mixing in the ocean. *Nature*, 409(6816):37.

Wilson, E. A., Thompson, A. F., Stewart, A. L., and Sun, S. (2022). Bathymetric control of subpolar gyres and the overturning circulation in the Southern Ocean. *Journal of Physical Oceanography*, 52(2):205 – 223.

Wolfe and Cessi (2011). The adiabatic pole-to-pole overturning circulation. *Journal of Physical Oceanography*, 41(9):1795–1810.

Wolfe, C. L. and Cessi, P. (2014). Salt feedback in the adiabatic overturning circulation. *Journal of Physical Oceanography*, 44(4):1175–1194.

Wunsch, C. and Heimbach, P. (2014). Bidecadal thermal changes in the abyssal ocean. *Journal of Physical Oceanography*, pages 2013–2030.

Wust, G. and Defant, A. (1936). Atlas zur schichtung und zirkulation des atlantischen ozeans. *Deutsche Atlantische Expedition Meteor 1925-1927, Wiss. Erg., Bd. V1-Atlas, Berlin*.

Xing, Q., Klocker, A., Munday, D., and Whittaker, J. (2023). Deepening of Southern Ocean gateway leads to abrupt onset of a deep-reaching meridional overturning circulation. *Geophysical Research Letters*, 50(19):e2023GL104382.

Xing, Q., Munday, D., Klocker, A., Sauermilch, I., and Whittaker, J. (2022). The sensitivity of the eocene–oligocene southern ocean to the strength and position of wind stress. *Climate of the Past*, 18(12):2669–2693.

Youngs, M. K. and Flierl, G. R. (2023). Extending residual-mean overturning theory to the topographically localized transport in the Southern Ocean. *Journal of Physical Oceanography*, 53(8):1901 – 1915.

Youngs, M. K., Thompson, A. F., Lazar, A., and Richards, K. J. (2017). Acc meanders, energy transfer, and mixed barotropic–baroclinic instability. *Journal of Physical Oceanography*, 47(6):1291–1305.

Zachos, J., Pagani, M., Sloan, L., Thomas, E., and Billups, K. (2001). Trends, rhythms, and aberrations in global climate 65 ma to present. *Science*, 292(5517):686–693.

Zanna, L., Khatiwala, S., Gregory, J. M., Ison, J., and Heimbach, P. (2019). Global reconstruction of historical ocean heat storage and transport. *Proceedings of the National Academy of Sciences*, 116(4):1126–1131.